

High Gain Antenna Array Design for 5G & MIMO Antenna Systems using Microstrip Ridge Gap Waveguide

Abdelmoniem Tajelsir Mahmoud Hassan

A Thesis

In the Department

of

Electrical and Computer Engineering

Presented in Partial Fulfillment of the Requirements

For the Degree of

Doctor of Philosophy (Electrical and Computer Engineering) at

Concordia University

Montreal, Québec, Canada

October 2020

© Abdelmoniem Tajelsir Mahmoud Hassan., 2020

CONCORDIA UNIVERSITY
SCHOOL OF GRADUATE STUDIES

This is to certify that the thesis prepared

By: Abdelmoniem Tajelsir Mahmoud Hassan.

Entitled: High Gain Antenna Array Design for 5G & MIMO Antenna Systems using
Microstrip Ridge Gap Waveguide.

and submitted in partial fulfillment of the requirements for the degree of

Doctor of Philosophy (Electrical & Computer Engineering)

Complies with the regulations of the University and meets the accepted standards with respect to originality and quality.

Signed by the final examining committee:

Dr. R. Ganesan _____ Chair

Dr. Aly Fathy _____ External Examiner

Dr. A. Youssef _____ External to Program

Dr. R. Paknys _____ Internal Examiner

Dr. A. Sebak _____ Internal Examiner

Dr. A. Kishk _____ Thesis Supervisor

Approved by: Dr. W. -P. Zhu, Graduate Program Director

October 21, 2020 Dr. Mourad Debbabi, Dean, Faculty of Engineering & Computer Science

ABSTRACT

High Gain Antenna Array Design for 5G & MIMO Antenna Systems using Microstrip Ridge Gap Waveguide

Abdelmoniem Tajelsir Mahmoud Hassan, Ph.D.
Concordia University, 2020.

The demand for high data rates and the unavailability of low-frequency bands have driven the need to explore and develop millimeter-wave (mm-wave) frequency bands. Indeed, the development of mm-wave frequencies has led to smaller radio frequency (RF) components and more compact profiles, creating more design constraints and challenges. Millimeter-wave technologies are the best-suited candidates that meet the requirements of 5G standards; specifically, for indoor communication, which requires higher gain and more directive beams. Gap waveguide technologies can be used to design high-gain antenna arrays and multiple input multiple output antenna systems (MIMO).

In this thesis, we are mainly focusing on Microstrip Ridge Gap Waveguide (MRGW) to design the antenna array systems for the 60 GHz band. Therefore, it is necessary to facilitate the design procedures and propose new design techniques. Here, we propose new design techniques for a large antenna array system using MRGW. The work of this thesis can be divided into two parts. Firstly, developing an efficient modeling and design tool for the MRGW to facilitate the design process. Recently, the use of MRGW has increased due to the need for self-packaged and low loss structures for millimeter-wave applications. The MRGW consists of a grounded textured surface, which is representing an artificial magnetic conductor (AMC) surface. The AMC surface is loaded with a thin low dielectric constant substrate with a printed strip topped with another air-filled or dielectric-filled substrate in which the wave propagates between the strip and the conducting plate covering such a substrate.

Currently, full-wave and optimization tools are usually used to design the MRGW structure, which makes the design slow and computationally expensive. Thus, an efficient modeling and design tool for the MRGW is proposed. Empirical expressions are developed for different MRGW parameters to provide the effective dielectric constant, characteristic impedance, and the dispersion effect. The expressions are verified with the full-wave solution. The results show the potential of the proposed approach in modeling and designing the MRGW structure. Secondly, an efficient procedure to

design a large finite planar array and its corporate feeding network is presented. The procedure is verified by an 8×8 and 16×16 array of magneto-electric (ME) dipoles fed by a network of MRGW. The procedure is based on designing the corporate feeding network by replacing the elements ports with the corresponding effective input impedance of each element that accounts for the mutual coupling between the antenna elements. In addition, the far-field characteristics of the array parameters such as the directivity, gain, and radiation patterns are predicted using pattern multiplication, including the mutual coupling effects. The results are verified with the full-wave numerical solution.

The procedure requires limited resources and speed up the design cycle. The use of the MRGW helps in having the feeding network lines to be tighter than using the ridge gap technology. Thus, allowing the distance between the radiating elements becomes smaller than one wavelength to avoid grating lobes. In addition, to avoid undesired bends and very tight lines that cause undesired interaction between the lines, unique power dividers are designed. Furthermore, a transition from waveguide WR-15 to the MRGW is proposed to feed two halves of the array antenna perfectly out of phase at all frequencies and rotating each half to form a mirrored array that better radiation pattern symmetry and low cross-polarization. Then, this procedure is implemented to design a circularly polarized antenna array with excellent performance. To further enhance the antenna, gain, and reduce the number of elements, a superstrate dielectric lens with the proper parameters is added. Study of a 4×4 MIMO system is studied, where each antenna is a sub-array to achieve the high gain requirements.

Finally, A low-profile, compact, and high-efficiency monopulse array antenna has been presented. The monopulse is built based on a hybrid coupler that has a wideband response for the reflection and the transmission coefficients. Then the monopulse system is used to present a multiplexing antenna system for short-range in the near field region wireless communication. The multiplexing system works as a MIMO system that has four independent channels. The performance of the system is evaluated through the simulation, which shows that it can be a promising candidate for the next wireless communication systems.

*To My Father's Memory,
To My Mother,
To My Sisters,
To My Friends,
To My Country.*

ACKNOWLEDGMENTS

‘‘and my success can only come from Allah In Him have I put my trust, and to Him do I always turn.’’ The Holy Qur'an Hud chapter (88).

Besides, I would like to thank my supervisor Dr. Ahmed Kishk for his ultimate support of my Ph.D. study that helped me to complete this work. Besides his immense knowledge, his patience and advice helped me in the research and writing of this thesis. Also, thanks to anyone helped me directly and indirectly to conduct this research.

I would like to thank Dr. Mohamed A. Moharram Hassan for his guidance through my research and for the advice when I started my Ph.D. journey.

Of course, all that could not be accomplished without my parents' support to have a successful life. Also, I would like to thank my lovely twin for her moral support and encouragement to achieve my goals.

Table of Contents

List of Tables.....x

List of Figures..... xi

List of Symbols xvii

List of Acronyms xviii

Chapter 1: Introduction..... 1

 1.1 Introduction2

 1.2 Millimeter-Wave and waveguide problems2

 1.3 Problem statement and work motivation.....4

 1.4 Objectives.....4

 1.5 Contribution and Novelty.....5

Chapter 2: Gap Waveguide Technology..... 7

 2.1 Introduction8

 2.2 Soft and Hard Surfaces.....8

 2.3 The Gap Waveguide Theory9

Chapter 3: Modeling and Design Empirical Formulas of Microstrip Ridge Gap Waveguide (MRGW) 14

 3.1 Introduction15

 3.2 Impedance Design Formulas15

 3.3 Width Design Formulas17

 3.4 Port Definition and Data Extraction.....18

 3.5 Equations Verification.....19

Chapter 4: Design Large Finite Array 29

 4.1 Introduction30

 4.2 Design Large Finite Array theory32

4.3	Mutual Admittance Matrix Construction for a Large Array	33
4.4	Effective Input Impedances Calculation for Antenna Array.....	34
4.4.1	Basic element design.....	34
4.4.2	8×8 elements for array design.....	37
4.4.3	16×16 antenna array design	45
4.4.4	Transition from WR-15 to MRGW.....	47
4.4.5	16×16 -element array optimization.....	48
4.5	Mutual Coupling and Failure Analysis in Antenna Arrays.....	56
4.5.1	Mutual Coupling and Radiation Characteristic.....	57
4.5.2	Failure of radiation elements and radiation characteristics.....	58
Chapter 5:	Circularly Polarized Antenna Array	59
5.1	Introduction	60
5.2	Design Procedures.....	61
5.2.1	8x8 antenna array design	63
Chapter 6:	Millimeter-Wave MIMO Antenna System And High Gain Using Double Superstrates	71
6.1	Millimeter-Wave MIMO Antenna	72
6.1.1	Design procedures.....	74
6.1.2	Sub-array antenna (8×8) design.....	75
6.1.3	Orthogonal 4×4 MIMO antenna design.....	78
6.2	Antenna Array based on Microstrip Ridge Gap Waveguide using Double Superstrates	82
6.2.1	Single ME-dipole antenna.....	82
6.2.2	2 × 2 ME-dipole array antenna	85
6.2.3	4 × 4 ME-dipole array antenna	90

6.3	Short-Range Wireless System based on Monopulse Microstrip Ridge Gap Waveguide	93
6.3.1	Monopulse components: Hybrid coupler.....	94
6.3.2	Monopulse components: Hybrid coupler plus delay lines.....	96
6.3.3	Short-range MIMO wireless system.....	101
6.3.4	Channel capacity of monopulse antenna array system.....	103
Chapter 7:	Conclusions and future work.....	105
7.1	Conclusions:.....	106
7.2	Future Work:.....	107
	References.....	109

List of Tables

Table I. 8×8-Element Array Gain	45
Table II. 16×16-Element Array Gain.....	52
Table III. Comparison Between Proposed and Reported 60-GHz Antenna Arrays	55
Table IV. Comparison Between Proposed and Reported 60-GHz Cp Antenna Arrays	70

List of Figures

Figure 2.1 Soft and hard surfaces realized with corrugations.....	8
Figure 2.2 Gap waveguides concept with ideal PEC-PMC parallel-plates.	9
Figure 2.3 Gap waveguide’s basic structure.	11
Figure 2.4 Gap waveguides: (a) Ridge gap waveguide, (b) Groove gap waveguide, (c) Microstrip ridge gap waveguide, and (d) Printed ridge gap waveguide.	12
Figure 3.1 Microstrip Ridge Gap Waveguide (MRGW) structure with Electromagnetic Band Gap (EBG) mushrooms with arrows indicate the field lines of the quasi-TEM mode.	15
Figure 3.2 Flow chart for the curve fitting.....	18
Figure 3.3 Port definition for MRGW.	19
Figure 3.4 Effective dielectric constant when $\epsilon r1$ is air: (a) case A, (b) case B, (c) case C, and (d) case D.....	20
Figure 3.5 Errors when $\epsilon r1$ is an air: (a) case A, (b) case B, (c) case C, and (d) case D.	20
Figure 3.6 Effective dielectric constant when the gap is filled with $\epsilon r1 < \epsilon r2$: (a) case E, (b) case F, (c) case G and (d) case H.....	21
Figure 3.7 Error when the gap filled with $\epsilon r1 < \epsilon r2$: (a) case E, (b) case F, (c) case G, and (d) case H.	22
Figure 3.8 Effective dielectric constant when filled with $\epsilon r1 > \epsilon r2$: (a) case X, and (b) case Y.	23
Figure 3.9 Errors when the gap filled $\epsilon r1 > \epsilon r2$: (a) case X, and (b) case Y.....	23
Figure 3.10 MRGW characteristic impedance with an air gap: (a) Case A, (b) Case B, (c) Case C, and (d) Case D.	24
Figure 3.11 MRGW characteristic impedance with a gap filled $\epsilon r1 < \epsilon r2$): (a) Case E, (b) Case F, (c) Case G and (d) Case H.....	25
Figure 3.12 MRGW characteristic impedance with a gap filled with $\epsilon r1 > \epsilon r2$: (a) Case X and (b) Case Y.....	26
Figure 3.13 MRGW characteristic impedance errors with an air gap: (a) Case A, (b) Case B, (c) Case C, and (d) Case D.	26
Figure 3.14 MRGW characteristic impedance errors with a gap filled with $\epsilon r1 < \epsilon r2$: (a) Case E, (b) Case F, (c) Case G, and (d) Case H.	27
Figure 3.15 MRGW characteristic impedance errors with a gap filled with $\epsilon r1 > \epsilon r2$: (a) Case X and (b) Case Y.....	27

Figure 3.16 Effective dielectric constant and characteristic impedance with a gap filled with $\epsilon r_1 = \epsilon r_2$ (Case Z).....	28
Figure 3.17 Effect of thickness on MRGW width.	28
Figure 4.1 Antenna array of $N \times N$ in XY-plane and equivalent circuit of one element.....	32
Figure 4.2 Construction of 8x8 and 16x16 array from 4x4 array.	33
Figure 4.3 Mutual admittance matrix arrangement (a) 4x4 element array and (b) constructed for the 8x8 element array.....	34
Figure 4.4 Dispersion diagram of MRGW.	35
Figure 4.5 Fig. Structure of PRGW ME-dipole antenna.	35
Figure 4.6 Simulated reflection coefficient of the ME-dipole antenna.	36
Figure 4.7 Input impedance of ME-dipole antenna.	36
Figure 4.8 64 Elements arrangement to calculate effective input impedances.....	37
Figure 4.9 Effective impedance of 8x8-element array using the 4x4-element array at 57 GHz.....	38
Figure 4.10 Effective impedance of 8x8-element array using the 4x4-element array at 60 GHz.....	38
Figure 4.11 Effective impedance of 8x8-element array using the 4x4-element array at 64 GHz.	38
Figure 4.12 (a) Feed network structure of the 8x8-element array, (b) 8x8-element array full structure with the ME-dipole elements.	39
Figure 4.13 Reflection coefficient of 8 x 8 ME-dipole antenna arrays.	40
Figure 4.14 Normalized radiation patterns of the ME-dipole antenna at 57 GHz.....	42
Figure 4.15 Normalized radiation patterns of the ME-dipole antenna at 60 GHz.....	42
Figure 4.16 Normalized radiation patterns of the ME-dipole antenna at 64 GHz.....	42
Figure 4.17 Normalized radiation patterns of the 8x8-element array at 57 GHz (E-plane).	43
Figure 4.18 Normalized radiation patterns of the 8x8-element array at 60 GHz (E-plane).	43
Figure 4.19 Normalized radiation patterns of the 8x8-element array at 64 GHz (E-plane).	43
Figure 4.20 Normalized radiation patterns of the 8x8-element array at 57 GHz (H-plane).....	44
Figure 4.21 Normalized radiation patterns of the 8x8-element array at 60 GHz (H-plane).....	44
Figure 4.22 Normalized radiation patterns of the 8x8-element array at 64 GHz (H-plane).....	44
Figure 4.23 Full-wave simulated gain compared to those calculated based on different cases (A, B, and C) and total radiation efficiencies of the 8x8 element array antenna.	45

Figure 4.24 Effective impedance of 16x16-element array using the 4x4-element and 8x8-element array at 57 GHz.	46
Figure 4.25 Effective impedance of 16x16-element array using the 4x4-element and 8x8-element array at 60 GHz.	46
Figure 4.26 Effective impedance of 16x16-element array using the 4x4-element and 8x8-element array at 64 GHz.	46
Figure 4.27 MRGW to WR-15 transition: (a) side view, (b) 3D geometry (top metallic layer is hidden).	47
Figure 4.28 Reflection coefficient of the transition from WR-15 to MRGW.	48
Figure 4.29 Sub-array optimization for 16x16 array.	49
Figure 4.30 Quarter of feeding network of 16x16 array antenna.	50
Figure 4.31 Simulated reflection and transmission coefficients of the power divider I, the power divider II and the power divider III.	50
Figure 4.32 Photos of different parts of fabricated antenna: (a) the AMC metal pin layer, (b) the feed network layer, and (c) the radiating layer.	51
Figure 4.33 Reflection coefficient of 16 x 16 with ME-dipole antennas (actual loads) and effective impedances loads for optimizing the feed network.	51
Figure 4.34 Normalized radiation patterns of the 16x16-element array at 57 GHz (E-plane).	53
Figure 4.35 Normalized radiation patterns of the 16x16-element array at 60 GHz (E-plane).	53
Figure 4.36 Normalized radiation patterns of the 16x16-element array at 64 GHz (E-plane).	53
Figure 4.37 Normalized radiation patterns of the 16x16-element array at 57 GHz (H-plane).	54
Figure 4.38 Normalized radiation patterns of the 16x16-element array at 60 GHz (H-plane).	54
Figure 4.39 Normalized radiation patterns of the 16x16-element array at 64 GHz (H-plane).	54
Figure 4.40 Full-wave simulated gain compared to different Cases (A, B, and C) and total radiation efficiencies of the 16x16 element array antenna.	55
Figure 4.41 Radiation pattern of a 4x4 antenna array in different environments, (a) subarray at the corner (embedded), (b) subarray in the middle (embedded).	57
Figure 4.42 Radiation pattern of an 8x8 antenna array with a different number of failure element	58
Figure 5.1 Schematic of the EM-dipole with the MRGW (a = 0.976 mm, b = 0.896 mm, c = 0.096 mm, d = 1.137 mm, e=0.85mm, f=0.565mm and g=0.44mm).	61

Figure 5.2 Simulated S-parameters gain and AR of the circular polarization ME- dipole antenna.	62
Figure 5.3 Radiation patterns of the ME-dipole antenna (xz-plane).	62
Figure 5.4 Radiation patterns of the ME-dipole antenna (yz-plane).	63
Figure 5.5 Geometry of the 8×8 antenna array with the feeding network of MRGW:(a) differential, (b)all in phase.....	63
Figure 5.6 Arrangement of the 8×8 array to calculate the effective input impedances.	64
Figure 5.7 Effective impedance of 8×8 -element array using 4×4 -element array at 57 GHz.....	65
Figure 5.8 Effective impedance of 8×8 -element array using 4×4 -element array at 60 GHz.....	65
Figure 5.9 Power divider structures: (a) power Divider I, (b) power Divider II and (c) power Divider III.	65
Figure 5.10 Simulated reflection and transmission coefficients of the power.....	66
Figure 5.11 Schematic of the EM-dipole with the MRGW ($a = 1.02$ mm, $b = 0.807$ mm, $c = 0.117$ mm, $d = 1.288$ mm, $e=0.699$ mm, $f=0.58$ mm and $g=0.44$ mm).	66
Figure 5.12 Reflection coefficient and AR of the 8×8 antenna array.	67
Figure 5.13 Simulated gain and radiation efficiency of the 8×8 antenna.	67
Figure 5.14 Radiation patterns of the 8×8 array in xz-plane at (a) 57GHz, (b) 60GHz, and (c) 64GHz..	68
Figure 5.15 Radiation patterns of the 8×8 array in yz-plane at (a) 57GHz, (b) 60GHz, and (c) at 64GHz.	69
Figure 6.1 mm-Wave Indoor network architecture.....	73
Figure 6.2 Configuration of the 8×8 -element array antenna.....	75
Figure 6.3 Simulated S-parameters of an 8×8 antenna array.....	76
Figure 6.4 Simulated gain from the full-wave and total radiation efficiency of the 8×8 element array antenna.	76
Figure 6.5 E-plane radiation patterns of the 8×8 array at frequencies 57, 60, 63, and 66 GHz.....	77
Figure 6.6 H-plane radiation patterns of the 8×8 array at frequencies 57, 60, 63, and 66 GHz.	77
Figure 6.7 45° -plane radiation patterns of the 8×8 array at and frequencies 57, 60, 63, and 66 GHz.	78
Figure 6.8 Orthogonal 4×4 MIMO antenna design with the electric field direction in the coupling slot at each subarray.	79
Figure 6.9 Simulated S-parameters of the four sub-array antenna.	79
Figure 6.10 Simulated S-parameters (isolation) between the ports of the four subarray antennas.	80

Figure 6.11 Simulated gain from the full-wave and total radiation efficiency of the four subarray antennas.....	81
Figure 6.12 Envelope correlation coefficient between four sub-array antennas	81
Figure 6.13 Schematic of the EM-dipole with the superstrate RO3006 and the MRGW.	83
Figure 6.14 Simulated S11 and gain from the full-wave using a single ME-dipole antenna with different superstrates.....	84
Figure 6.15 Radiation patterns of the single ME-dipole using dielectric superstrate RO3006. All are normalized to the gain at 60 GHz: (a) E-plane (b) H-plane.....	84
Figure 6.16 Radiation patterns of the single ME-dipole using dielectric superstrate RO3010. All are normalized to the gain at 64 GHz: (a) E-plane (b) H-plane.....	85
Figure 6.17 Schematic of the 2×2 ME-dipole with one dielectric superstrate and the MRGW.	86
Figure 6.18 Simulated S11 and gain from the full-wave using 2×2 antenna array with one dielectric superstrate.	87
Figure 6.19 Radiation patterns of the 2×2 ME-dipole antennas using one dielectric superstrate. All are normalized to the gain at 60 GHz: (a) E-plane (b) H-plane.....	87
Figure 6.20 Schematic of the 2×2 EM-dipole with two dielectric superstrates and the MRGW.	88
Figure 6.21 Simulated S11 and gain from the full-wave using 2×2 antenna array with two dielectric superstrates.....	89
Figure 6.22 Radiation patterns of the 2×2 ME-dipole antennas using two dielectric superstrates. All are normalized to the gain at 64 GHz: (a) E-plane (b) H-plane.....	89
Figure 6.23 Schematic of the 4×4 EM-dipole with two dielectric superstrates and the MRGW.	90
Figure 6.24 ME dipole antenna dimensions ($a = 1.02 \text{ mm}$, $b = 1.1 \text{ mm}$, $c = 1.19 \text{ mm}$, $e = 0.1 \text{ mm}$, and $d = 0.66 \text{ mm}$).....	91
Figure 6.25 Simulated S11 and gain from the full-wave using 4×4 antenna arrays with two dielectric superstrates.....	91
Figure 6.26 Radiation patterns of the 4×4 ME-dipole antennas using the two dielectric superstrates: (a) 57 GHz, (b) 60 GHz, and (c) 64 GHz.	92
Figure 6.27. 3dB hybrid coupler structure.	95
Figure 6.28. Simulated MRGW hybrid coupler scattering parameters.	95
Figure 6.29. Simulated differential phase characteristics of the MRGW.	95

Figure 6.30. The monopulse comparator structure.	96
Figure 6.31. Simulated reflection coefficients of the comparator network: (a) mode 1, (b) mode 2, (c) mode 3 and (d) mode 4.	97
Figure 6.32. Simulated phase variation of the comparator network: (a) mode 1, (b) mode 2, and (c) mode 3.....	97
Figure 6.33. 8x8 antenna array of the monopulse comparator structure.....	98
Figure 6.34. Simulated reflection coefficients of the 8x8 antenna array.	98
Figure 6.35. Simulated reflection coefficients of the port isolation of the 8x8 antenna array.....	99
Figure 6.36. Operating mechanism of the 8x8 monopulse array antenna.	99
Figure 6.37. Radiation patterns of the 8×8 monopulse antenna array at 57GHz.....	100
Figure 6.38. Radiation patterns of the 8×8 monopulse antenna array at 60GHz.....	100
Figure 6.39. Radiation patterns of the 8×8 monopulse antenna array at 64GHz.....	101
Figure 6.40. MIMO system based on 8×8 antenna and monopulse.....	102
Figure 6.41. Mode coupling between two MIMO system at: (a) 8 cm, (b) 20 cm, (c) 38 cm, and (d) 60 cm.....	103
Figure 6.42. Channel capacity of a monopulse MIMO system.	104

List of Symbols

λ	Wavelength
λ_0	Wavelength in free space
ϵ_0	Permittivity of free space, 8.854×10^{-12} F/m
ϵ_r	Relative permittivity of medium
ϵ_{r-eff}	Effective relative permittivity of medium
c	Speed of electromagnetic waves in vacuum ($2.99792458E8$ m/s)
dB	Decibels
GHz	Gigahertz
S	S-parameter
$\tan\delta$	Loss tangent
η_0	Intrinsic impedance of free space
Ω	Ohms
Z_0	Characteristic impedance

List of Acronyms

3D	Three Dimensional
AMC	Artificial Magnetic Conductor
BW	Bandwidth
CPW	Coplanar Waveguide
CST MWS	Computer Simulation Technology Microwave Studio
EBG	Electromagnetic Band Gap
EM	Electro-Magnetic
LTCC	Low-Temperature Co-fired Ceramic
MM-Wave	Millimeter Wave
PCB	Printed Circuit Board
PMC	Perfect Magnetic Conductor
PRGW	Printed Ridge Gap Waveguide
RGW	Ridge Gap Waveguide
SIW	Substrate Integrated Waveguide
SLL	Side Lobe Level
TE	Transverse Electric
TEM	Transverse Electromagnetic
TM	Transverse Magnetic

Chapter 1: INTRODUCTION

1.1 Introduction

Current wireless and mobile communication systems use a frequency range between 800MHz and 3GHz, including different telecommunication generation (2G/3G and 4G) and Wireless Local Area Networks (WLAN) for indoor communications. Using these frequency bands has less attenuation and can provide long distance coverage. However, the upcoming communication systems and (IoT) require tremendous data rates. In other words, the focus of future technology is on data capacity rather than coverage, where many users can utilize a large amount of capacity simultaneously and efficiently. Obtaining high data rates can be realized through the millimeter-wave band (mm-wave) [1][2]. Wave propagation at mm-wave is vulnerable to atmospheric absorption and attenuation; it is useful for indoor application and short-range applications. However, using mm-wave for long distances can take place along with other technologies, such as massive multiple-input multiple-output (MIMO) and beamforming [3]. MIMO and beamforming play a vital role in future communication systems. They provide channel orthogonality, which is also required to increase the channel capacity and isolate the channels in MIMO systems. Mm-wave Technologies are the candidates that are expected to be mostly used for the next communication systems. Hence, the antenna with high gain and a more directive beam is required [3]. Some unlicensed frequency bands such as the 60-GHz band (57-64 GHz), the 76-81 GHz band, and above 100 GHz are good candidates for the fifth-generation (5G) and the upcoming communication systems. In contrast, designing electric components in the mm-wave frequency is challenging and more complicated since the dimensions become very small. Electromagnetic waveguiding structures that are used to realize these components play an essential role, especially in the mm-wave frequency range, and have a direct effect on the component performance where low loss, small profile, less interference, and high efficiency are needed. Therefore, significant attention has been focused on researches around mm-wave to validate new technologies that can be used for designing future communication systems [3] [4].

1.2 Millimeter-Wave and waveguide problems

The mm-wave frequency band includes frequencies from 30 to 300 GHz. Recently, the V-band (57-64GHz) has received increased interest and attention because of the unlicensed bands, large available bandwidth, and the ability to provide a high gain antenna with small physical dimensions. Some applications such as high-quality video transmission, WiGig (Wireless Gigabit) [4, 5], and automotive

radars and sensor systems [6] are popular nowadays using unlicensed mm-wave frequency bands (60 GHz and 30GHz bands). Moreover, Mm-wave systems are proposed to be used for point-to-point wireless communication links as backhaul in base stations using LTE 4G cellular services in high-density areas [7]. In addition, mm-wave gigabit broadband (MGB) solution that provides gigabit-per-second links to mobile small cells and fixed broadband access points was proposed [3]. Nevertheless, designing for the radio frequency (RF) front end at mm-wave frequencies creates technological and mechanical challenges. Since the guidance structures for the wave propagation are playing a crucial role at mm-wave, conventional metallic waveguides have been used to design with low loss and high performance. However, at mm-wave frequencies, the design for the feed network becomes more complicated and difficult for manufacturing, especially the electrical contact between the metals [8] [9]. On the other hand, planar microstrip technologies are used for implementing antenna array feed networks at mm-wave because of many advantages such as a low cost, compact profile structure, easy fabrication, and manufacturing [10]. However, dielectric losses, radiation loss, and surface waves are the most frequently encountered obstacles in the design using Microstrip technologies [11]. These losses have a direct effect in reducing the radiation efficiency and gain. Substrate integrated waveguide (SIW) is another guiding structure, which was introduced in [12]. SIW resembles waveguide technologies. However, the electromagnetic waves are propagating through the dielectric material with metal on the top and bottom, and the side walls are realized by two rows of metalized via holes on the left and right side [13]. SIW provides similar advantages to the conventional metallic waveguide. However, these guide structures suffer from dielectric loss, which could be unacceptable at millimeter-waves; accurate via holes placements are required. Dielectric material with low loss tangent can be used to reduce the dielectric losses, but dielectric materials with low losses might increase the cost. The limitation of these guidance structures can be overcome, especially at millimeter-wave frequency range through the gap waveguide technology that has been introduced in [14-18]. Gap waveguide (GWG) technologies have shown exemplary performance in the mm-wave bands and have proven to be a good candidate and an alternative for the conventional guiding technologies. Gap waveguide technologies provide some advantages compared to other technologies. GWG parts don't need to be electrically connected. Furthermore, propagating waves are quasi-TEM waves, which means less dispersive compared to the waveguides that are required to keep the signal integrity. Most of the field is confined along the ridge in the direction of the propagation, which means no radiation losses due to the self-packaged nature of the guiding structure.

Therefore, the mutual coupling between the components has less effect, and more components can be placed adjacently, which provides a compact and small size.

1.3 Problem statement and work motivation

One of the main requirements for the next generation of wireless communication devices is compactness and low profile. In other words, more components should be placed close to each other. Therefore, the technology that should be used to design such components must provide good isolation between these different components (low interference) and must be easily manufactured and fabricated. Microstrip Ridge Gap Waveguide (MRGW) is one of the promising versions of the ridge gap waveguide. However, one of the main problems to design using MRGW is the absence of closed-form expressions to calculate or synthesize the characteristic impedance and the effective dielectric constant. Therefore, the design of these lines and components, such as power dividers, delay lines, and hybrids, is based on optimization tools. In addition, MRGW can be used to design high gain antenna arrays. However, the design of such antenna arrays can be challenging to meet the high performance required in terms of high gain and efficiency with less complexity, especially at mm-wave frequencies. The complexity is mainly caused by compensating for the effect of mutual coupling. Particularly, in the phased array, the mutual coupling between the radiating elements has a noticeable effect. The spacing between the array elements is less than half a wavelength to avoid grating lobes. The surface and space waves are the main contributors to the mutual coupling between the radiating elements. Therefore, an efficient design procedure for designing a large finite array feeding network is required, including the effect of mutual coupling by considering the effective input impedance of each element of the array. The design of large arrays can be achieved with less computational and processing time without the need for the full-wave analysis. In consequence, designing a large antenna array efficiently, including the mutual coupling effect, can reduce the complexity of the massive MIMO antenna system. Basically, in a massive MIMO, a huge number of antennas (antenna array, especially at mm-wave frequencies) act as a single element in order to achieve the required gain.

1.4 Objectives

The main objective is designing high gain antenna arrays at mm-wave to be used in 5G applications and MIMO systems at 60GHz. the design procedures for the high gain antenna need to be efficient and reliable

when the full-wave simulations have limited resources to process and simulate large antenna systems. The process to realize these objectives can be described as follows:

- MRGW is the electromagnetic waveguide that will be used to design the antenna array systems. Consequently, an efficient modeling and design tool for the MRGW needs to be proposed to provide closed-form empirical expressions for the effective dielectric constant and characteristic impedance.
- A new method will be used to predict the performance of a large finite array from a small array, including the effect of the mutual coupling between the elements. The method will provide us with the radiation characteristics of the large array as well as the effective impedance (active impedance) of all the array elements at its port. Then, this information is used to design the corporate feeding network as terminating loads without the need to introduce the radiating elements in the computation and then introducing an efficient design procedure of the large finite array feeding network. The procedure is applicable to any feeding network technology. The procedure will be applied to design an 8×8 and 16×16 antenna array with Single-Layered Corporate-Feed besides an 8×8 circular polarized antenna array based on MRGW at 60GHz.
- Using the method in (2), a high gain 4×4 MIMO antenna system will be designed for a 60 GHz band using MRGW for the indoor application that can be used at the physical layer (front end of the radio frequency (RF)) for 5G WIFI devices.
- In addition, design a high gain antenna array using super dielectric substrate and a limited number of radiating elements 2×2 and 4×4 array with gain equivalent to 4×4 and 8×8 antenna array gain. The antenna array will be designed using corporate feed based on MRGW technology for 60 GHz band applications with spacing between the elements exceeds one wavelength and suppressed grating lobes.
- To design a 3dB hybrid coupler that can be used to design a comparator system. The comparator contains a radiation part of an 8×8 antenna array and provides four independent channels through pattern orthogonality that can be used as a MIMO antenna system.

1.5 Contribution and Novelty

In this work, the main contributions of this work can be summarized as follows:

- 1) Analysis and synthesis formulas for the MRGW to facilitate the design process.

- 2) Provide empirical expressions for the effective dielectric constant and characteristic impedance for several possible configurations of the MRGW.
- 3) Demonstrate the validity of the proposed formulas for various cases of the MRGW.
- 4) Verify the method of predicting the performance of a large finite array from a small array for certain bandwidth. The method provides us with the radiation characteristics of the large array as well as the effective impedance (active impedance) of all the array elements at their ports. Then, this information is used to design the corporate feeding network as terminating loads instead of a conventional matching load, which avoids the need to make the design in the presence of the radiating elements in the computation. Facilitate using three different 3-port MRGW that allow avoiding some bends in the feeding network that deteriorate its performance.
- 5) A rectangular waveguide transition to the MRGW provides a differential phase power division from the rectangular waveguide to the MRWG.
- 6) Finally, an efficient design procedure of the large finite array feeding network is introduced. The procedure is applicable to any feeding network technology. The procedure is applied to a microstrip ridge gap waveguide (MRGW) to design an 8x8 and 16x16 antenna array with linear polarization and an 8x8 circular polarized antenna array.

It is worth emphasizing that the procedure in [2] depends on the knowledge of the mutual admittance matrix (it could be the scattering parameters or the mutual impedance matrix) of the small array that can be obtained from a full-wave solution or measurements. Then, the effective input impedance of each element of the array is used to separately design the feeding network by using the radiating elements as the loads terminating the feeding network. Therefore, large array processing time is reduced because the radiators are excluded from the numerical solution to reduce the numerical domain to the internal domain of the feeding network. Therefore, the optimization process could be implemented on the feeding network only. Then the appropriate design of the feeding network structure can be obtained to minimize the radiation and surface wave losses. From the active voltage terminal of the elements, an array factor, including the mutual coupling, can be computed to predict the radiation patterns as well as the array gain. This analysis gives useful estimations of the array performance under different scenarios in which we can design the proper feeding networks. Besides, the use of commercial full-wave simulation tools, such as CST, in designing large array becomes more efficient and faster. Lastly, the concept is used to design 8x8 and 16x16 antenna arrays of ME-dipole with high gain and high efficiency based on MRGW. The antenna array design to cover the bandwidth of 57–64 GHz with a feeding network and radiating layers only and overcomes the problem of introducing the cavity layer. Moreover, less computation time and memory consumption are needed.

Chapter 2: GAP WAVEGUIDE TECHNOLOGY

2.1 Introduction

Materials with electric conductivity are physically present in nature (metals). However, materials with magnetic conductivity do not physically exist. Therefore, researchers have artificially realized these surfaces using periodic structures. These structures are frequency dependent and should be designed for the specified frequency band.

2.2 Soft and Hard Surfaces

Soft and hard surfaces with anisotropic properties can be considered as metamaterials that satisfy the condition of the Magnetic Conductor. The anisotropic properties provide high surface impedance, which cut off the wave with a specific direction of propagation. In which case, soft surfaces suppress the electromagnetic waves from propagating, and hard surfaces allow the waves to propagate [19] [20]. Basically, the idea of soft and hard surfaces has been realized by corrugated structures where ground strips or corrugations with a height of quarter guided wavelength, as shown in Fig. 2.1.

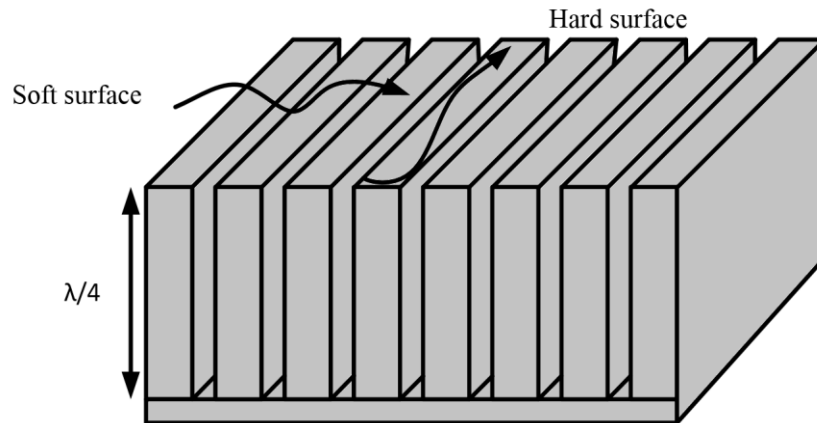


Figure 2.1 Soft and hard surfaces realized with corrugations.

The main idea has been developed from the transmission line concept, such that the short circuit becomes an open circuit at the surface of the corrugation. As a result, a high anisotropic surface impedance (high in the transverse direction of the corrugation acting as an artificial magnetic conductor and zero along the corrugations) is generated and stop all the waves from propagating within a specific frequency band. Corrugated surfaces can be considered as a 1D bandgap configuration that can provide high impedance (soft) in one direction (for wave propagation transverse to the corrugation wall) and low impedance (hard) for wave propagation along the corrugation wall. In addition, the bandgap can be in 2D configurations

(periodic structures) to provide a higher degree of freedom for high surface impedance implementation [21] [22]. In other words, 2D bandgap structures can manipulate the electromagnetic signals to cut off the waves from propagating isotopically within a specific frequency band.

2.3 The Gap Waveguide Theory

Consider two parallel plates, as shown in Fig. 2.2, PEC plate above the PMC plate with spacing (d) between them. According to Maxwell equations for transverse electric (TE), electric and magnetic fields traveling in the $+z$ direction satisfy the following equations [23]:

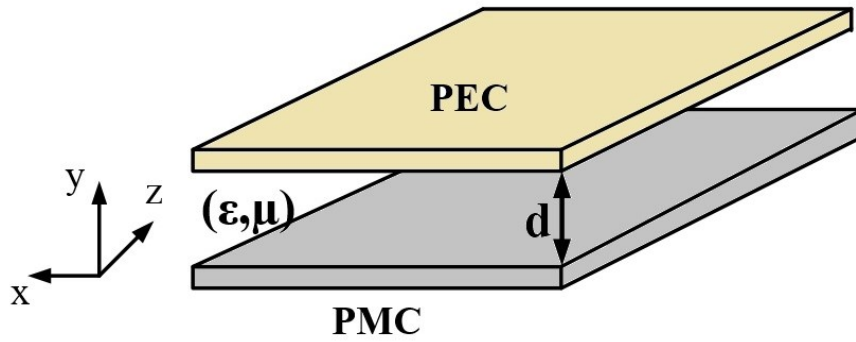


Figure 2.2 Gap waveguides concept with ideal PEC-PMC parallel-plates.

$$E_x = -\frac{1}{\varepsilon} \frac{\partial F_z}{\partial y} \quad (2.1)$$

$$E_y = \frac{1}{\varepsilon} \frac{\partial F_z}{\partial x} \quad (2.2)$$

$$E_z = 0 \quad (2.3)$$

$$H_x = -j \frac{1}{\omega \mu \varepsilon} \frac{\partial^2 F_z}{\partial x \partial z} \quad (2.4)$$

$$H_y = -j \frac{1}{\omega \mu \varepsilon} \frac{\partial^2 F_z}{\partial y \partial z} \quad (2.5)$$

$$H_z = -j \frac{1}{\omega \mu \varepsilon} \left(\frac{\partial^2}{\partial z^2} + \beta^2 \right) F_z \quad (2.6)$$

where $F_z(x, y, z)$ is the z -component of the electric vector potential in the rectangular coordinate system that must satisfy [23]:

$$\nabla^2 F_Z(x, y, z) + \beta^2 F_Z(x, y, z) = 0 \quad (2.7)$$

which can be expressed as:

$$\frac{\partial^2 F_Z}{\partial x^2} + \frac{\partial^2 F_Z}{\partial y^2} + \frac{\partial^2 F_Z}{\partial z^2} + \beta^2 F_Z = 0 \quad (2.8)$$

To simplify the analysis, we consider no variation in the x-direction and the width in the x-direction is infinite, so that $\frac{\partial^2}{\partial x^2} = 0$. Then the solution for $F_Z(x, y, z)$ can be obtained using separation of variables as [23]:

$$F_Z(x, y, z) = k(y)g(z) \quad (2.8)$$

$$\beta_y^2 + \beta_z^2 = \beta^2 \quad (2.9)$$

where β_y and β_z are the wave constants in y- and z-directions, respectively. Since the wave is bounded in the y-direction, then the solution for $k(y)$ represents standing wave while $g(z)$ travelling wave, thus,

$$F_Z(x, y, z) = [A \cos(\beta_y y) + B \sin(\beta_y y)] e^{-i\beta_z z} \quad (2.9)$$

By substituting (2.9) in (2.6) and (2.1) and apply the boundary conditions on the bottom (PMC) and top (PEC) plates, we obtained:

$$H_z(y = 0, z) = 0 \quad (2.10)$$

$$E_x(y = d, z) = 0 \quad (2.11)$$

Then the solution can be written as:

$$F_Z(x, y, z) = [B' \sin(\beta_y y)] e^{-i\beta_z z} \quad (2.12)$$

$$\beta_y = (2n + 1) \frac{\pi}{2d} \quad n = 0, 1, 2, \dots \quad (2.13)$$

where B' is constant. From (2.12) β_z must be greater than zero for propagation. However, to cut off the propagation, the field must be attenuated (Evanescence waves are exponentially decaying fields); this implies that β_z must be imaginary:

$$\beta_z^2 = \beta^2 - \beta_y^2 \rightarrow \left(\frac{2\pi}{\lambda}\right)^2 - \left(\frac{\pi}{2d}\right)^2 < 0 \quad (n = 0)$$

$$d < \frac{\lambda}{4} \quad (2.14)$$

The distance between these two plates controls the propagated waves, such that if this distance is smaller than a quarter wavelength, then all parallel-plate modes are stopped from propagation. Also, when PMC is used, the bandgap acts as a high pass filter, which allows the propagation until the cutoff frequency.

However, when the PMC is realized as an artificial magnetic conductor (AMC), the bandgap acts as a bandstop filter, which creates another cutoff at a lower frequency. This concept is used to realize the ridge gap waveguide (RGW). It should also be clear that the TE case is entirely dual for the TM case. Therefore, the condition of attenuation is valid for the TM case as well. The ridge gap waveguide (RGW), in summary, is based on an air gap sandwiched between two parallel conducting plates where most of the fields (The parallel-plate TEM modes) are confined. The parallel-plate TEM waves are the modes that propagate when the parallel plates are both PECs. To assure that most of the fields are confined between the parallel plates, soft surfaces can cut-off the parallel-plate modes from propagating in one direction (anisotropic). However, it is necessary that all the waves must be prohibited from propagation off the PEC/PEC parallel plates. To achieve that electromagnetic bandgap (EBG), surfaces are used to realize the PMC condition artificially, which provide a high impedance surface [24] to stop parallel plate modes and surface waves from traveling within a frequency range in all directions (isotropic characteristics) when d is less than a quarter wavelength as shown in Fig. 2.3.

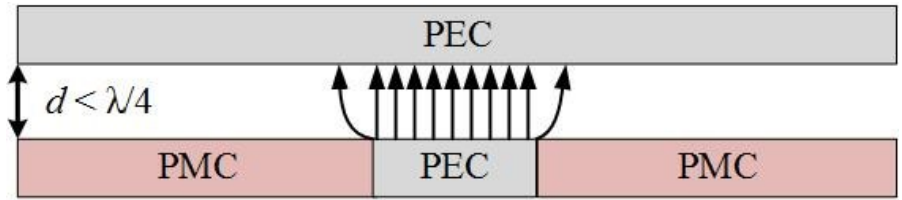


Figure 2.3 Gap waveguide's basic structure.

Hence, the bottom plate has a smooth continuous metal (ridge) surrounded by textured surfaces acting as AMC; a flat metal plate covers all. The distance between these two parallel plates should be smaller than a quarter wavelength, which creates a high impedance condition [25] to stop and cut-off the waves over the textured surface and only allows it between the two smooth top and bottom metals; forcing the field to be guided along the required direction only reduces the radiation loss. In addition, since the wave is attenuated (cut-off) along the other undesired direction, then maintaining good metal contacts is no longer necessary.

Furthermore, the main advantages of this technology are the alleviation of dielectric losses, surface wave suppression, and resolving the electrical contact between metals. The AMC implementation has been realized using different approaches. It can be implemented using a metal pin (bed of nails) [26] or using

mushroom patches [27], in which case it is referred to as printed RGW (PRGW) [28]. A different version of the ridge gap can be made based on the AMC, as indicated in Fig. 2.4; for example, in the ridge gap and groove gap waveguides, metal pins are used without the dielectric.

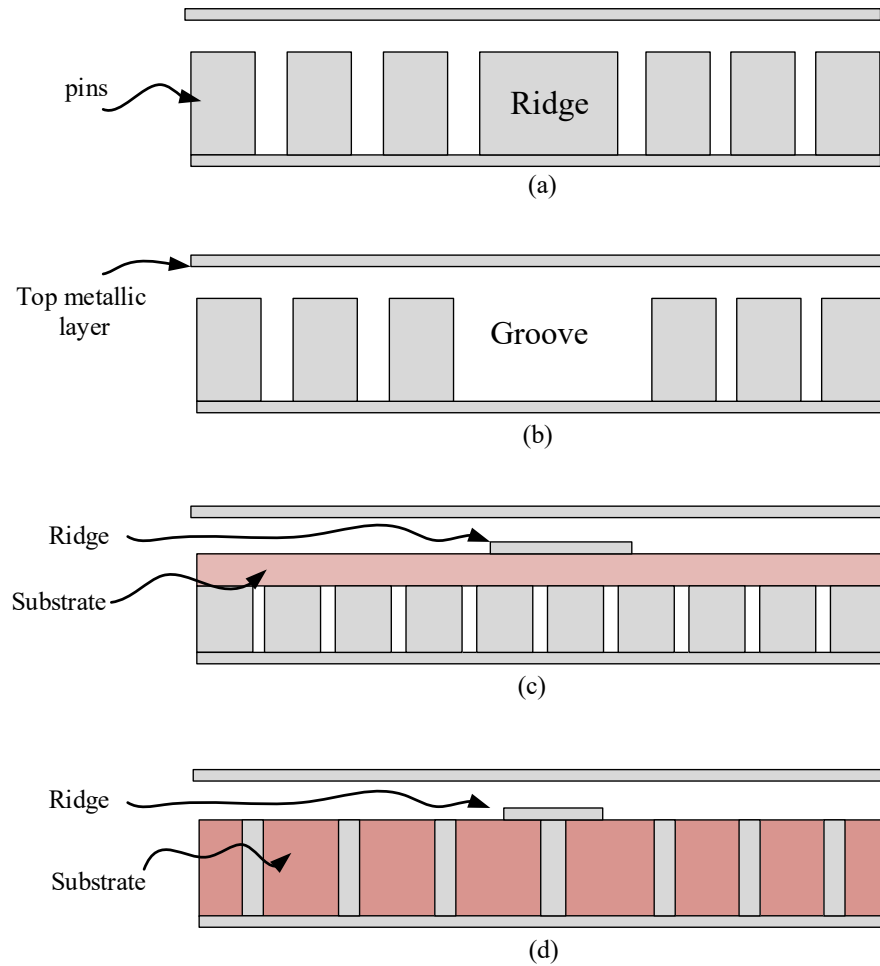


Figure 2.4 Gap waveguides: (a) Ridge gap waveguide, (b) Groove gap waveguide, (c) Microstrip ridge gap waveguide, and (d) Printed ridge gap waveguide.

However, the propagating mode in the ridge gap is the quasi-transverse electromagnetic mode (quasi-TEM) because part of the field (fringing) experience a different propagation environment. On the other hand, the propagating mode in the groove gap is the TE_{10} mode, which resembles the conventional metallic waveguide. Different mm-Wave devices using groove gap waveguides have been reported, such as antennas [29–35], filters [36–42], and diplexers [43–46] with good performance. Another version of the ridge gap is an inverted microstrip gap waveguide [47], which is close to the inverted microstrip lines.

However, the main field propagates in the air gap between the ridge and the upper metal plate. It is worth mentioning that within the stopband of the AMC, the parallel modes and surface waves are cut-off. Furthermore, RGW and PRGW have also been used to design a different kind of components in mm-wave, as reported in [14] [48-49]. RGW and PRGW have a problem of making arbitrary circuits, with bends and discontinuities, disturb the bed of nails and mushroom periodicity, which requires adjusting the nails or the mushroom positions. To avoid such a problem, the ridgeline is elevated up away from the bed of nails or mushroom surfaces without the need to connect the ridge surface to the ground and spacing between them with a thin low dielectric constant substrate. As such, the periodicity of the bed of nails or mushrooms is not disturbed. In addition, the air gap can be filled with dielectric materials, which is advisable to be of low dielectric constant to keep the wideband characteristics of the guiding structure. In this case, a microstrip circuit with all the needed discontinuities can be printed on a grounded substrate and then flipped to face the periodic texture. Such a structure is referred to as the inverted microstrip line, as the signal is propagating in the dielectric substrate of the microstrip line. The inverted microstrip structure is considered as a packaged microstrip line [50], which was treated in several publications [51-55]. These are very complicated structures to be analyzed and designed. However, they have received significant interest because of merging the advantages of the metallic waveguides, in terms of low losses, with the advantages of microstrip technologies; in terms of compact size and ease of fabrication. Hence, it can be a preferred candidate for feeding network design at the mm-frequency range.

**Chapter 3: MODELING AND DESIGN
EMPIRICAL FORMULAS OF MICROSTRIP
RIDGE GAP WAVEGUIDE (MRGW)**

3.1 Introduction

MRGW can be considered as a parallel plate waveguide filled with air or dielectric with a thickness (d) and relative permittivity (ϵ_{r1}); or a microstrip line with a possible air substrate. The inner conductor surface of the microstrip line is the surface of the ridge. The microstrip line (ridge) is elevated above the AMC surface by a dielectric spacer that has relative permittivity (ϵ_{r2}) and thickness (t). The geometry of the MRGW is presented in Fig. 3.1, which can be seen as an inverted microstrip line enclosed with an AMC. The electric field is mostly within the air gap. However, some of the fringing field lines are in the substrate. Therefore, the propagating mode is not a pure transverse electromagnetic mode (TEM) but quasi-TEM. In addition, the substrate material underneath the ridge is nonmagnetic with unity relative magnetic permeability (i.e., $\mu = 1$). An attractive advantage of MRGW configurations with an air gap is that the effective dielectric constant is much smaller than the spacer dielectric constant. Therefore, the loss tangent is substantially reduced, and the component dimensions can be increased, which gives more flexibility in the design at mm-wave frequencies.

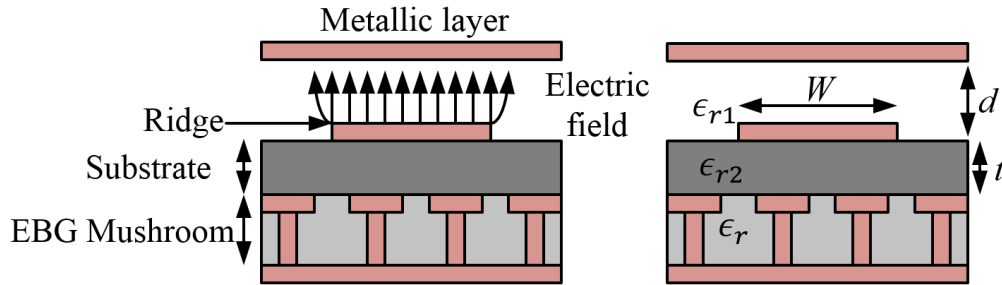


Figure 3.1 Microstrip Ridge Gap Waveguide (MRGW) structure with Electromagnetic Band Gap (EBG) mushrooms with arrows indicate the field lines of the quasi-TEM mode.

3.2 Impedance Design Formulas

The characteristic impedance equation of the quasi-TEM mode [56], propagating along the MRGW, can be express as:

$$Z_c = \frac{120\pi d}{\sqrt{\epsilon_{r-eff}} W_{eff}} \quad (3.1)$$

where W_{eff} is the effective width of the line, and ϵ_{r-eff} is the effective dielectric constant of the guiding medium. Inspired by the microstrip line analysis expressions, it should be stated that the above expression assumes that the physical parameters are known to get W_{eff} and ϵ_{r-eff} . Both W_{eff} and ϵ_{r-eff} are represented in empirical expressions that contain the rational functions of the physical parameters. Using a nonlinear curve fitting routine to a microstrip-like, W_{eff} can be expressed as such:

$$\frac{W_{eff}}{d} = \frac{W}{d} \left(\frac{d}{t} + 1 \right) 0.438 + 1.1 \ln \left[3.708 + \frac{W}{d} \left(\frac{d}{t} + 1 \right) \right] \quad (3.2)$$

The effective dielectric constant ϵ_{r-eff} can be computed by treating the MRGW geometrical configuration as a parallel plate capacitor. Analyzing the effective dielectric constant using this method is similar to the method that has been used by Wheeler for the standard microstrip [57].

However, here we considered the effect of the closed structure with AMC. In order to find an accurate empirical expression to estimate ϵ_{r-eff} , we define a function $F(d, W)$ and $G(d, W, t)$ to compensate for the capacitance effect between the top metal, ridge, and mushroom such that:

$$\epsilon_{r-eff} = \frac{\epsilon_{r1} + \epsilon_{r2}}{2} F(d, w) + \frac{\epsilon_{r1} - \epsilon_{r2}}{2} G(d, w, t) \quad (3.3)$$

Using a non-linear curve fitting routine to a microstrip-like ϵ_{r-eff} can be expressed as:

- If $\epsilon_{r1}=1$

$$\epsilon_{r-eff} = \frac{\sqrt{\epsilon_{r2} + \epsilon_{r1}}}{2} \left[1 + 0.0001 \left(\frac{W}{d} \right)^{1.011} \right] - \frac{\sqrt{\epsilon_{r2} - \epsilon_{r1}}}{2} \left[\left(1 - 0.322 \left(\frac{d}{W} \right) + 2.598 \left(\frac{t}{W} \right) \right)^{-1.91} - 1.025 \left(1 + 0.876 \left(\frac{W}{t} \right) \right)^{-1.197} \right] \quad (3.4)$$

- If $1 < \epsilon_{r1} \leq \epsilon_{r2}$

$$\epsilon_{r-eff} = \frac{\epsilon_{r1} + \epsilon_{r2}}{2} \left[1 + 0.001 \left(\frac{W}{d} \right)^{1.369} \right] - \frac{\epsilon_{r2} - \epsilon_{r1}}{2} \left[\left(1 - 0.904 \left(\frac{d}{W} \right) + 2.096 \left(\frac{t}{W} \right) \right)^{-0.069} - 0.534 \left(1 + 0.206 \left(\frac{W}{t} \right) \right)^{-1.672} \right] \quad (3.5)$$

- If $\epsilon_{r1} > \epsilon_{r2}$

$$\epsilon_{r-eff} = \frac{\epsilon_{r1} + \epsilon_{r2}}{2} \left[1 - 0.0004 \left(\frac{W}{d} \right)^{0.987} \right] - \frac{\epsilon_{r2} - \epsilon_{r1}}{2} \left[\left(1 - 1.428 \left(\frac{d}{W} \right) + 1.572 \left(\frac{t}{W} \right) \right)^{-0.141} - 0.714 \left(1 + 0.126 \left(\frac{W}{t} \right) \right)^{-1.986} \right] \quad (3.6)$$

3.3 Width Design Formulas

An expression for width design can be obtained empirically in terms of rational functions of the physical parameters and the dielectric constant of the material via non-linear curve fitting. Consequently, the MRGW width can be obtained for a given Z_c viz:

- $\epsilon_{r1}=1$

$$\left(\frac{W}{d}\right) = \frac{3.414}{\pi} [A + 0.062 - \ln(3.181A + 1.663) - 0.266 \ln(A - 1.369)] \quad (3.7)$$

- If $1 < \epsilon_{r1} \leq \epsilon_{r2}$

$$\left(\frac{W}{d}\right) = \frac{3.361}{\pi} [A - 0.392 - \ln(0.361A + 3.681) - 0.354 \ln(A - 1.283)] \quad (3.8)$$

- If $\epsilon_{r1} > \epsilon_{r2}$

$$\left(\frac{W}{d}\right) = \frac{3.02}{\pi} [A - 1.544 - \ln(3.447A - 1.933) + 1.35 \ln(A + 1.484)] \quad (3.9)$$

$$A = \frac{120\pi}{\sqrt{\epsilon_{r1}} Z_c} \quad (3.10)$$

The analysis and synthesis equations are found to be accurate with a maximum error of 6% from the exact theoretical data over the range $\epsilon_{r1} \leq 6.15$, $\epsilon_{r2} \leq 10.2$, $0.2 < \frac{t}{d} \leq 1$, and $0.1 < \frac{W}{d} \leq 2$. The MRGW ridge thickness can affect the characteristic impedance and the effective dielectric constant since both are being functions of the MRGW width. According to [58], thick microstrip $0.05 < \frac{t_h}{h_m} \leq 0.2$ is used for the transmission lines that can be used for quasi-DC operations. However, the thin line $0.01 < \frac{t_h}{h_m} \leq 0.05$ is used for the microwave devices, where h_m is the thickness of the substrate in the conventional microstrip line. Similarly, MRGW can be used to design the transmission line for quasi-DC and microwave devices. Therefore, the closed-form expressions for the width (W_h), considering the effect of the thickness (t_h), can be obtained empirically as such:

$$\left(\frac{W_h}{d}\right) = \frac{W}{d} + \frac{0.8t_h}{d\pi} \left[1 + \ln\left(\frac{2d}{t_h}\right)\right] \quad (3.11)$$

In [59], it has been noticed that Z_c value decreases as the strip thickness increases. Therefore, the effect of the finite thickness of the MRGW line may be thought of as an increase in width. Equation (3.11) is similar to the one used for the conventional microstrip in [60]. However, different coefficients are used in

(3.11) since the estimation of W_d in MRWG is different from the conventional microstrip line. When the line thickness is considered, the W term in (3.2), (3.4), (3.5), and (3.6) needs to be replaced by W_h , which can be obtained from (3.11). A flow chart that illustrates the curve fitting process is shown in Fig 3.2.

3.4 Port Definition and Data Extraction

The definition of the waveguide port used for MRWG is similar to the definition in [61], with port width dimensions of at least one-unit cell period p from both sides of the MRGW line in the transverse direction. Hence, most of the fields (confined and fringing) are considered. Also, the port length is designed to cover the gap region d substrate t and half of the mushroom pin height (h) in the longitudinal direction, as shown in Fig. 3.2. The propagation constant β and Z_c can be obtained directly from the waveguide port information using full-wave analysis at a specific frequency. The relation between β and ϵ_{eff} can be found in [62] for quasi-TEM. Then the empirical expressions are developed by using curve fitting.

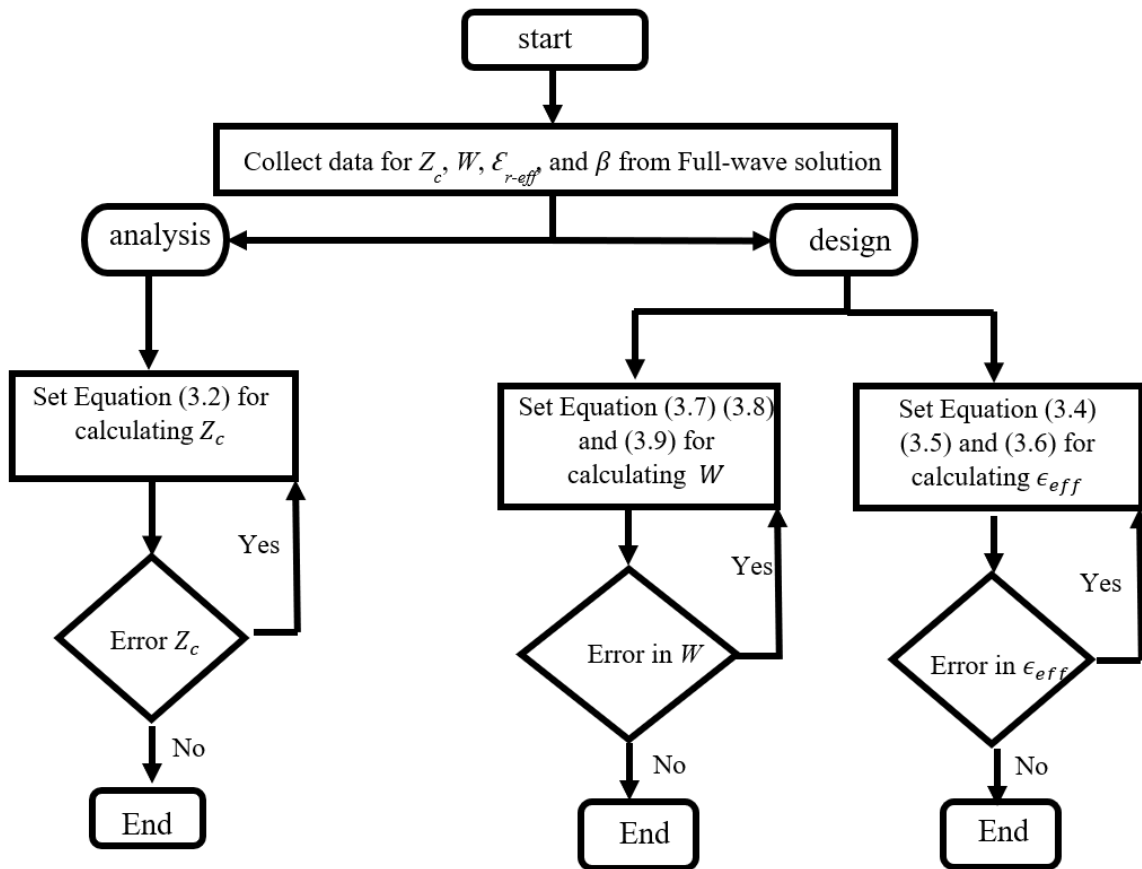


Figure 3.2 Flow chart for the curve fitting.

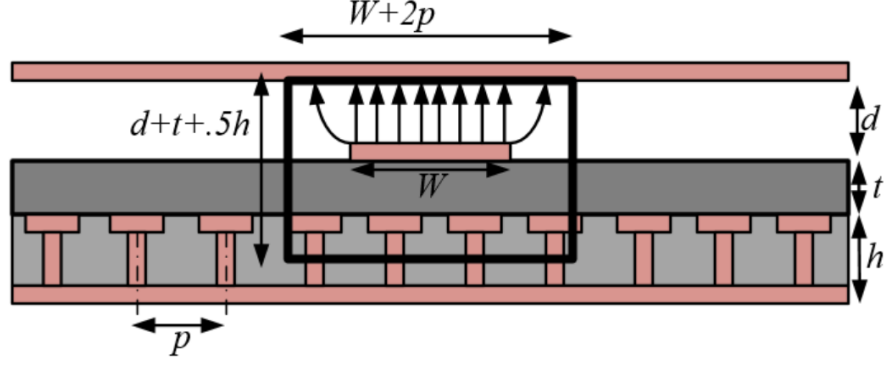


Figure 3.3 Port definition for MRGW.

3.5 Equations Verification

To verify the proposed formulas, different cases have been studied based on ϵ_{r1} and ϵ_{r2} . First, the case when ϵ_{r1} is air, the MRGW structure in [38] is used. The unit cells are designed to provide a stopband between 20-40 GHz loaded with $\epsilon_r=3$. The unit cell with $\epsilon_{r2}=3$ is used in case A. On the other hand, a unit cell for stopband 50-80 GHz with $\epsilon_{r2}=3$ is also used with the thickness = 0.13 mm and air gap = 0.18 mm. The mushroom is designed with radius = 0.7 mm, via diameter = 0.33 mm, period = 0.85 mm and loaded with $\epsilon_r=3$ in case B. Moreover, a unit cell for stopband 10-20 GHz with $\epsilon_{r2}=3$ is also used with the thickness = 0.508 mm, and the air gap = 0.508 mm. The mushroom is designed with radius = 1.3 mm, via diameter = 0.3 mm, period = 3 mm and loaded with $\epsilon_r=3$ in case C. The same dimensions that used in case C are used for case D; however, with $\epsilon_{r2}=6.15$ is used. Then, ϵ_{eff} is calculated using (3.4) and compared with the full-wave analysis of the different cases (A, B, C, D) at the center frequencies 30 GHz, 60 GHz, and 14 GHz, respectively. The variation of ϵ_{eff} with $\frac{W}{d}$ is shown in Fig 3.4. It may be observed that the empirical expressions are in good agreement with the full-wave analysis results within a maximum error of less than 5%, as shown in Fig 3.5. In addition, it may be noticed that the value of ϵ_{eff} gets close to one when the width of the MRGW line increases because most of the electric field becomes more confined within the air gap. From the different cases, it can be observed that the approximation of using $\epsilon_{eff}=1$ is no longer valid, especially when the value of ϵ_{r2} is high.

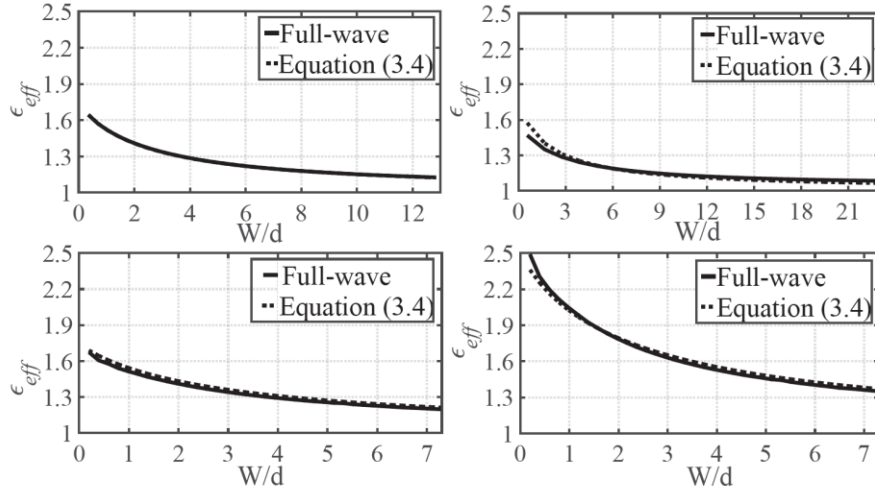


Figure 3.4 Effective dielectric constant when ϵ_{r1} is air: (a) case A, (b) case B, (c) case C, and (d) case D.

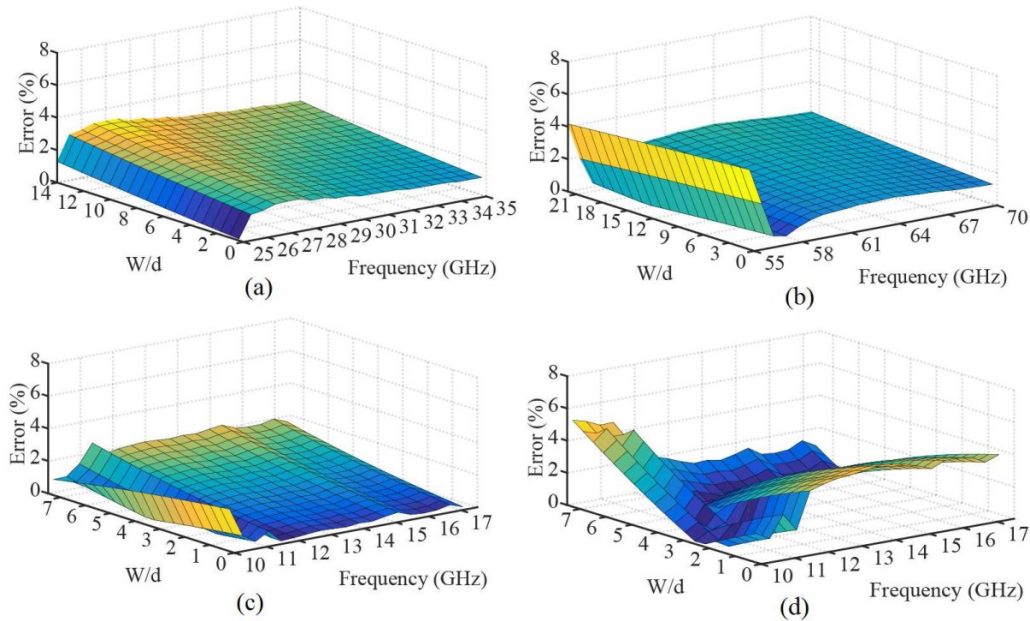


Figure 3.5 Errors when ϵ_{r1} is an air: (a) case A, (b) case B, (c) case C, and (d) case D.

Since the empirical formulas are generalized to accommodate the gap filled with dielectric material, several MRGW unit cells are used for verification. When $\epsilon_{r1} < \epsilon_{r2}$. A unit cell is designed to provide a stop-band between 8-18 GHz. A substrate dielectric material is used with $\epsilon_{r2}=3$ and thickness = 0.508 mm. The gap thickness = 0.508 mm is filled with substrate dielectric material that has $\epsilon_{r1}=2.2$ and $\epsilon_{r1}=1.96$ for case E and case F, respectively. The EBG mushroom has the same dimensions as case C to provide the required stopband. Moreover, another unit cell for the case when $\epsilon_{r1} < \epsilon_{r2}$ are designed to provide stopband between

8-18 GHz with $\epsilon_{r2}= 6.15$ and thicknesses = 0.508 mm. The gap thickness of 0.508 mm is filled with substrate dielectric material that has a permittivity $\epsilon_{r1}=2.2$ and $\epsilon_{r1}= 3$ for case G and case H, respectively. The variation of ϵ_{eff} over the line width at 14 GHz is shown in Fig 3.6. From the results, it may be observed that the value of ϵ_{eff} gets close to the substrate dielectric permittivity filling the gap as the width of MRGW line increases. As expected, most of the electric field becomes more confined within the layer between the top metal and the ridge. The values obtained from the empirical expressions are in good agreement with the full-wave analysis results in a maximum error of 3%, as shown in Fig 3.7. The error has been calculated as an absolute percentage error for the values obtained from the full-wave analysis.

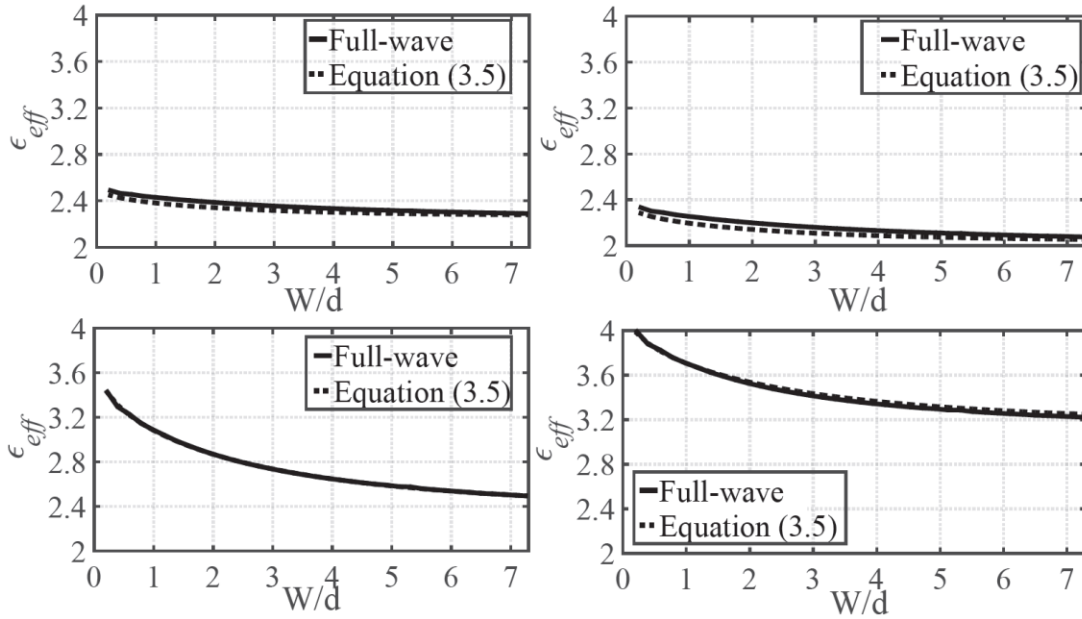


Figure 3.6 Effective dielectric constant when the gap is filled with $\epsilon_{r1} < \epsilon_{r2}$: (a) case E, (b) case F, (c) case G and (d) case H.

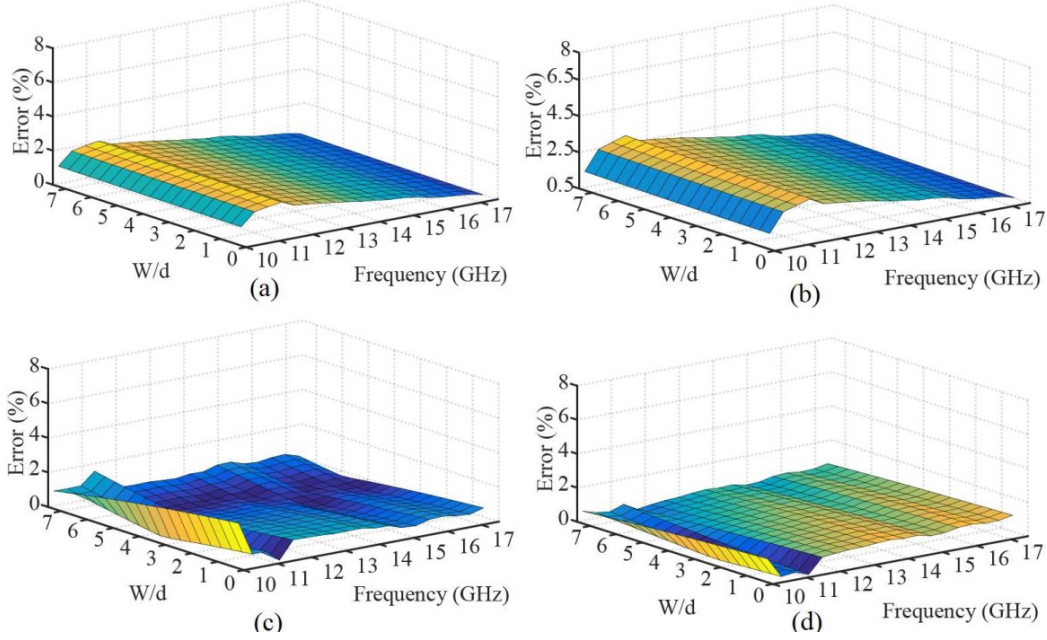


Figure 3.7 Error when the gap filled with $\epsilon_{r1} < \epsilon_{r2}$: (a) case E, (b) case F, (c) case G, and (d) case H.

On the other hand, the case when $\epsilon_{r1} > \epsilon_{r2}$ is verified through different MRGW unit cells. A unit cell is designed to provide stopband between 8-18 GHz with $\epsilon_{r1}=6.15$ and $\epsilon_{r2}=3$ each with thicknesses = 0.508 mm in case X. Another unit cell is designed to provide stopband between 8-18 GHz with $\epsilon_{r1}=10.2$, and $\epsilon_{r2}=3$, and both substrates have thicknesses = 0.508 mm in case Y. The EBG mushroom is designed with the same dimensions as case C. Then, the variation of ϵ_{eff} over the line width at 14 GHz is shown in Fig 3.8. From the results, it may be observed that the value of ϵ_{eff} increases as the line width increases, which is similar to the behavior of the microstrip. The values obtained from the empirical expressions agree with the full-wave analysis results within a maximum error of 2%, as shown in Fig 3.9. The design expressions for the width are also verified by known Z_c . Using the previous unit cell structures, the estimation of MRGW width is calculated using (3.7), (3.8), and (3.9). Figs 3.10 - 3.12 show the characteristic impedance calculated from the full-wave analysis and the empirical expressions. Agreement between the empirical expression and the full-wave results can be observed within a maximum error of less than 8%, as shown in Fig 3.13- 3.15. In addition, as expected, the larger the MRGW width, the lower the characteristic impedance. Besides, in the case of filling the gap with dielectric material, it can be observed that the dimensions (width of the line) are getting smaller for specific Z_c compared with the case of air-filled.

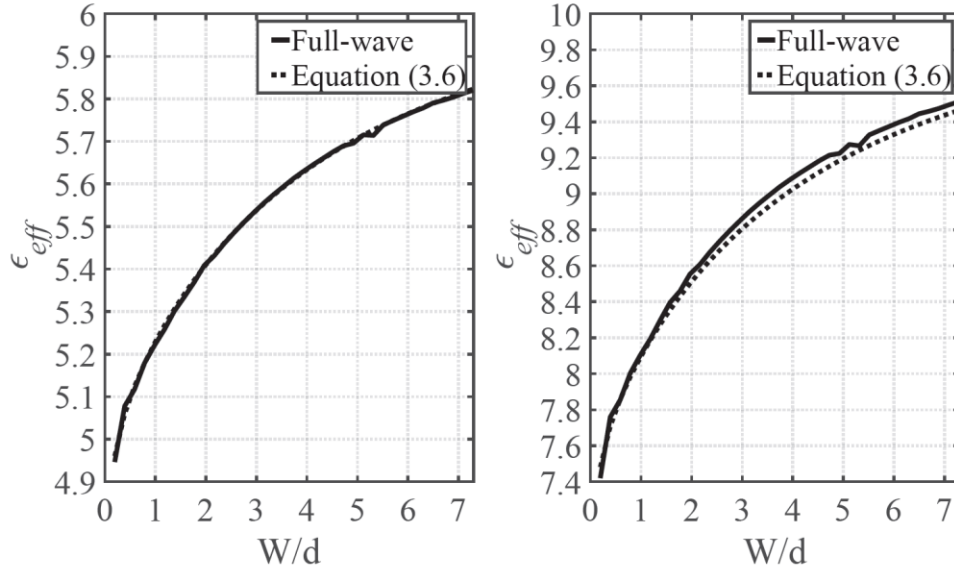


Figure 3.8 Effective dielectric constant when filled with $\epsilon_{r1} > \epsilon_{r2}$: (a) case X, and (b) case Y.

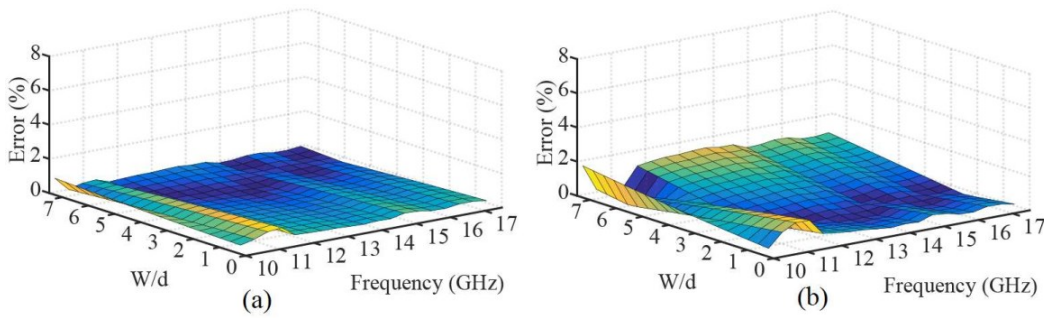


Figure 3.9 Errors when the gap filled $\epsilon_{r1} > \epsilon_{r2}$: (a) case X, and (b) case Y.

It can be observed that the thickness of the dielectric underneath the ridge with ϵ_{r2} has a negligible effect on calculating Z_c since most of the fields are concentrated at the gap between the top metal plate and the ridge. For example, in case C and case D, the thickness of the substrate dielectric underneath the ridge is 0.508 mm with different ϵ_{r2} . But the width for $Z_c=50$ is approximately 2 mm for both. It is essential to mention that case C, case G, and case Y were used for data fitting. However, other cases are used for testing. Finally, for the case with $\epsilon_{r1} = \epsilon_{r2}$, the same dimensions in Case C are used in the unit cell. However, both the gap and the dielectric material underneath the ridge have $\epsilon_{r1} = \epsilon_{r2} = 3$ in case Z. As expected, confined fringing fields within the gap experience the same material such that ϵ_{r-eff} is almost 3, as shown in Fig 3.16.

The effect of MRGW line thickness is verified in Fig. 3.17, where the empirical expression (3.11) is used, and compared with the full-wave analysis, it can be noticed that the change of the width versus MRGW thickness is very small. The width of MRGW in Case A is selected to give 58Ω with zero thickness. However, the thickness variation changes the impedance up to -5Ω . On the other hand, MRGW width, Case B, is selected to give 54Ω with zero thickness. By including the effect of the thickness, up to -3Ω of variation can be observed.

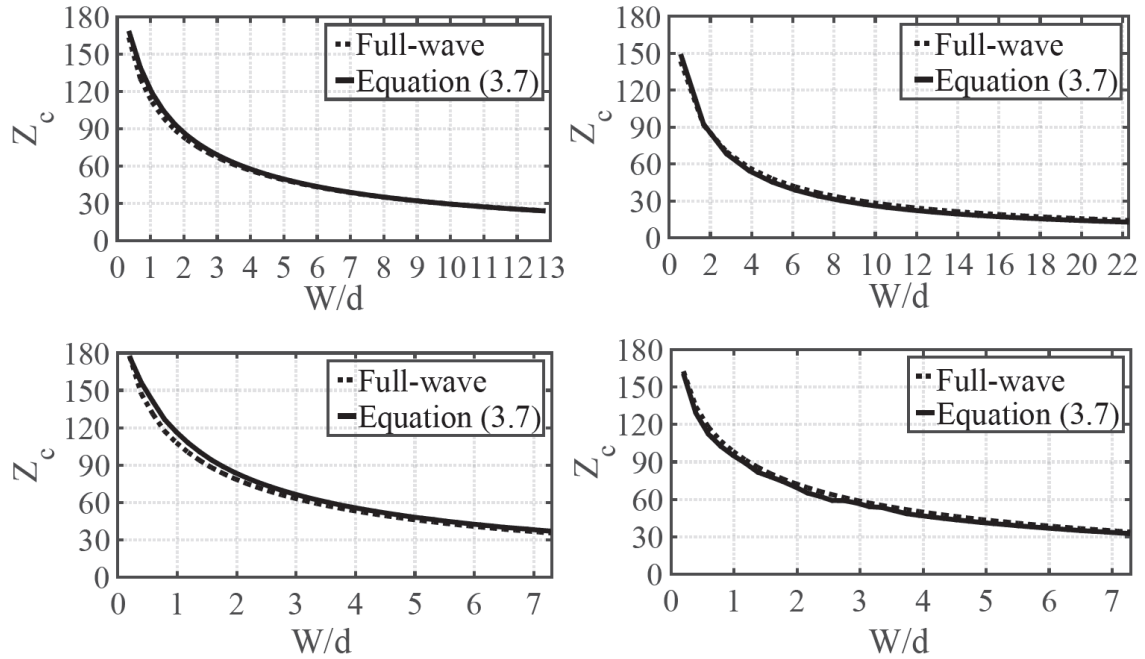


Figure 3.10 MRGW characteristic impedance with an air gap: (a) Case A, (b) Case B, (c) Case C, and (d) Case D.

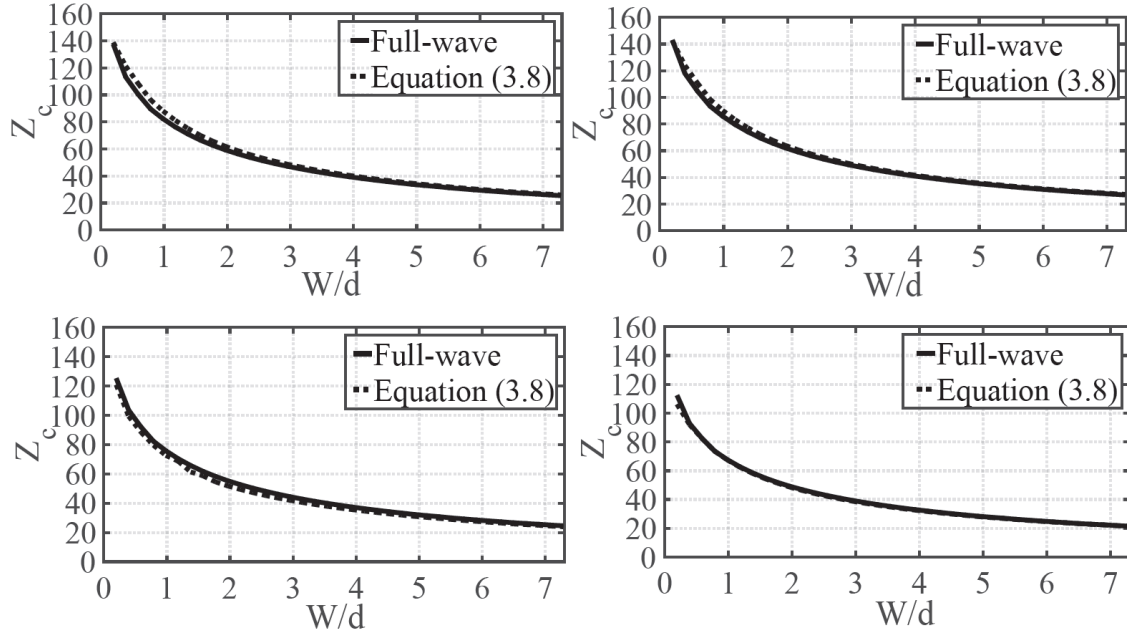


Figure 3.11 MRGW characteristic impedance with a gap filled $\epsilon_{r1} < \epsilon_{r2}$): (a) Case E, (b) Case F, (c) Case G and (d) Case H.

Moreover, a comparison between the present work and previously published work, using MRGW, is conducted by comparing the values obtained from the present model with those used in the other works. In [63], the line width for $Z_c=50$, quarter wavelength transformer length and width were 0.9 mm, 2.5 mm, and 1.6 mm, respectively. However, the values obtained from our model are 1.06 mm, 2.22 mm, and 1.8 mm, respectively. The difference between values obtained by the proposed model and those in [63] is due to the correction used in [63] to account for the discontinuities using optimization. It is worth mentioning that our model values were close to the optimized values, which means that the optimizer starts from a good guess and reduce the processing time. In addition, in [61] where $\frac{t}{d}=2$ the line width for $Z_c=50$ was 0.78 mm, where the value of our model is 0.71 mm. The AMC layer can be implemented using metal pins instead of EBG mushrooms. In [64], the line width for $Z_c=50$ was 1.11 mm, and the value of our model is 1.06 mm. In [14], where MRGW technology is used with metal pins to design a 4×4 planar dual-mode horn array, the line width for $Z_c=50$ was 7.362 mm and from our model is 6.812 mm; whereas for the power divider line width for $Z_c=50$ changed to 8.8 mm. The quarter wavelength transformer length and width for $Z_c=70$ were 6.6 mm and 4.39 mm, respectively. However, the values obtained from our model

are 6.1 mm and 3.5 mm, respectively, at 10.5 GHz. Another line for $Z_c=100$ is used with width 2.4 mm, and the value of our model is 1.6 mm, where the effect of the continuity is not included.

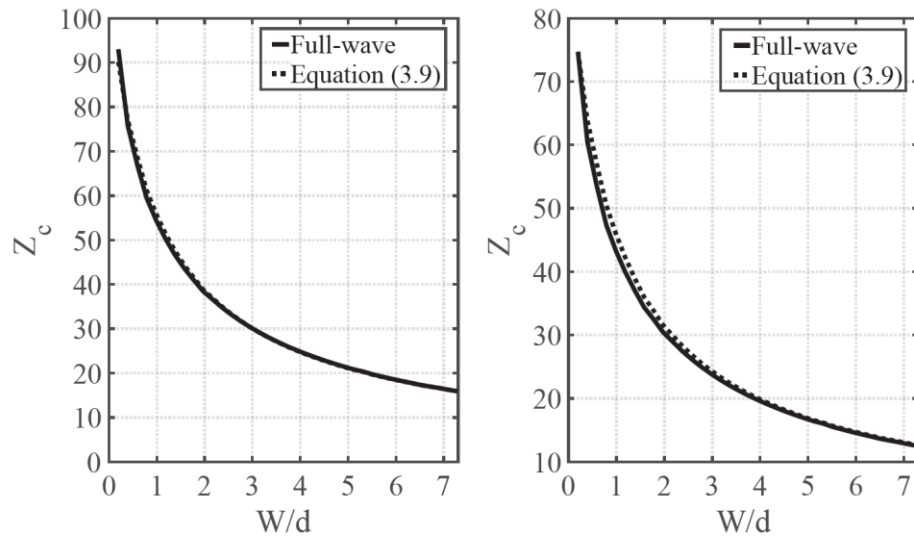


Figure 3.12 MRGW characteristic impedance with a gap filled with $\epsilon_{r1} > \epsilon_{r2}$: (a) Case X and (b) Case Y.

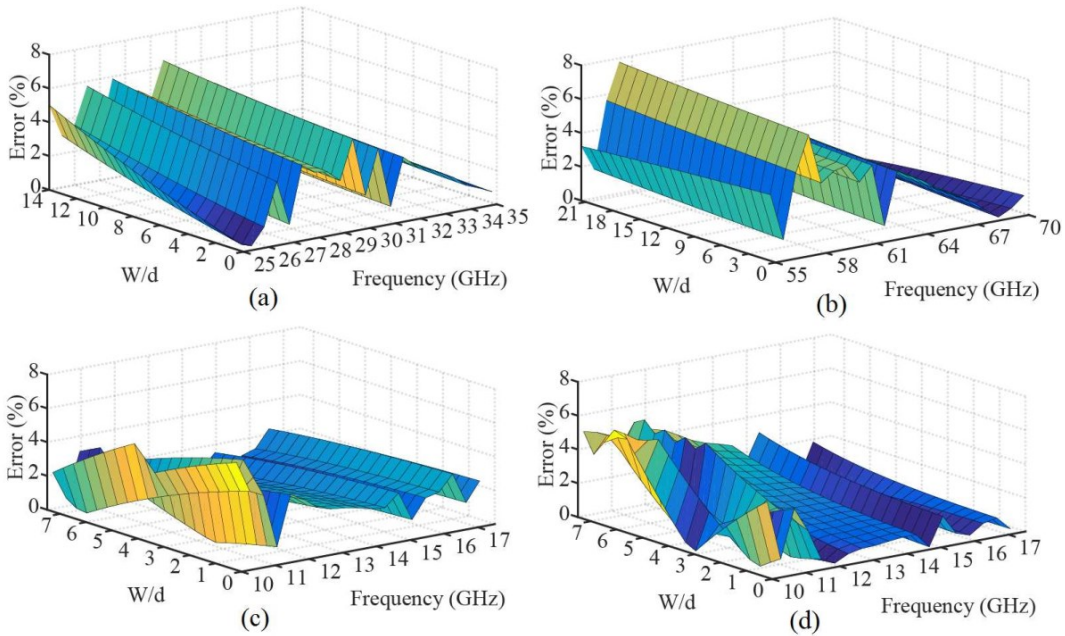


Figure 3.13 MRGW characteristic impedance errors with an air gap: (a) Case A, (b) Case B, (c) Case C, and (d) Case D.

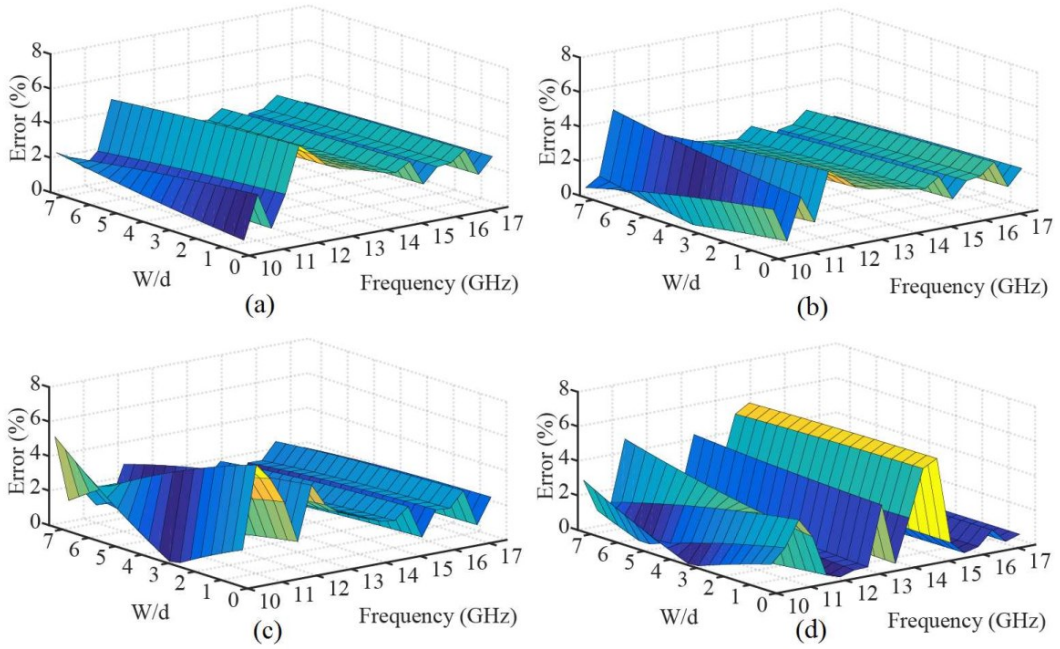


Figure 3.14 MRGW characteristic impedance errors with a gap filled with $\epsilon_{r1} < \epsilon_{r2}$: (a) Case E, (b) Case F, (c) Case G, and (d) Case H.

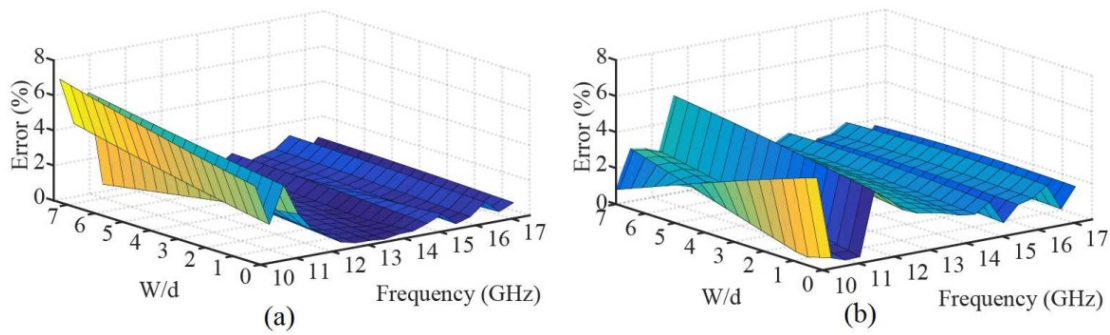


Figure 3.15 MRGW characteristic impedance errors with a gap filled with $\epsilon_{r1} > \epsilon_{r2}$: (a) Case X and (b) Case Y.

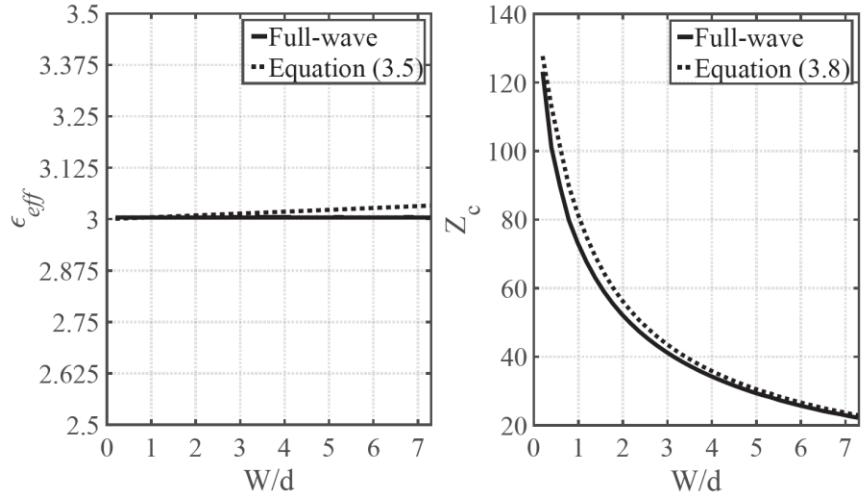


Figure 3.16 Effective dielectric constant and characteristic impedance with a gap filled with $\epsilon_{r1} = \epsilon_{r2}$ (Case Z).

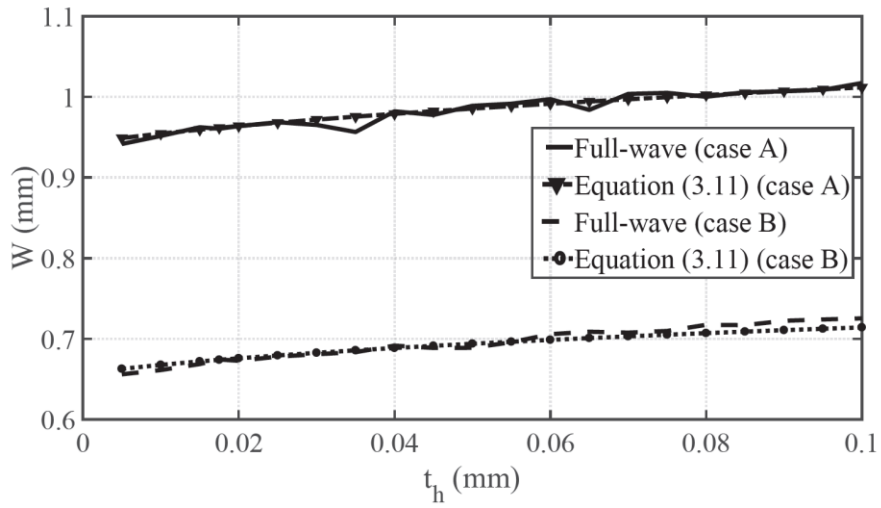


Figure 3.17 Effect of thickness on MRGW width.

Chapter 4: DESIGN LARGE FINITE ARRAY

4.1 Introduction

Phased antenna arrays have received increased attention recently because of their applications in satellite, military, and vehicular communications for high gain [65]. Most of the design procedures for phased arrays start with a study of the radiation characteristics of the single element and then design for the large antenna array structure. However, the environment of a single isolated element is different from that of an array environment where the coupling has a direct effect on the resonance frequency, bandwidth, and the radiated power of each element [66-67]. Besides, the pattern multiplication for an antenna array in [68], which can be used to estimate the far field parameters, is valid when the mutual coupling can be ignored. Practically, in the phased array, the mutual coupling between the radiating elements has a noticeable effect. The spacing between the array elements is less than half a wavelength to avoid grating lobes.

The surface wave is the main contributor to the mutual coupling between the radiating elements. On the other hand, the estimation of the antenna array performance can be improved by including the effects of mutual coupling and considering the effective input impedance in designing the feeding network. The effective (active) input impedance can be defined as the active input impedance of the radiating element in the array environment, which includes the mutual coupling effect. Generally, optimization tools of a full-wave solver can be used to design a large antenna array. However, using optimization is a time consuming and requires huge computing resources, which is costly, especially for the large antenna arrays. There are many different reported techniques in the literature [69-75] for designing large antenna arrays using different numerical techniques. Some of these techniques are for specific array types and elements.

Recently, accurate modeling and analysis to design a large antenna array is reported [76]. However, the procedures are complicated in a way that the mutual coupling needs to be calculated through Fourier integral. Besides, the effect of the mutual coupling is not related to each element port impedance to help in the design of the feeding network. Moreover, the estimation for the radiation patterns requires a minimum of 9 elements pattern to be extracted to consider the effect of the edges and corners, which add more complexity. In [66], a more general and efficient technique was introduced to consider the effect of the mutual coupling regardless of the element type. Furthermore, the presented method can predict array performance for the entire scan range by studying the far field characteristics of the single element in an infinite array numerically, then predict the far field parameters of the large array. Since the edge elements of the array have a different environment than the other antenna elements, it is expected that the edge

elements perform differently. Simulations using the infinite array environment cannot describe the edge effects. Therefore, the edge element effect is considered. Following the procedure in [66], by considering a small array full-wave solution, or measurements to get its Scattering matrix (S-matrix) or admittance matrix (Y-matrix) as an N-port network, where N is the number of elements. Using this matrix of a small array, a similar matrix of a larger array with a similar array lattice can be obtained. The larger matrix is obtained by neglecting the mutual coupling of elements further away than those of the small array. From the S- or Y-matrix of the desired large array, the effective input admittance or input impedance can be obtained.

Moreover, phased antenna arrays with high gain are required, especially for millimeter-wave (mm-Wave) applications. Design such antenna arrays can be challenging to meet high performance in terms of high gain and efficiency with less complexity. Lots of research is performed to design a high gain antenna array [77-80]. The feeding network of the array differs based on the guiding structure used. The Microstrip line technology is known to be highly lossy at mm-wave frequencies and has significant dielectric and radiation losses; however, SIW suffers from dielectric losses since most of the electric field propagates through the dielectric substrate. Therefore, the recently developed ridge gap waveguide (RGW) technology has been used because it is self-package and can be designed to have an air propagating medium, and the line width of the characteristic impedance is narrower than the conventional microstrip lines. However, it was found that this technology requires a significant distance between the guiding lines that prevented having a direct feeding to the array elements with a distance less than a guiding wavelength. To reduce the distance between the radiating elements, the RGW feeding network is used to feed an array of 2×2 subarrays made on a substrate integrated waveguide cavity [78], [81]. In terms of losses between the MRGW and SIW, a quantitative study in [63] has been conducted, and it showed that smaller losses in MRGW than SIW if designed with the same dielectric material.

This has complicated the antenna array by adding an extra layer. As such, optimization takes a long time. In addition, as the subarrays become the elements of the feeding network, it has a higher directivity than the subarray elements, but it becomes vulnerable to the grating lobe in the large broadside arrays. In order to overcome this problem, the microstrip ridge gap waveguide (MRGW) is used, which made it possible to reduce the distance between the feeding network lines and make the distance between the directly fed radiating elements less than the wavelength [64]. However, it was possible to design a 4×4 array achieving the required bandwidth. When the same topology is used to design an 8×8 array, the bandwidth is reduced, and it was difficult to optimize the feeding network to achieve a similar bandwidth. After

careful investigation, we found that the main reason for failing to achieve the required bandwidth is the strong coupling between the terminating stubs with the guiding structures in several positions of the network. Therefore, we have modified the feeding network topology to avoid such coupling.

4.2 Design Large Finite Array theory

Considering an $N \times N$ antenna array with identical elements in XY-plane, as shown in fig 4.1. According to [66], the effective input impedance can be calculated as

$$Z_i^e = R_i \frac{\sum_{j=1}^N A_{ij} V_j}{\sum_{j=1}^N (\delta_{ij} - A_{ij}) V_j} \quad (4.1)$$

$$A_{ij} = [Y_{ij} R_i + \delta_{ij}]^{-1} \quad (4.2)$$

where R_i the input impedance of the isolated element, $\delta_{ij} = 1$ for $i = j$ and zero for $i \neq j$ (element in a row i and column j), V_j the applied voltage and Y_{ij} is the port mutual admittance between the i^{th} and j^{th} radiating elements.

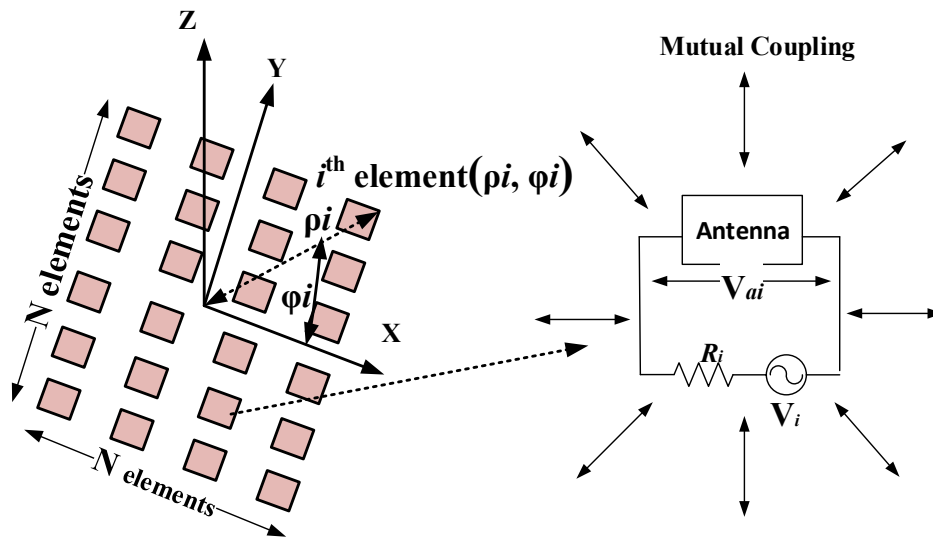


Figure 4.1 Antenna array of $N \times N$ in XY-plane and equivalent circuit of one element.

Then, the effective input impedance of each element of the array is used to design the feeding network by using the radiating elements as the loads terminating the feeding network. Therefore, large array processing time is reduced because the radiators are excluded from the numerical solution to reduce the numerical domain to the internal problem domain. Therefore, the optimization process could be implemented on the feeding network only. Then the appropriate design of the feeding network structure can be obtained to minimize the radiation and surface wave losses. From the active voltage terminal of

the elements, an array factor, including the mutual coupling, can be computed to predict the radiation patterns as well as the array gain. This analysis can give useful estimations of the array performance under different scenarios in which we can design the proper feeding networks. Besides, the use of commercial full-wave simulation tools, such as CST, in designing large array becomes more efficient and faster.

4.3 Mutual Admittance Matrix Construction for a Large Array

The calculation for the effective input impedance in (4.1) requires the mutual admittance for the large array. However, such calculation can be time-consuming; therefore, in [66], a new method to predict this matrix from the small matrix and construct a large array using the small array information as shown in fig. 4.2 where the internal, edge and corner elements have the same environments as the large array.

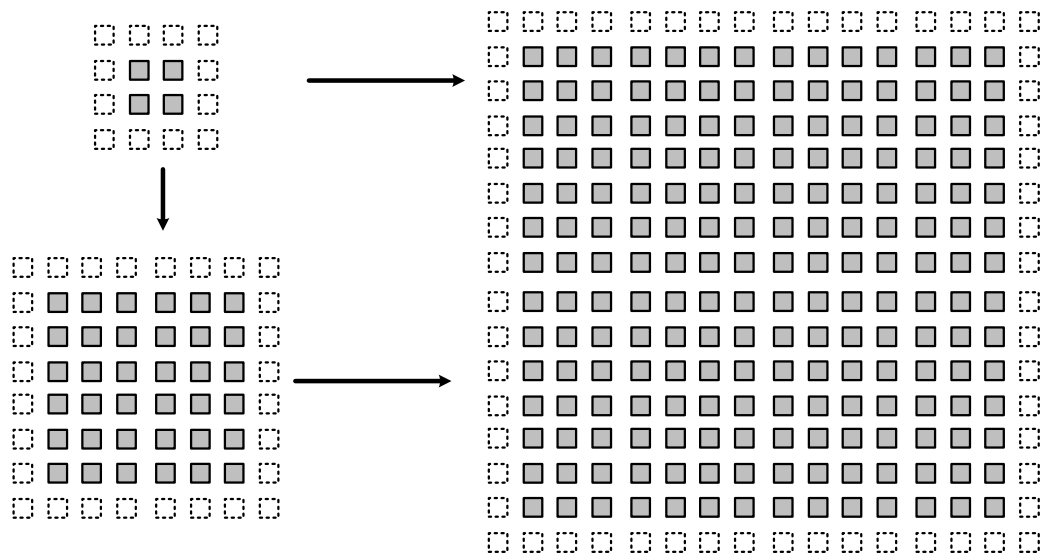


Figure 4.2 Construction of 8x8 and 16x16 array from 4x4 array.

The mutual admittance matrix of 4 x 4 small array can be mapped into the large matrix for 8x8, 16x16, or even larger arrays, as shown in Fig. 4.3. Such mapping reserves a mutual coupling environment of elements with similar relative positions. Thus, a large matrix retains the properties of a small matrix. Also, the mutual coupling is ignored between elements when the distances are greater than three times the spacing between the adjunct elements.

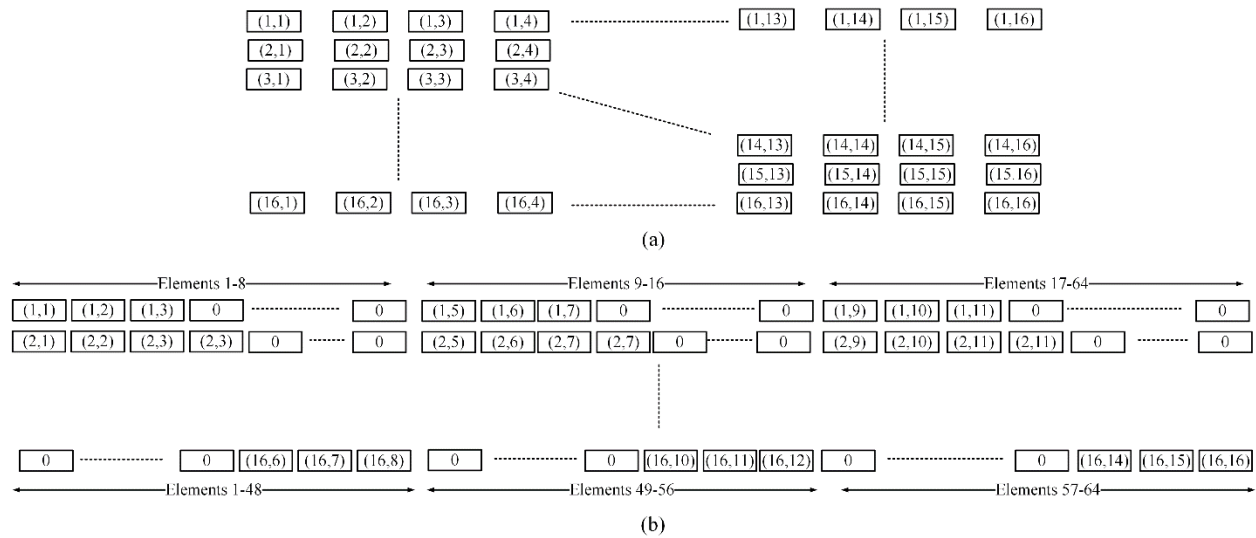


Figure 4.3 Mutual admittance matrix arrangement (a) 4x4element array and (b) constructed for the 8x8element array.

4.4 Effective Input Impedances Calculation for Antenna Array

4.4.1 Basic element design

The design starts with the design of the AMC layer that is realized by periodic structure. The periodic structure unit cell is a metal pin loaded with a thinner dielectric substrate topped with an air gap between its upper surface and an upper conducting plate. The dimensions of pin and cell parameters are selected and adjusted to have an electromagnetic bandgap (EBG) with a central frequency around 60 GHz. AMC layer design for the MRGW with a pin of $0.51 \times 0.51 \times 1.05 \text{ mm}^3$ and a period of 1.1 mm. For the upper layer that accommodates the microstrip line and feeds network, a RO3003 (loss tangent=0.001) is used with a thickness of 0.13 mm. The air gap between the upper substrate and the top metal layer is selected at 0.165 mm to provide an EBG between 46 and 89 GHz. The single-cell dispersion diagram is omitted for brevity. The presence of a microstrip line as a guiding ridge in the center of the EBG structure creates the dispersion diagram given in Fig. 4.4, showing the structure modes. In this figure, the dotted line is the ridge mode indicating its presence within the bandgap of the periodic structure. The presence of the thin dielectric substrate on the bed of the nail does not have an effect on the mode propagation, such as surface waves within the EBG frequency band.

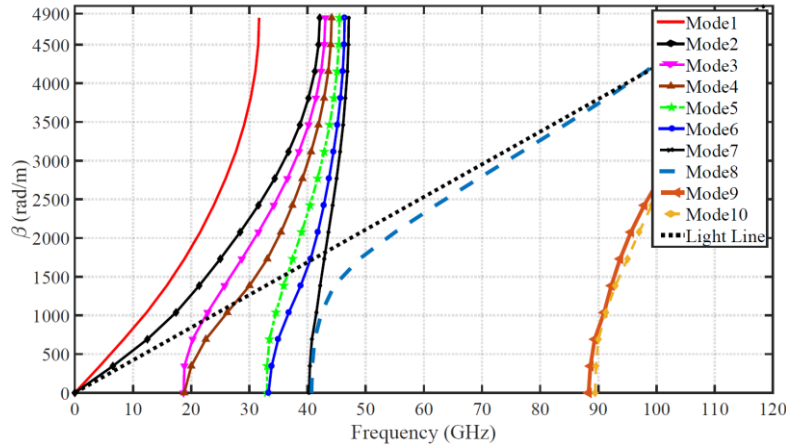


Figure 4.4 Dispersion diagram of MRGW.

The magneto-electric (ME) dipole antenna excited by a narrow slot is considered as the radiating element using *RO4003C* (loss tangent=0.0027) with a thickness of 0.508 mm. A similar design can be found in [64] in the Ka-band and in [82] excited with a slot in a substrate integrated waveguide (SIW). One of the main advantages of the ME is providing a stable gain and radiation pattern across the operating bandwidth [83]. The ME-dipole is designed to work at 60 GHz band and the radiating element in [82] with SIW as a guiding structure. Here, the MRGW is used, as shown in Fig. 4.5. The ME-dipole antenna has a 10 dB matching bandwidth over 19.6% bandwidth (55.3–67.1 GHz), as shown in Fig. 4.6. The input impedance of the ME-dipole antenna is shown in Fig. 4.7, with a gain of 8.8 dBi at 60 GHz.

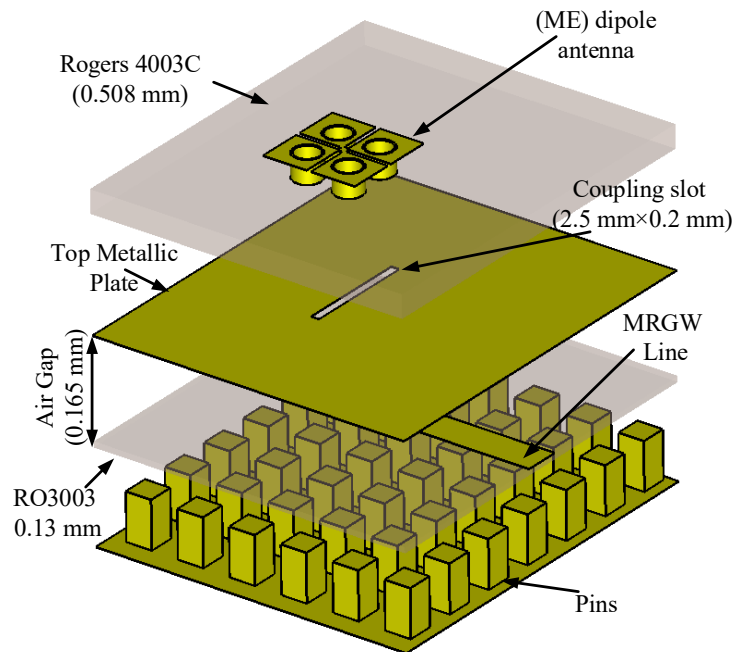


Figure 4.5 Fig. Structure of PRGW ME-dipole antenna.

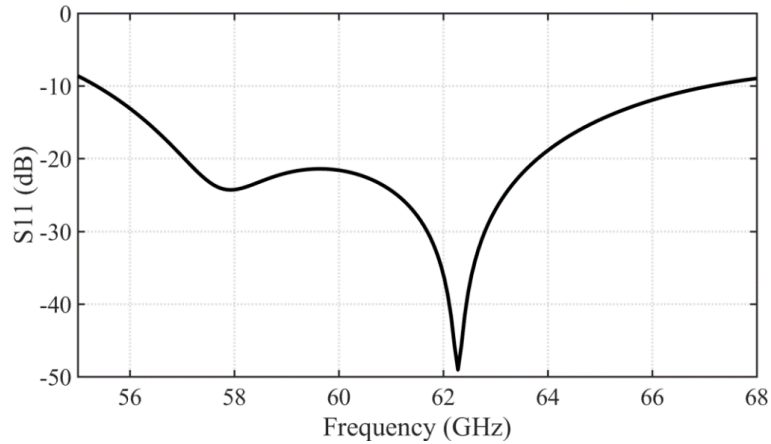


Figure 4.6 Simulated reflection coefficient of the ME-dipole antenna.

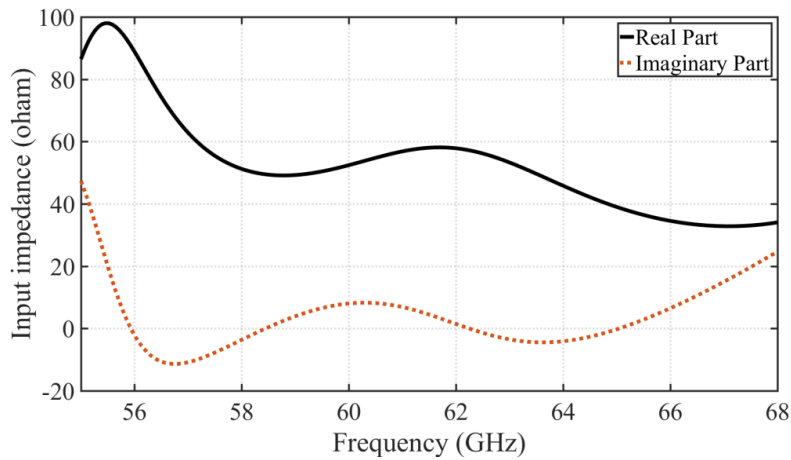


Figure 4.7 Input impedance of ME-dipole antenna.

A 4×4 -element array of ME-dipoles with a separation distance of 4.5 mm between the elements in both x - and y -direction is analyzed using the full-wave simulator of Microwave Studio (CST). Then the obtained mutual admittance matrix is used to construct and estimate the mutual admittance matrix of an 8×8 and 16×16 -element array according to [66]. Finally, the effective impedance for the 64-element array is calculated at different frequencies. Moreover, full-wave simulation is used to obtain the effective impedance for the 64 and 256 elements as actual values and compared with the estimated values calculated by the method in [66]. The element arrangement is shown in Fig. 4.8. Briefly, the procedure for this efficient method to design large antenna arrays can be summarized as follows:

- 1) Select the radiating element and distribute it in a small 4x4 array with the same array lattice of the large array;
- 2) Compute or measure the mutual admittance matrix (Y-matrix) or the S-matrix of the small array;
- 3) Predict the Y-matrix or S-matrix of the large array following the procedure in [66];
- 4) Design the feeding network based on the effective impedances loads that include the mutual coupling effect. Here, only the effective impedances of the elements are used as terminating loads to the feeding network.

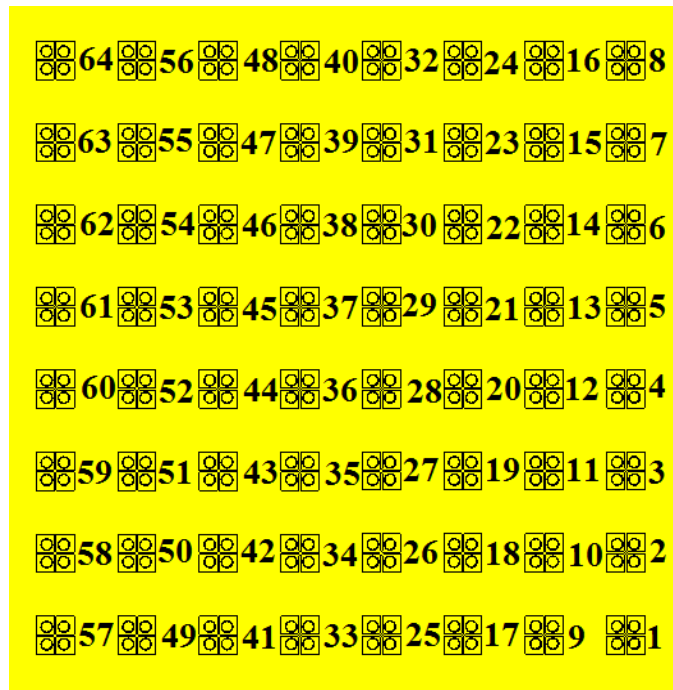


Figure 4.8 64 Elements arrangement to calculate effective input impedances.

4.4.2 8×8 elements for array design

For an 8×8 antenna array, effective input impedances are estimated. It can be pointed out that the edge elements have different characteristics from the central elements, as can be noticed from Fig. 4.9, 4.10, and 4.11 at frequencies 57 GHz, 60 GHz, and 64 GHz, respectively. In other words, the edge elements experience a different environment compared with the central elements. In addition, it may be observed that the estimated values are in good agreement with the full-wave analysis results. However, a small difference might exist because the relative position of the ridgeline with respect to the EBG mushroom cells is not always the same. Conventionally, the antenna array is designed based on fixed input impedance

that is usually the input impedance of an isolated element at the central frequency. Such a design usually ignores the effect of the feeding network discontinuity as well as the mutual coupling effect on the input impedance of the elements in the array environment.

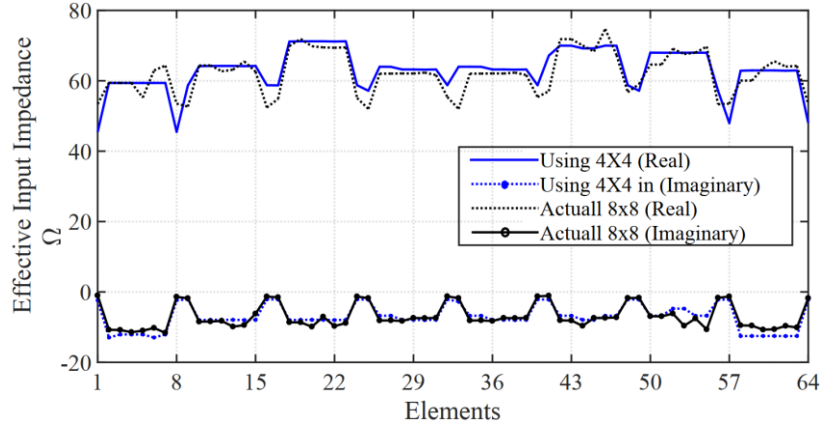


Figure 4.9 Effective impedance of 8×8-element array using the 4×4-element array at 57 GHz.

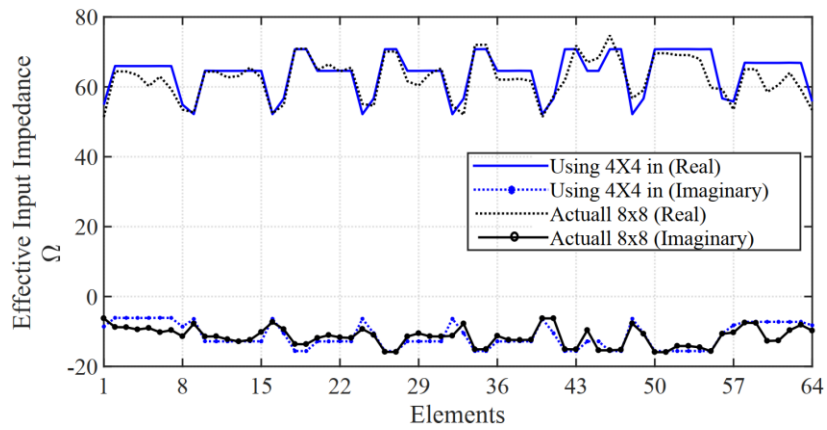


Figure 4.10 Effective impedance of 8×8-element array using the 4×4-element array at 60 GHz.

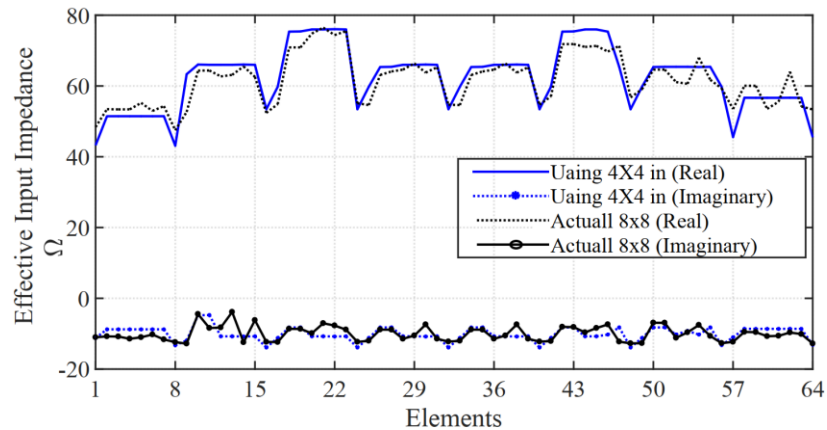


Figure 4.11 Effective impedance of 8x8-element array using the 4x4-element array at 64 GHz.

Here, the feeding network of the 8×8 array is constructed such that each element has its effective impedance, which is represented by a different line width terminated by the effective impedance of the element, where the coupling effect is considered. Then a transformer with different width and length is used to match the actual impedances, which have real and imaginary parts, as shown in Fig. 4.12. The initial design parameters are calculated using [84]. Then, the overall corporate distribution network is optimized to compensate for the discontinuities in the feeding layer.

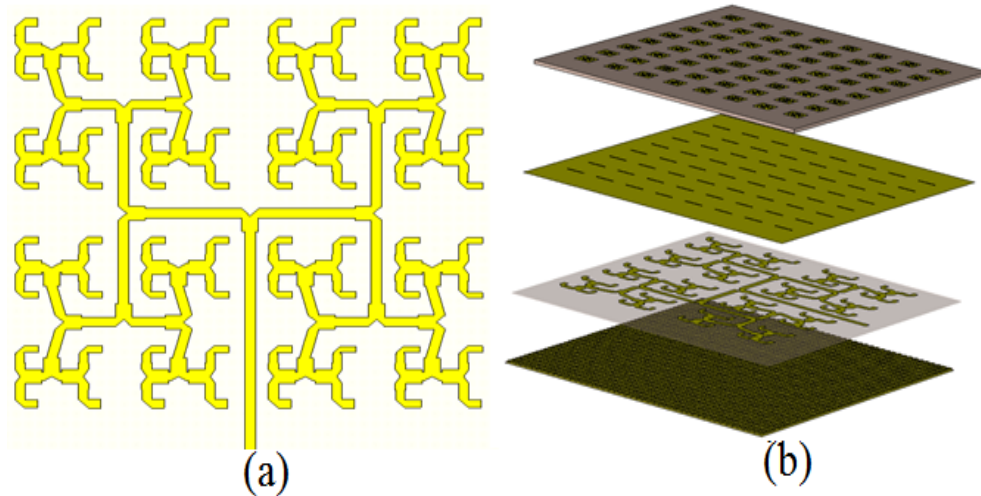


Figure 4.12 (a) Feed network structure of the 8×8 -element array, (b) 8×8 -element array full structure with the ME-dipole elements.

It is worth mentioning that using this procedure reduces the processing time a lot to optimize the reflection coefficient by replacing the radiating elements with their effective impedances at their ports. In Fig. 4.13, the reflection coefficient is shown where four cases are introduced. In the first case, the feeding network is designed at 60 GHz with terminating loads of Z_o . In the second case, the feeding network is optimized when a complex effective input impedance terminates each port at 60 GHz. In the third case, the feeding network of the second case is terminated by the actual radiating antenna elements (ME dipole). In the fourth case, the feeding network is optimized for the whole frequency band when terminated by the frequency dependent Z_{eff} using HFSS. The frequency dependent loads have been optimized using HFSS, where the lumped ports are loaded with snp/znp or ynp files which include the effective input (impedance/admittance or the S parameters) as frequency dependent. The effective impedance termination provides comparable performance to the actual structure, which agrees very well at 60 GHz, at which the feeding network is designed and optimized. One can also notice that there is no much difference between the third case and the fourth case.

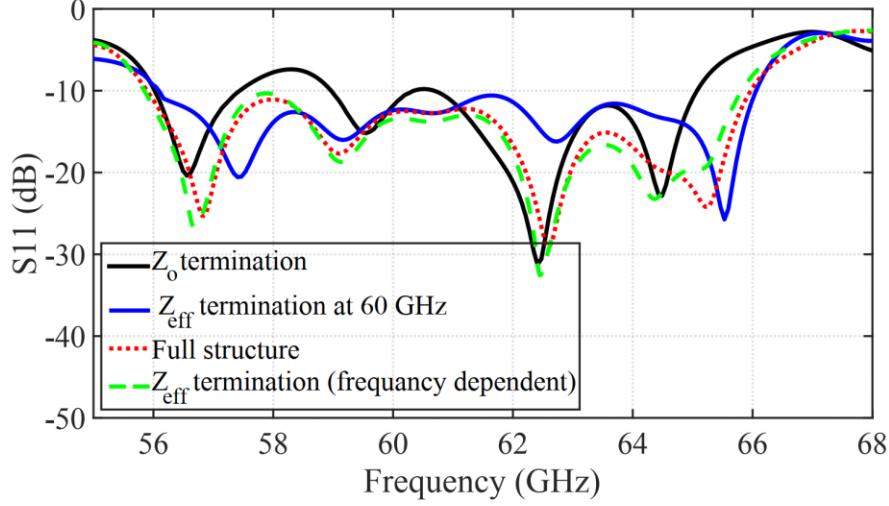


Figure 4.13 Reflection coefficient of 8×8 ME-dipole antenna arrays.

The bandwidth obtained from the conventional method is smaller than that based on the concept of small to large, which leads to achieving a bandwidth closer to the single element bandwidth. In addition, a better matching level using the actual elements to realize the whole structure and obtain the far-field results. As mentioned in [20], the total radiation patterns and gain can be estimated by using the concept of pattern multiplication, considering the effective input impedance in the active voltage terminal of the elements as such

$$\begin{Bmatrix} E_{\theta}^t \\ E_{\phi}^t \end{Bmatrix} = \begin{Bmatrix} E_{\theta} \\ E_{\phi} \end{Bmatrix} F(\theta, \varphi) \quad (4.3)$$

where E_{θ} and E_{ϕ} are the θ and ϕ components of the element radiation patterns, respectively. E_{θ}^t and E_{ϕ}^t are the corresponding total array radiation patterns. $F(\theta, \varphi)$ is the array factor that can be expressed as

$$F(\theta, \varphi) = \sum_{i=1}^N V_{ai} e^{jk_o \rho_i \sin \theta \cos(\varphi - \varphi_i)} \quad (4.4)$$

and

$$V_{ai} = \sum_{j=1}^N A_{ij} V_j \quad (4.5)$$

where (ρ_i, φ_i) is the cylindrical coordinates of the i^{th} element. Then the directivity, D , and the gain, G of the array with respect to an isotropic radiator at a distance r can be expressed as:

$$D(\theta, \varphi) = 4\pi \frac{|E_{\theta}^t(\theta, \varphi)|^2 + |E_{\phi}^t(\theta, \varphi)|^2}{2\eta P_r} \quad (4.6)$$

$$G(\theta, \varphi) = 4\pi \frac{|E_\theta^t(\theta, \varphi)|^2 + |E_\varphi^t(\theta, \varphi)|^2}{2\eta P_t} \quad (4.7)$$

$$P_t = \sum_{i=1}^N \text{real}(Z_i^e) \left| \sum_{j=1}^N Y_{ij} V_{aj} \right|^2 \quad (4.8)$$

$$P_r = \eta_{rad} P_t \quad (4.9)$$

where η is the intrinsic impedance of free space, P_r is the total radiated power, P_t is the total input power that contributes to the radiation from the array and η_{rad} is the total radiation efficiency, which includes the reflection losses of the radiating elements due to mismatch, dielectric and Ohmic losses, surface waves losses, and the losses due to connector and transition. It is important to highlight that η_{rad} is calculated after designing the feeding network. Moreover, the technology of design the feeding network plays a significant role in calculating the total radiation efficiency. Hence, our method can estimate the gain without considering the feeding network losses. However, the realized gain (including the mismatch and feeding network losses) can still be calculated after designing the feeding network using (4.7), (4.8), and (4.9). Since η_{rad} can be obtained from the full-wave simulation, it should be mentioned that for the pattern multiplication, three cases are considered for the ME-dipole element pattern: Case A uses the radiation pattern of the isolated element; Case B, the embedded radiation pattern of an intermediate element of the small 4×4- array; Case C, the embedded radiation pattern of an element in an infinite arrays environment. The normalized radiation patterns are shown in Figs. 4.14, 4.15, and 4.16 at 57, 60, and 64 GHz, respectively. The 8x8-element array normalized radiation patterns considering the above cases are given in Figs. 4.17, 4.18, and 4.19 for E-plane and Figs. 4.20, 4.21, and 4.22 for H-plane. A good agreement between the estimated radiation pattern using the effective impedance method and the full-wave analysis can be observed. Besides, the first sidelobe levels in both E- and H-plane are around -12.8 dB.

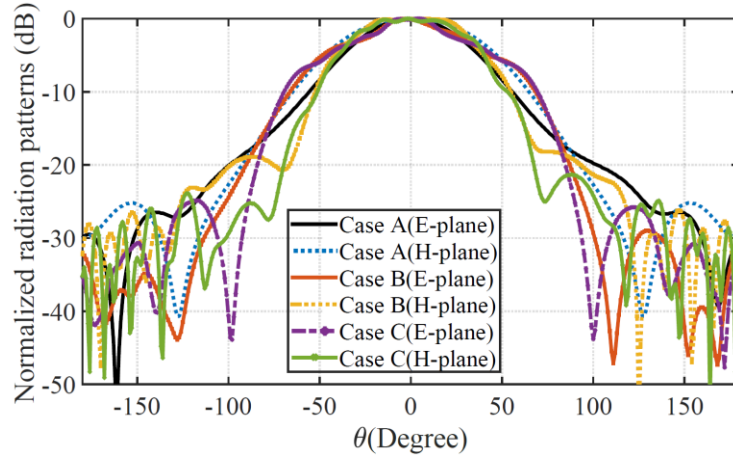


Figure 4.14 Normalized radiation patterns of the ME-dipole antenna at 57 GHz.

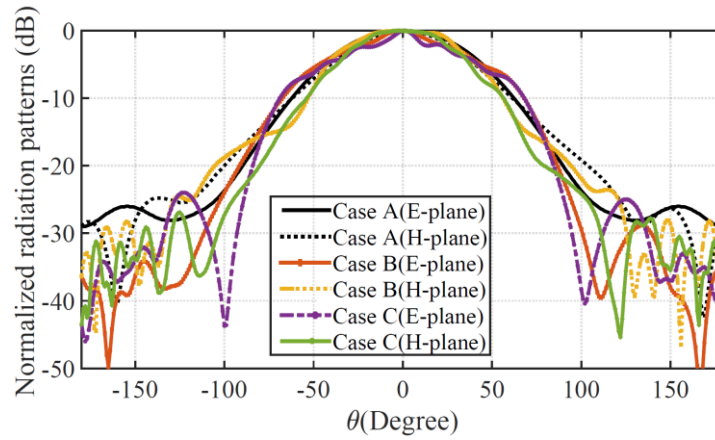


Figure 4.15 Normalized radiation patterns of the ME-dipole antenna at 60 GHz.

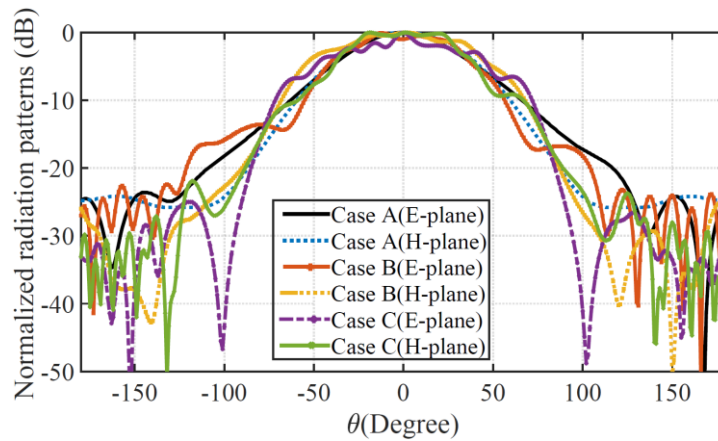


Figure 4.16 Normalized radiation patterns of the ME-dipole antenna at 64 GHz.

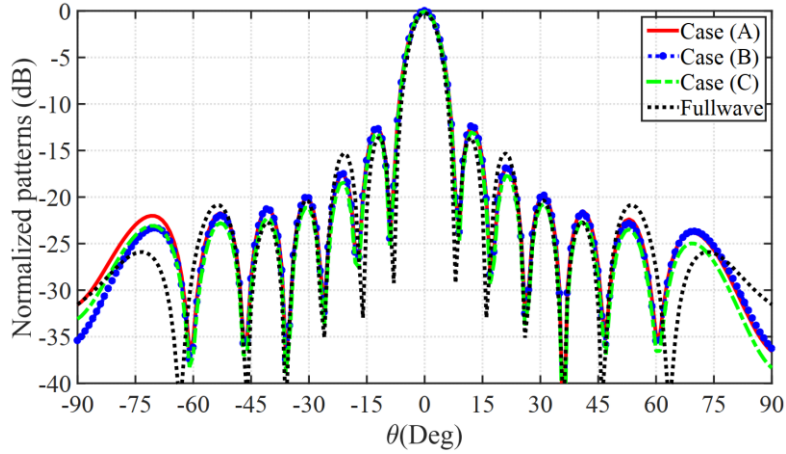


Figure 4.17 Normalized radiation patterns of the 8×8 -element array at 57 GHz (E-plane).

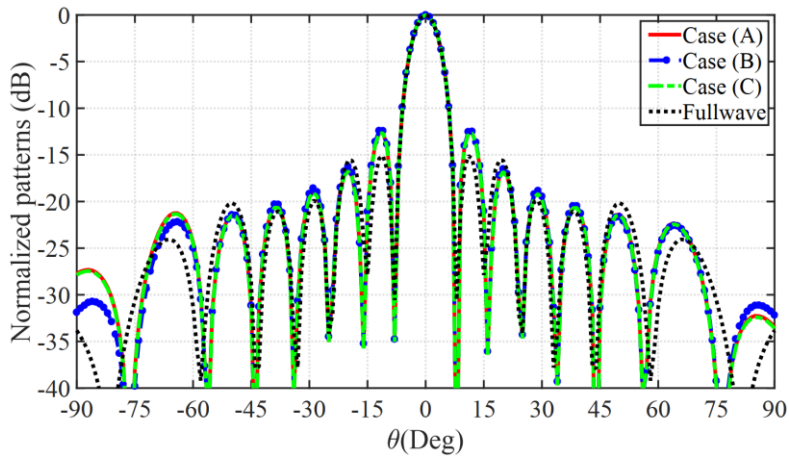


Figure 4.18 Normalized radiation patterns of the 8×8 -element array at 60 GHz (E-plane).

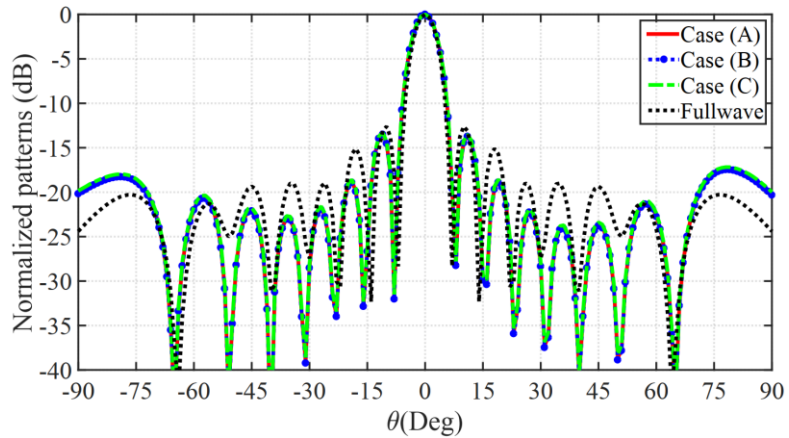


Figure 4.19 Normalized radiation patterns of the 8×8 -element array at 64 GHz (E-plane).

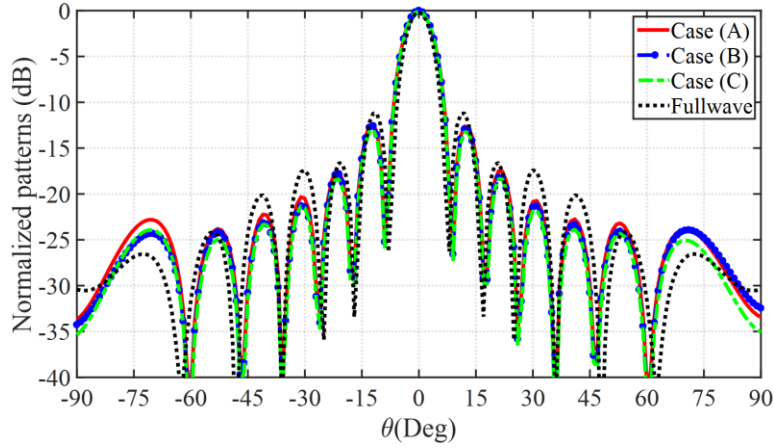


Figure 4.20 Normalized radiation patterns of the 8×8 -element array at 57 GHz (H-plane).

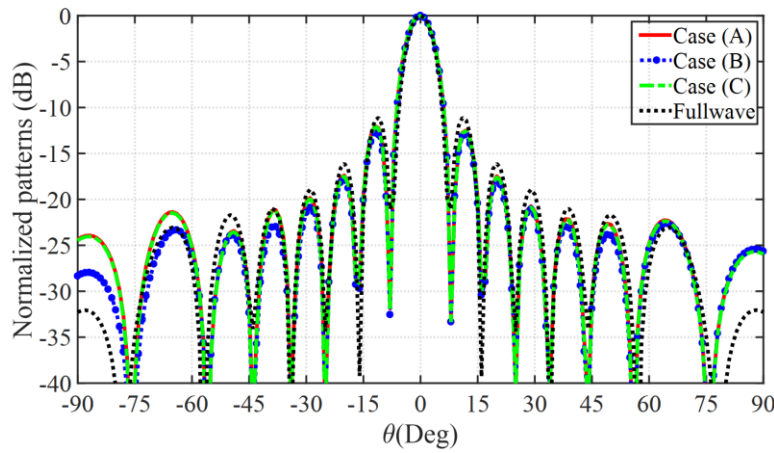


Figure 4.21 Normalized radiation patterns of the 8×8 -element array at 60 GHz (H-plane).

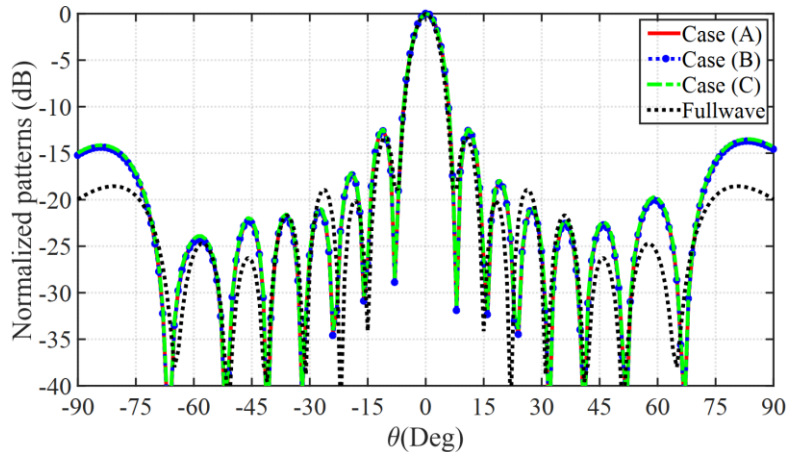


Figure 4.22 Normalized radiation patterns of the 8×8 -element array at 64 GHz (H-plane).

The simulated array gain for Cases A, B, and C, compared to the full-wave analysis using CST (time-domain), are indicated in Table I. It can be seen that all the cases provide close values for the gain.

However, Case C shows better agreement when the element is considered in an infinite array and can be used to estimate the array far field parameters.

Table I. 8×8-Element Array Gain

Frequency (GHz)	Case A	Case B	Case C	Full- Wave
57	25.86	25.80	25.85	25.60
60	26.01	26.08	26.03	25.98
64	26.32	26.29	26.35	26.27

The radiation efficiency over the operating frequency is better than 72%. The total radiation efficiencies and the simulated gain over the operating frequency without including the total losses are illustrated in Fig. 4.23.

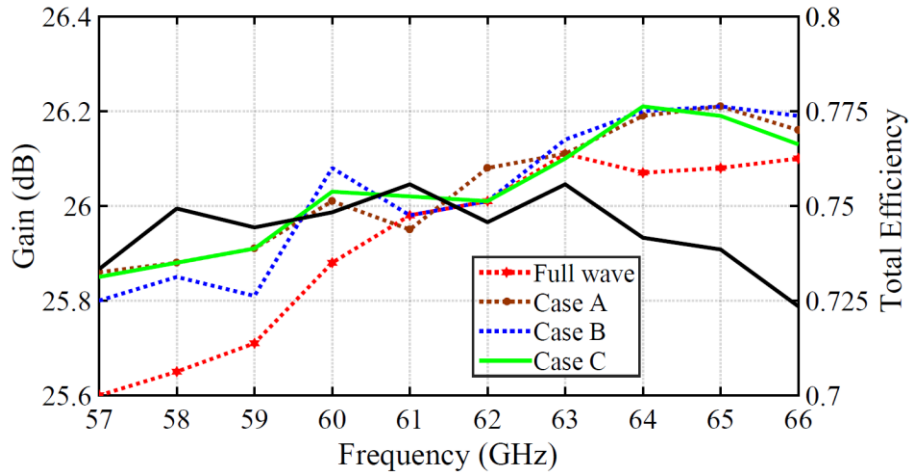


Figure 4.23 Full-wave simulated gain compared to those calculated based on different cases (A, B, and C) and total radiation efficiencies of the 8×8 element array antenna.

4.4.3 16×16 antenna array design

A 16 × 16 antenna array is a substantial numerical structure considering the feeding network within a periodic mushroom structure. Thus, a full-wave solution is not always possible for verification because of the limited computational resources. The 16×16 array characteristics are predicted based on a 4 × 4 array and 8x8 array and comparing the effective input impedances from these two predictions. A good agreement can be observed, and the coupling effect appears clearly on the edge elements, as shown in Fig. 4.24, 4.25, and 4.26 at frequencies 57, 60, and 64 GHz, respectively. For a 16 × 16 feeding network, a

central feed WR-15 is used to excite the radiating elements. Hence, the simulation and computation can be reduced by taking advantage of the symmetry.

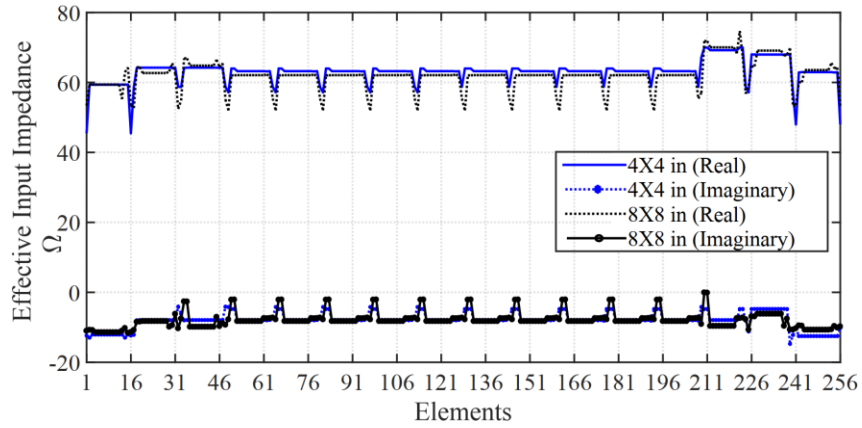


Figure 4.24 Effective impedance of 16x16-element array using the 4x4-element and 8x8-element array at 57 GHz.

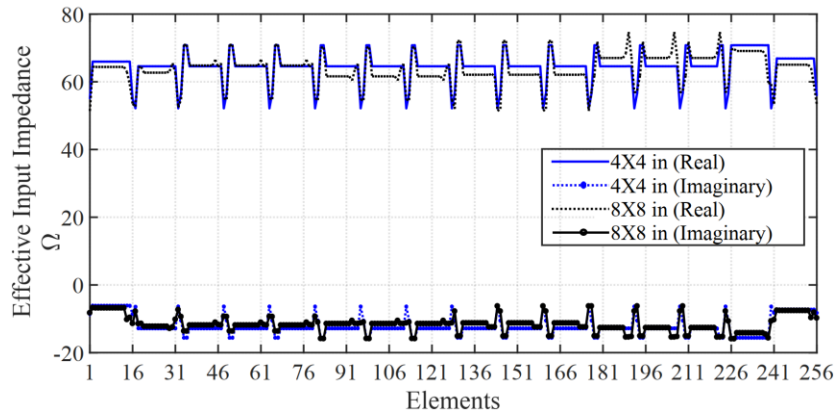


Figure 4.25 Effective impedance of 16x16-element array using the 4x4-element and 8x8-element array at 60 GHz.

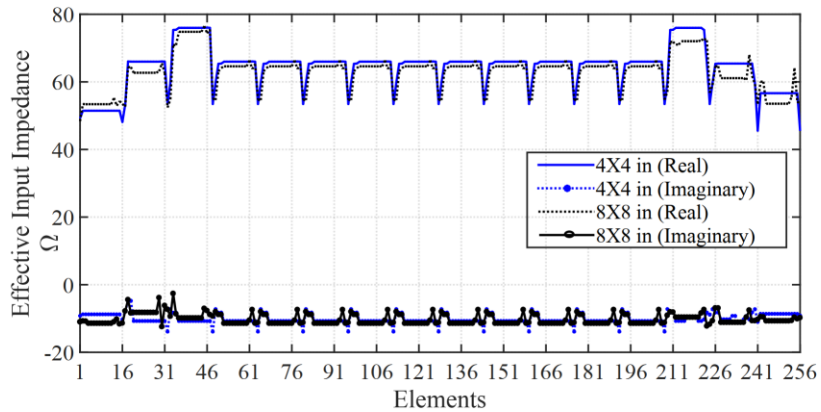


Figure 4.26 Effective impedance of 16x16-element array using the 4x4-element and 8x8-element array at 64 GHz.

4.4.4 Transition from WR-15 to MRGW

A WR-15 on the bottom plane of the structure is used to excite the ME-dipoles. Hence, transferring the power from the TE_{10} dominant mode of the WR-15 to the quasi-TEM MRGW is required. In [85], a transition from printed ridge gap waveguide (PRGW) to WR-15 is designed using a cavity back short, which requires a thick top metal layer. However, in our design, we use MRGW, where the ridge is elevated from the AMC layer with a dielectric material that has permittivity ϵ_{r1} . Therefore, a matching stub line is made in the EBG layer (step). Then another via-hole is made through the substrate ϵ_{r1} to connect MRGW with the matching stub line, as shown in Fig. 4.27. The via-hole positions with the width and length of the stub are optimized to achieve a matched bandwidth of 46–76 GHz. The simulated S-parameters are shown in Fig. 4.28. It should be stated that the two output ports have a 180° phase difference, as indicated by the field lines in Fig. 4.27(a). Hence, the structure of the feeding network must be symmetric along the x-axis.

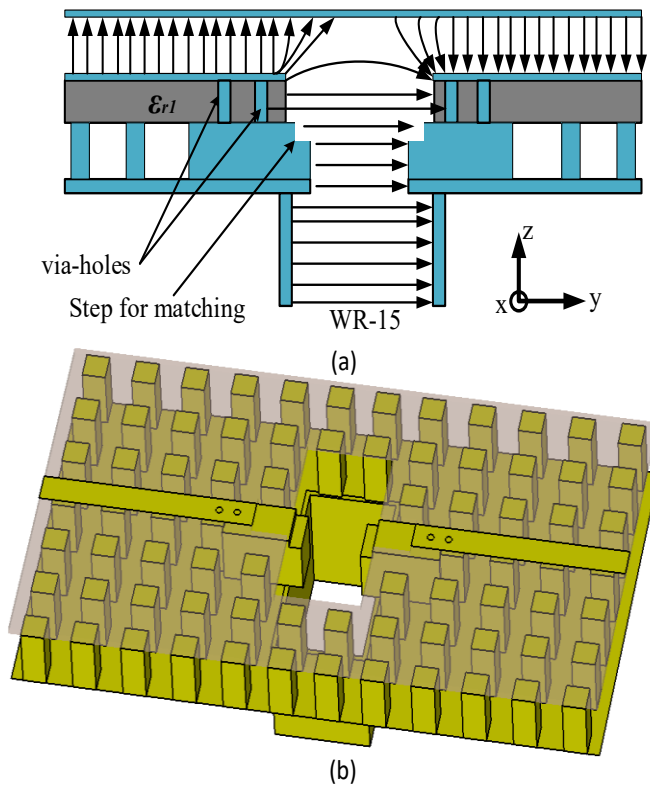


Figure 4.27 MRGW to WR-15 transition: (a) side view, (b) 3D geometry (top metallic layer is hidden).

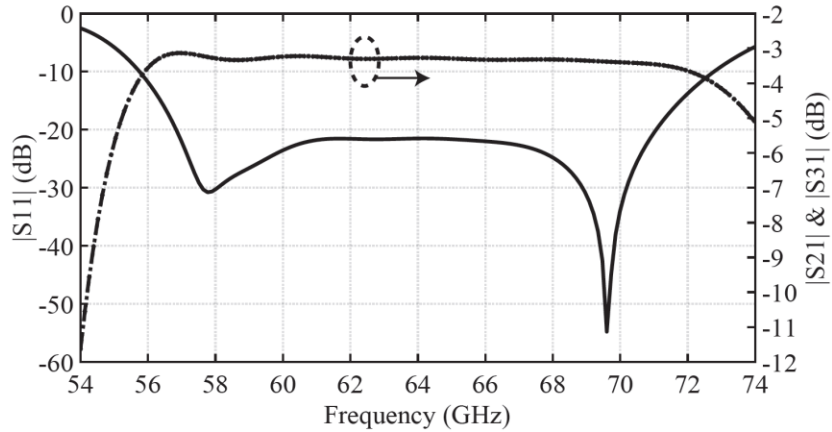


Figure 4.28 Reflection coefficient of the transition from WR-15 to MRGW.

4.4.5 16×16 -element array optimization

The processing time to optimize the feeding network for a 16×16 array is relatively huge compared to an 8×8 array, especially in the presence of the EBG texture. As all the mutual coupling effects are considered, and the effective impedances of all elements are known. Therefore, to reduce the number of optimization parameters, the feeding network is partitioned into small parts; each part feeds a 2×2 subarray. The feeding network of each 2×2 subarray is designed and optimized. Thus, the feeding network is reduced to a feeding network of 8×8 subarrays, each terminated by the input impedance of the corresponding 2×2 subarray. This array is partitioned into a set of subarrays of 4×4 elements. Now, a feeding network of 2×2 subarray each of 4×4 elements should be optimized for the final port. As such, the optimization is always performed on a 2×2 feeding network. At each step, the mutual coupling effect with respect to the relative positions of the subarrays are considered as the presence of all elements of the 16×16 array is included. The 16×16 array is constructed from the 8×8 -subarrays of 2×2 subarrays as a first level. Each of these 2×2 feeding networks is designed to get the effective impedances at the port of each sub-array feeding network through a separate optimization. In the second level, the 8×8 subarray is reduced to 4×4 subarrays feeding network. Each of the 4×4 subarrays is a 2×2 subarray.

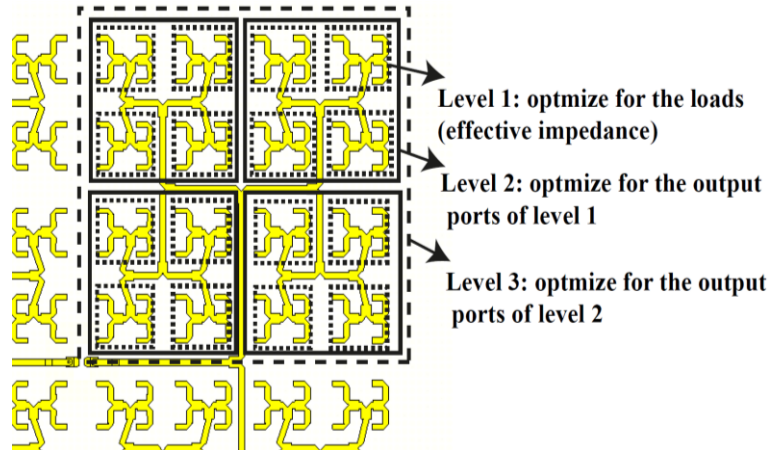


Figure 4.29 Sub-array optimization for 16x16 array.

Perform the design of a 2×2 feeding network that is terminated by the 2×2 subarray effective impedances. Notice that the length of the feeding network arms is double the lengths of the previous level. Finally, level three ends up being a 2×2 array of 8×8 subarrays. Its feeding network arms are twice the length of the previous level. This procedure has broken the problem into several optimizations of a 2×2 feeding network that has a small number of parameters to optimize each time. Symmetry can also be enforced to reduce the number of 2×2 problems. Without symmetry, the number of 2×2 feeding networks is $(8 \times 8 + 4 \times 4 + 2 \times 2 = 84)$. It should also be stated that because the array input port is the rectangular waveguide, the feeding network of the 8×8 subarray is a design of a power divider that its input is coupled to the waveguide aperture. Another difference in this design because of the use of the waveguide input port and its differential output power divider. Therefore, the two sides of the array are out of phase. In order to correct for this, one side is rotated 180° to compensate for the phase that makes the two halves in phase. Fig. 4.29 shows a sketch of just a quarter of the 16×16 feeding network. By using this technique, we are reducing the number of optimization parameters for the feeding network. A quarter of the geometric configuration of the 16×16 array antenna is shown in Fig. 4.30. Different power dividers are deployed to the feeding network to reduce the interaction between the stubs exciting the slots and the nearest line to its end. Fig. 4.31 shows the simulated reflection coefficient of the different power dividers.

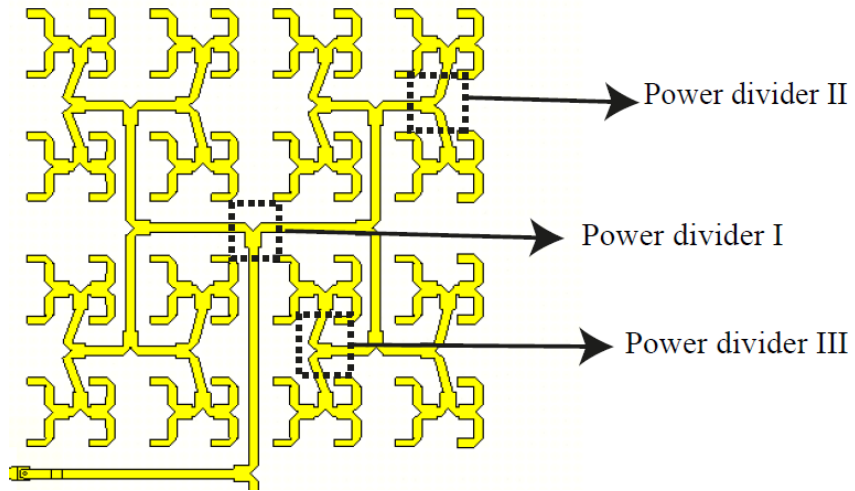


Figure 4.30 Quarter of feeding network of 16×16 array antenna.

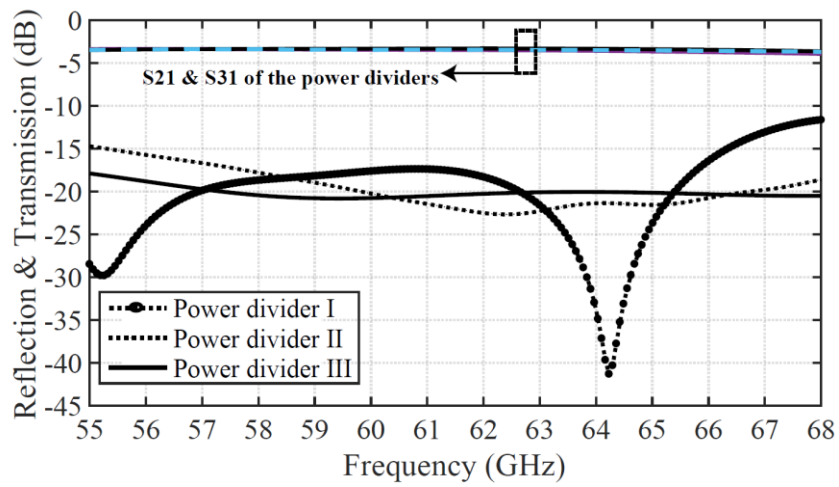


Figure 4.31 Simulated reflection and transmission coefficients of the power divider I, the power divider II and the power divider III.

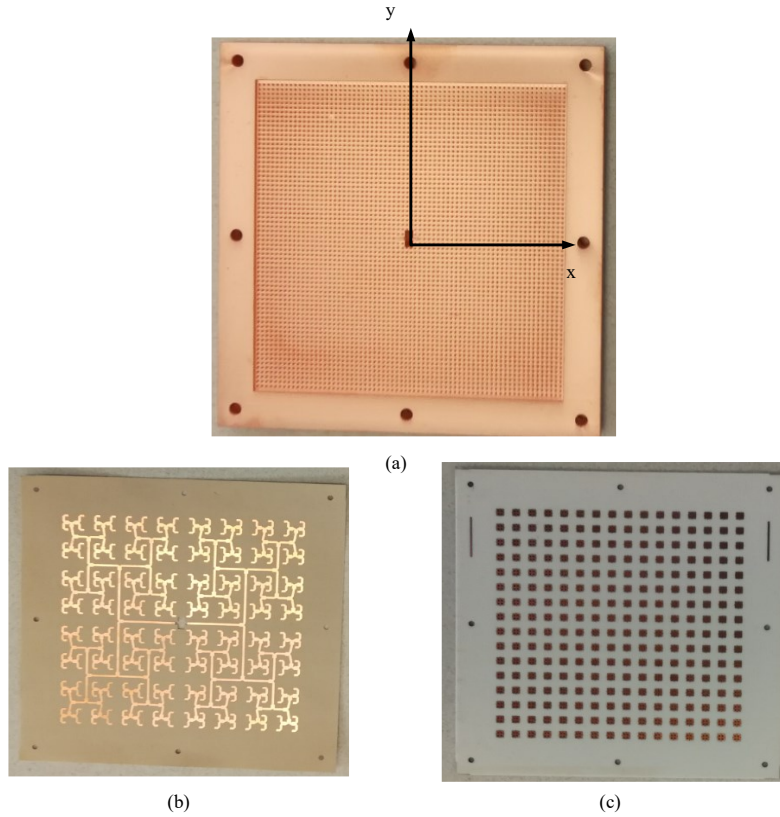


Figure 4.32 Photos of different parts of fabricated antenna: (a) the AMC metal pin layer, (b) the feed network layer, and (c) the radiating layer.

A physical prototype for the 16×16 array antenna is fabricated with a dimension of $89 \text{ mm} \times 89 \text{ mm}$ to validate the performance. The different parts and the complete antenna structure connect to a standard WR-15 flange with screws are presented in Fig. 4.32.

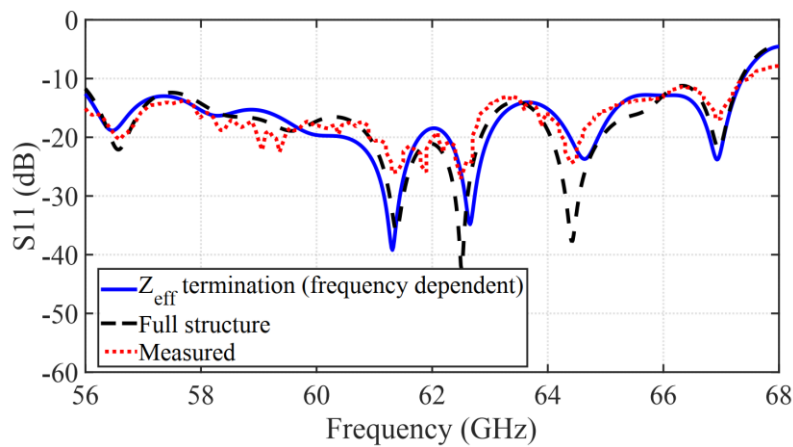


Figure 4.33 Reflection coefficient of 16×16 with ME-dipole antennas (actual loads) and effective impedances loads for optimizing the feed network.

For fabrication, 3-D-printing technology is used for the AMC metal pin layer, where a polycarbonate material is used. Then the printed structure is coated with 0.08 mm thick copper material via the electroplating process. For the feed network and the radiating layers, printed circuit board (PCB) milling technology is used. The response of the optimized structure with loads calculated from the effective input impedance and the ME dipole elements as actual loads are shown in Fig. 4.33, with 19% of reflection coefficient bandwidth ($|S_{11}| < -10$ dB) covering the 56–67GHz frequency range. The tolerances of manufacturing and assembling the structure layer cause some differences between the measurement and the simulation results. The normalized radiation patterns for the 16x16 array are shown at 57 GHz, 60 GHz, and 64 GHz, respectively, in both the E- and H-planes in Fig. 4.34-4.39. The array gain is computed using the method [20] for Case A, B, and C, compared to the full-wave analysis using CST (time domain), as indicated in Table II.

Table II. 16×16-Element Array Gain

Frequency (GHz)	Case A	Case B	Case C	Full-Wave
57	31.45	31.47	31.44	31.41
60	31.41	31.42	31.41	31.38
64	31.46	31.48	31.48	31.46

The estimated radiation patterns are in good agreement with the full-wave analysis. The first sidelobe levels (SLL) in both E- and H-plane are around -12 dB with symmetrical radiation patterns. Also, the total radiation efficiency over the operating frequency is more than 70%. The total radiation efficiencies and the gain over the operating frequency are illustrated in Fig. 4.40. A difference of 1 dB can be observed between measured and simulated; this is mainly because of the dielectric losses and fabrication tolerance. The fabrication tolerance can be critical and degrades the performance of the antenna system, especially at mm-frequency ranges. It is worth recalling that the total efficiency depends on the electromagnetic wave guidance technology (Ridge Gab, SIW, or microstrip). However, the proposed concept can be applied regardless of the used technology.

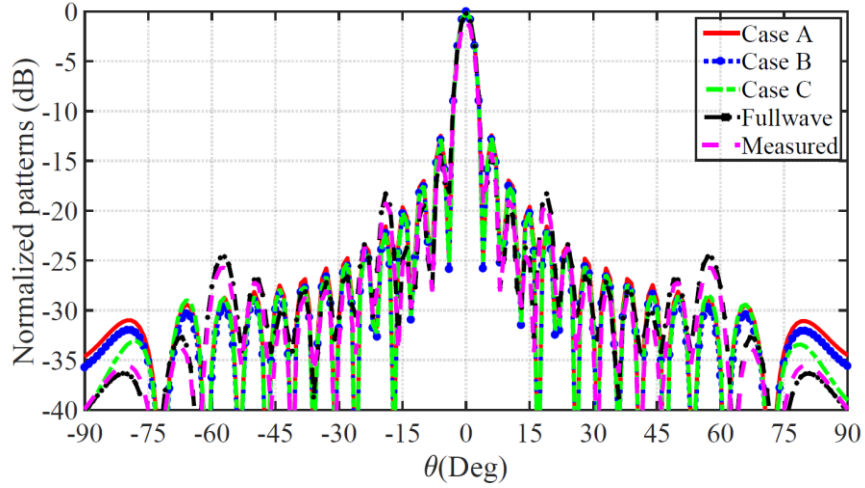


Figure 4.34 Normalized radiation patterns of the 16×16-element array at 57 GHz (E-plane).

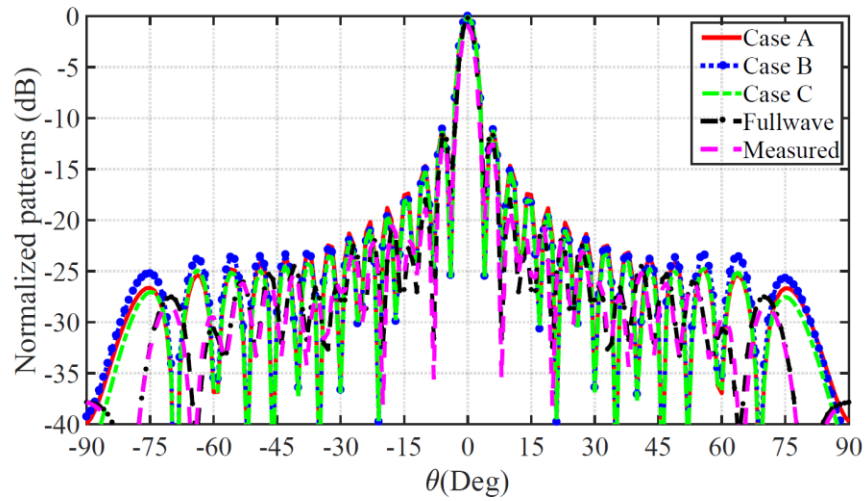


Figure 4.35 Normalized radiation patterns of the 16×16-element array at 60 GHz (E-plane).

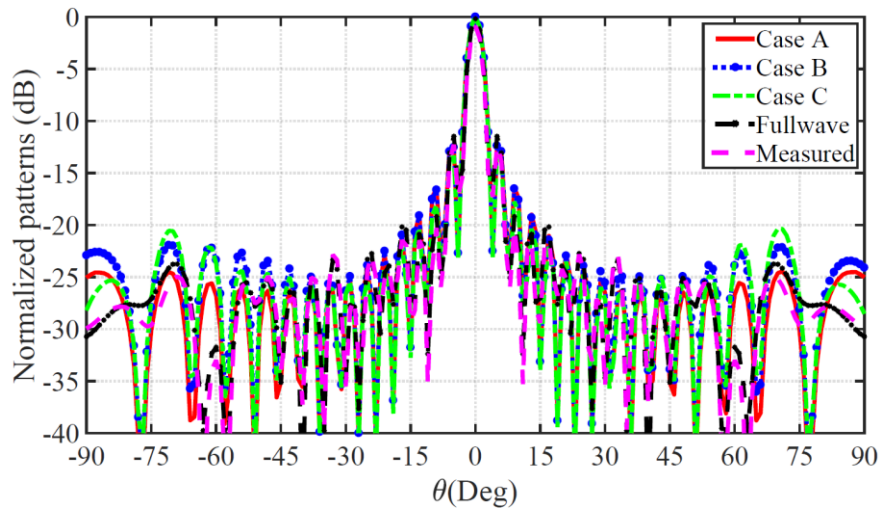


Figure 4.36 Normalized radiation patterns of the 16×16-element array at 64 GHz (E-plane).

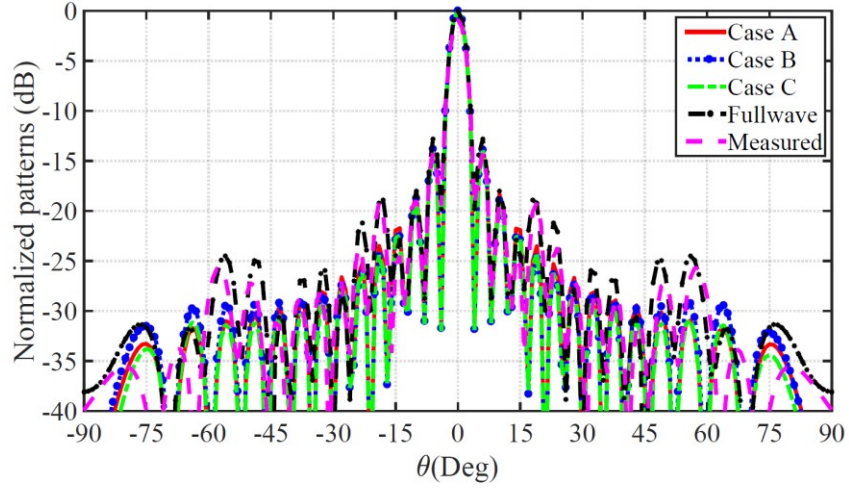


Figure 4.37 Normalized radiation patterns of the 16×16 -element array at 57 GHz (H-plane).

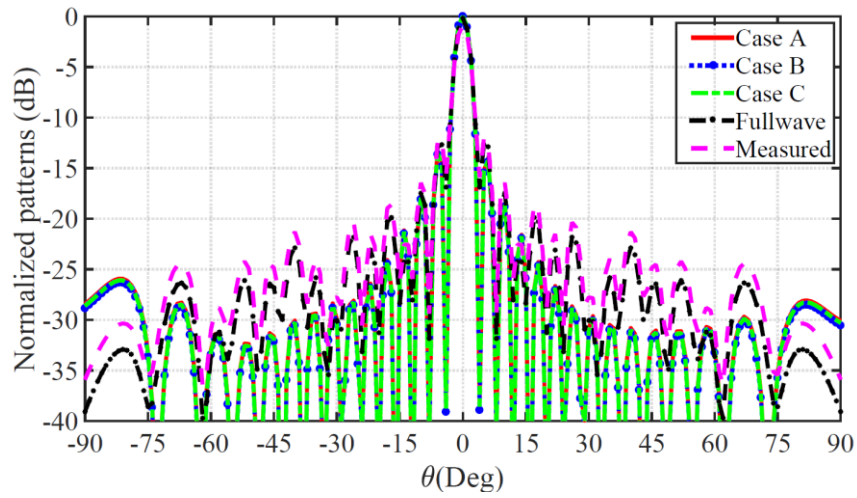


Figure 4.38 Normalized radiation patterns of the 16×16 -element array at 60 GHz (H-plane).

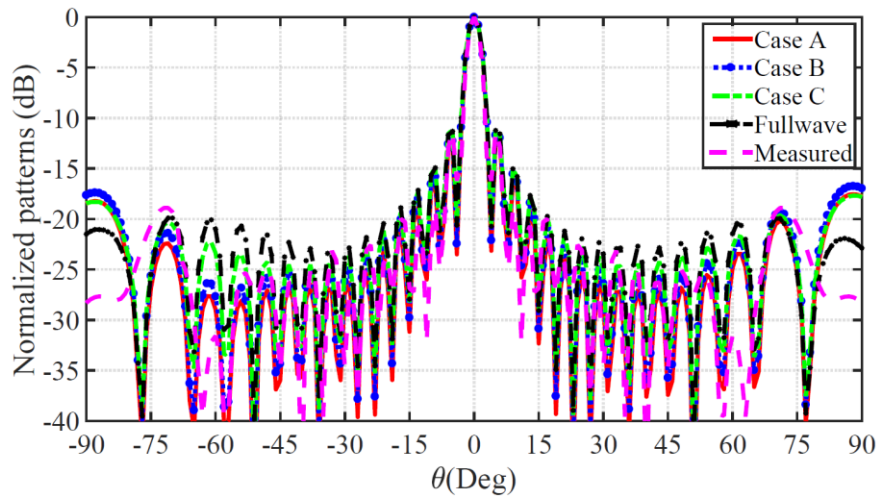


Figure 4.39 Normalized radiation patterns of the 16×16 -element array at 64 GHz (H-plane).

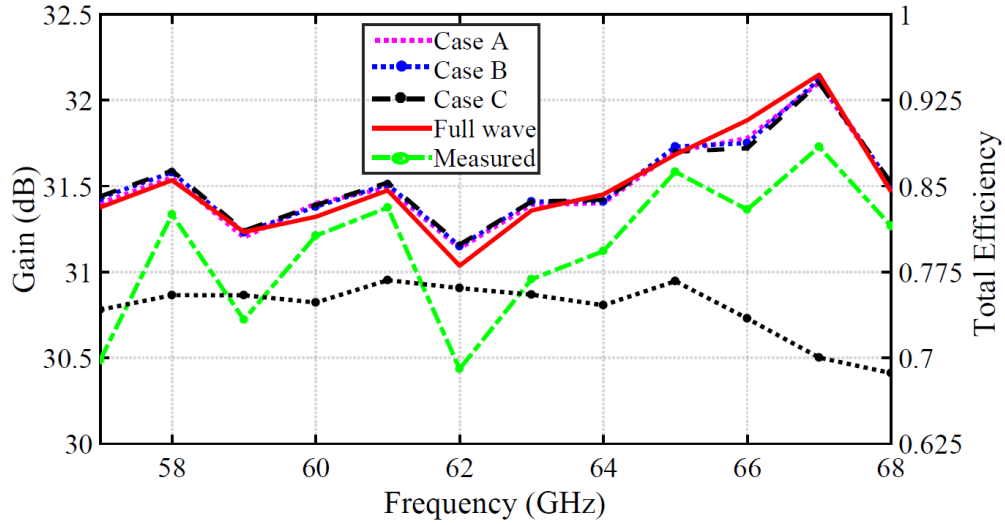


Figure 4.40 Full-wave simulated gain compared to different Cases (A, B, and C) and total radiation efficiencies of the 16×16 element array antenna.

Table III. Comparison Between Proposed and Reported 60-GHz Antenna Arrays

	Present	[86]	[87]	[79]	[88]	[89]	[90]
Size (mm ²)	7.4 × 7.4	24×24	7.5×7.6	6.08×6.8	1.6×1.7	3.36×3.36	7×6.4
# of elements	16×16	64×64	16×16	16×16	4×4	8×8	16×16
# of layers	2	3	3	3	4	2	3
BW%	19	28.1	13	15.3	22	17	16
Gain, dBi	31.7	39.2	33	30.1	18	27	33.2
Efficiency	>71	>15	>80	>49	>35	>70	>70
Technology	MRWG	MS line	WG	SIW	SIW	RGW	RGW

Compared with other 60-GHz antenna arrays in the literature, the present 16 × 16 array has wideband and excellent radiation performance in terms of efficiency and gain, as shown in Table III. It is expected that SIW technologies experience more losses due to dielectric material compared to the gap waveguide (RGW) technology. In addition, RGW technology provides even better radiation efficiency, compared to MRGW, because of the absence of any dielectric material. However, its design for complex feeding networks is very laborious and might require complete full-wave design and optimization for the pin’s locations. It should be stated that using MRGW allows feeding all elements directly, which would benefit in controlling the amplitude and phase to each element of the array. Unlike previous designs that make

the feeding network in two levels. Each 2×2 subarray is fed through a cavity that does not allow controlling the amplitude and phase for each element individually as each cavity is fed through a corporate feeding network on a lower level at which amplitude and phase can be controlled. Therefore, the actual array element is the 2×2 subarray. The distance between them is larger than one wavelength at all frequencies. Therefore, grating lobes are created, and the scanning capabilities of the array is limited.

4.5 Mutual Coupling and Failure Analysis in Antenna Arrays

Phased array antennas are becoming essential for different applications such as automotive driver assist systems, satellite communications, advanced radar, aerospace, and defense radar systems. Developing communication systems using phased array antennas can bring some complexity and cost issues. In other words, designers use expensive design software to address the complexity of designing an antenna array system, and the physical design performance can be verified before prototyping. For the array, multiple numbers of antennas are used to obtain the required radiation characteristics, such as gain and sidelobe level (SLL). Unfortunately, some of the antenna elements may fail and become inactive due to open/short circuits reasons. Failure can also be due to feeding network manufacturing flaws, which can be challenging, especially for the next generation of the communication systems where the design requirements move toward highly integrated phased-array systems, which adds more challenges and complexity for the hardware developers. Moreover, other factors, such as system aging and excess temperature, can contribute to such failures. The effects of such failures resulting in degradation of the radiation characteristics such as SLL and losses of some transmit power [91]. Recently, in [92-94], different methods have been developed to compensate for the failure effect on the radiation patterns of arrays (more specifically gain and SLL) in the presence of failed or partially failed elements. Obviously, amplitude optimization is affected by mutual coupling. However, these techniques do not include the effect of mutual coupling to tackle the failure effect. According to [66], the mutual coupling between antenna elements has a direct effect on antenna parameters such as terminal impedances. Hence, the antenna array performance is affected. Here, a model to analyze and design the failure of the phased arrays, including the mutual coupling effects between the elements, is presented since the antenna array performance is mainly driven by the element's characteristics. In addition, this model provides full system performance as predicting the failure effect on the gain and SLL. From equation (4.4) and (4.5), conventionally, if this matrix is developed without considering the mutual coupling assuming ideal elements in the array environment, it results in inaccurate modeling. Here, instead of calculating the array

factor from the applied voltage V_j across the input terminals of the element, we used the effective voltage that includes the mutual coupling effect [66]. Then, the total pattern of the array with identical elements in (4.3) can be express in a matrix form as:

$$[E] = [W][a] \tag{4.10}$$

Where $[E]$ is the total field, $[W]$ is the coefficient matrix, which includes the coupling between the elements, and $[a]$ is the excitation amplitude of each element $[V_1, V_2, \dots, V_j, \dots, V_{N \times N}]^t$.

4.5.1 Mutual Coupling and Radiation Characteristic

The phased array radiation characteristics are significantly affected by the array element positions. For instance, the sub-arrays radiation characteristics in the edge of the large antenna arrays can be different from the one in the middle. Fig. 4.41 shows the radiation pattern for the 4×4 subarray in the middle and the corner (embedded) of an 8×8 antenna array using the enhanced modeling that includes the mutual coupling in [66] and compares with an isolated 4×4 antenna array. It is important to highlight that; this modeling can be useful for MIMO antenna systems analysis, especially for the massive MIMO using the concept of subarrays where mutual coupling must be considered. The gain obtained from a subarray at the corner, and the middle (embedded) is 21.49dBi and 21.67dBi, respectively. However, the gain for the isolated 4×4 is 20.8dBi with 9.1dBi gain of the single element.

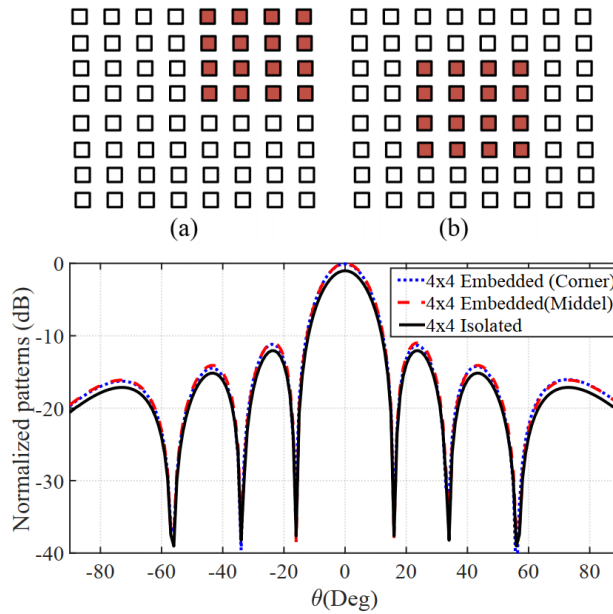


Figure 4.41 Radiation pattern of a 4×4 antenna array in different environments, (a) subarray at the corner (embedded), (b) subarray in the middle (embedded).

4.5.2 Failure of radiation elements and radiation characteristics

The matrix $[a]$ in (4.10) is useful to model the failure in the array. It could be used to represent the failure in the elements by changing the values of V_j according to failure. It should be stated that the matrix $[W]$ is fixed and behave as a transfer function that produces a specific response $[E]$ according to $[a]$. Fig.4.42 shows the radiation patterns for an 8×8 array with a different number of failed elements. It's expected that the gain and SLL change due to the failed elements. For 3, 5, and 8 failed elements (selected randomly), the gain dropped up to 5.5 dB; however, when half of the elements failed, the gain dropped in value by less than 3 dB because of the mutual coupling.

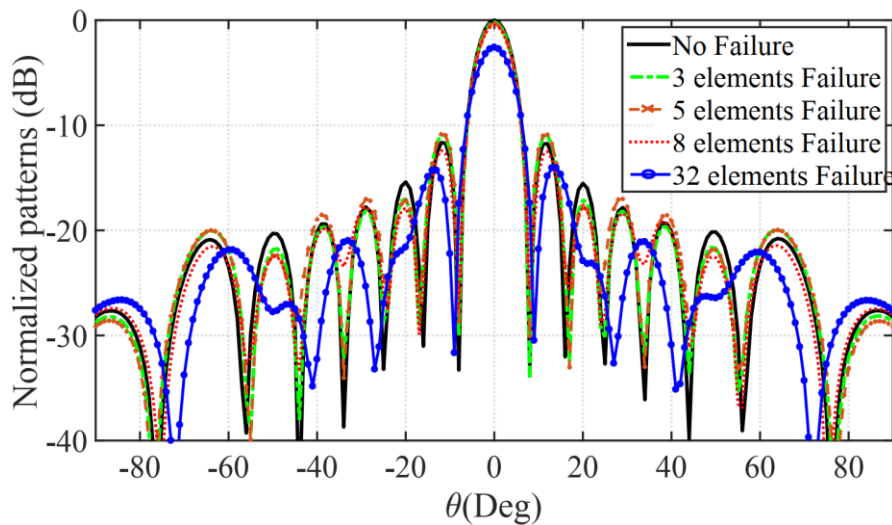


Figure 4.42 Radiation pattern of an 8×8 antenna array with a different number of failure element

Chapter 5: CIRCULARLY POLARIZED ANTENNA ARRAY

5.1 Introduction

For the next wireless communication, it is expected that mm-wave communication portable devices will be used for the Internet of Things (IoT) and high-speed applications [95]. Therefore, considerable research efforts have been conducted on the mm-wave communication [96, 97], such as base station within small cells will cover around a couple of hundred meters. Hence, a high directive of a narrower beamwidth antenna array will be used to reduce the multipath effect. The multipath propagation effect can be reduced significantly when a circular polarization is used [98]. As a result, a high gain antenna array at 60 GHz with circular polarization is a proper candidate to enhance channel communication performance. However, at mm-wave frequencies, the required dimensions are relatively small, and consequently, the fabrication complexity increases that affect its performance. In terms of performance, high efficiency, and low losses, antenna array structures are required to compensate for the free space path loss. The corporate feeding network is usually the primary source of losses at mm-wave frequencies. Therefore, the feeding network must be implemented using the proper electromagnetic guiding technology. MRGW offers more design flexibility in the design of a complicated feeding network by avoiding disturbing the periodic structure of the AMC layer, as previously stated. At 60 GHz, several circularly polarized (CP) antenna array designs have been reported. In [99], [100], a simple planar antenna array is introduced using patch antenna as radiating elements; besides the low efficiency, the 3-dB axial ratio (AR) is less than 10%. In [101], a circular-polarized array antenna by using hexagonal radiating apertures is proposed using metal waveguides feeding network; although high gain and efficiency are achieved, a narrow 3-dB AR is obtained beside the fabrication process for such structures. SIW and microstrip lines are used to design a 2×2 CP antenna in [102], [103]. However, both structures have low gain and efficiency. In [80], an 8×8 CP antenna array based on SIW is introduced with high gain and wide 3-dB AR. However, the substrate losses degrade its efficiency. In addition, manufacturing cost and simulating complexity increase by using a cavity layer to excite the radiating elements as subarrays of 2×2 elements. The cavity layer is mainly used because it is not possible to excite each element individually due to the SIW width [79], [104-109]; therefore, the feed network cannot be designed in a single layer, as stated before. As a result, these configurations have three layers, backed cavities radiation layer besides the feeding network layer. Unfortunately, this kind of structure can increase the full-wave analysis processing time dramatically. Using the concept of the effective input impedance, an 8×8 high gain circular polarized single-layered

corporate feeding network using MRGW is designed using the magneto-electric (ME) dipole as the radiation elements without a need for a cavity layer with wide 3-dB AR and matching bandwidth and excellent radiation performance.

5.2 Design Procedures

Design wideband circularly polarized (CP) antenna array with good radiation performance requires a radiating element with a wide impedance matching and 3-dB axial ratio (AR) bandwidths. It should be stated that the CP-bandwidth is the common (overlapped) bandwidth between the matching and AR bandwidths. Several radiating elements were introduced to provide circular polarization. These designs provided a tradeoff between the matching impedance and AR bandwidths. For instance, a patch antenna with a cavity was used to generate a circularly polarized antenna; however, it provided narrow matching impedance and AR bandwidths [101, 102]. In addition, a U-shaped slot antenna was used with wide matching impedance bandwidth but narrow AR bandwidths [99]. An ME-dipole with wide matching bandwidth and circular polarization is used. The printed form of the ME-dipole consists of patches (electric dipole) on a substrate material; these patches are separated by slots (magnetic dipole).

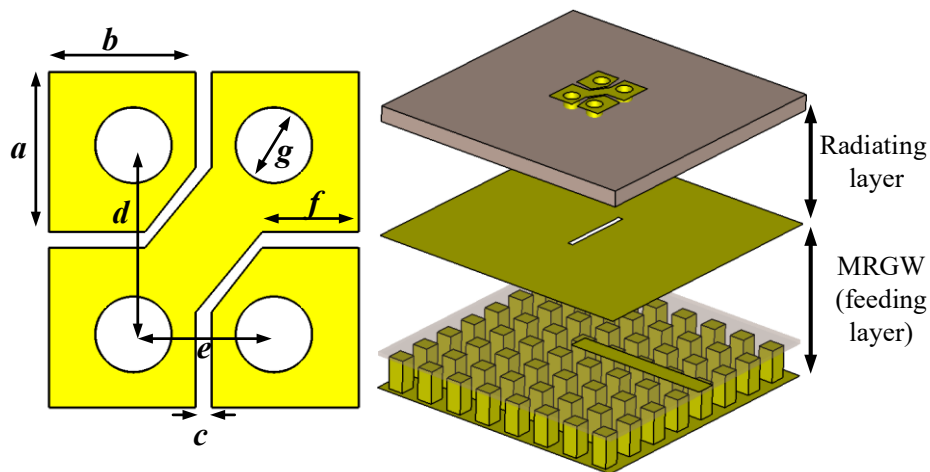


Figure 5.1 Schematic of the EM-dipole with the MRGW ($a = 0.976$ mm, $b = 0.896$ mm, $c = 0.096$ mm, $d = 1.137$ mm, $e = 0.85$ mm, $f = 0.565$ mm and $g = 0.44$ mm).

Circular polarization can be obtained by adding a metallic strip diagonally and trimming the corner of these patches besides perturbing the geometry dimensions such that the slot can excite two orthogonal liner modes with a 90° phase difference. A CP ME-dipole was used in [80], where a wide CP bandwidth was achieved. Using a wideband CP antenna eliminates the need for sequential feeding networks and

avoids the limitation of the delay lines needed for sequential feeding. However, designing a parallel feeding network can be challenging. A ME-dipole element is designed using MRGW, as shown in Fig 5.1. The AMC pin layer has the same dimensions as in Fig. 4.5. The printed ME-dipole is designed using RO4003c substrate with a relative dielectric constant of 3.38 and a thickness of 0.508 mm. In terms of performance, CP-ME-dipole has a 28.8% for $|S_{11}| < -10$ dB (52.4-70 GHz), as shown in Fig 5.2. The 3-dB AR bandwidth is 25.9% (52.4-68 GHz), with a peak gain of 8.8 dBic gain, as elaborated in Fig 5.2. The radiation patterns for the two orthogonal planes are shown in Fig 5.3 and 5.4, where symmetrical and stable patterns can be observed.

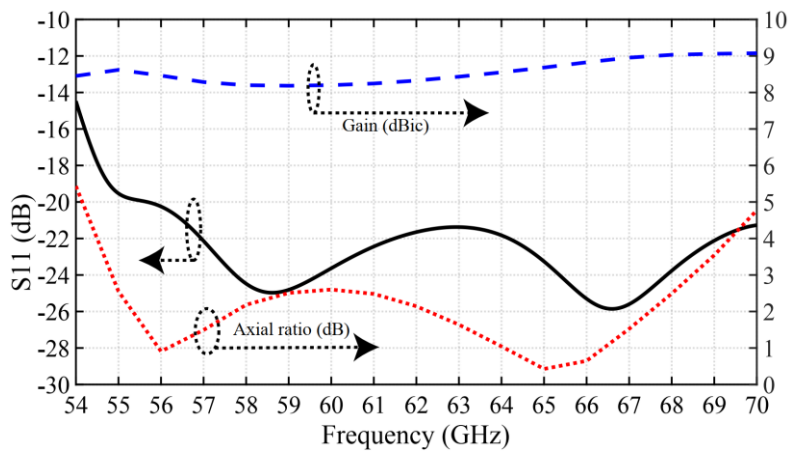


Figure 5.2 Simulated S-parameters gain and AR of the circular polarization ME- dipole antenna.

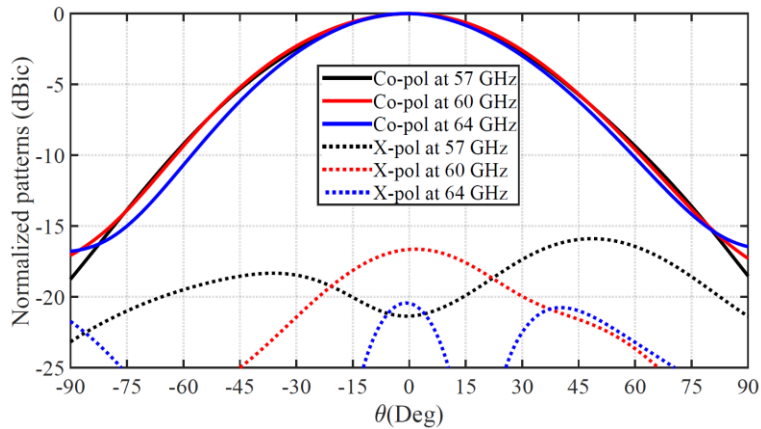


Figure 5.3 Radiation patterns of the ME-dipole antenna (xz-plane).

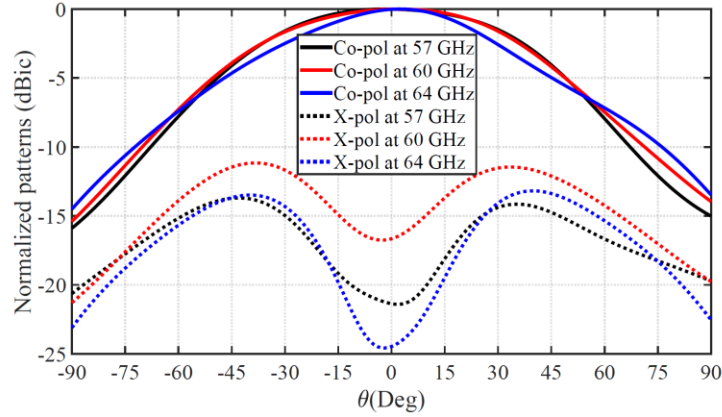


Figure 5.4 Radiation patterns of the ME-dipole antenna (yz-plane).

5.2.1 8x8 antenna array design

The structure of the 8x8 CP-ME dipole antenna array is shown in Fig 5.5, which consists of two layers: the radiating elements layer and the feed network layer, which is designed using MRGW that includes the AMC pins. To highlight the effect of the feeding network on the CP, two different designs are carried out, when the elements are fed all in phase and when differential feeding is used.

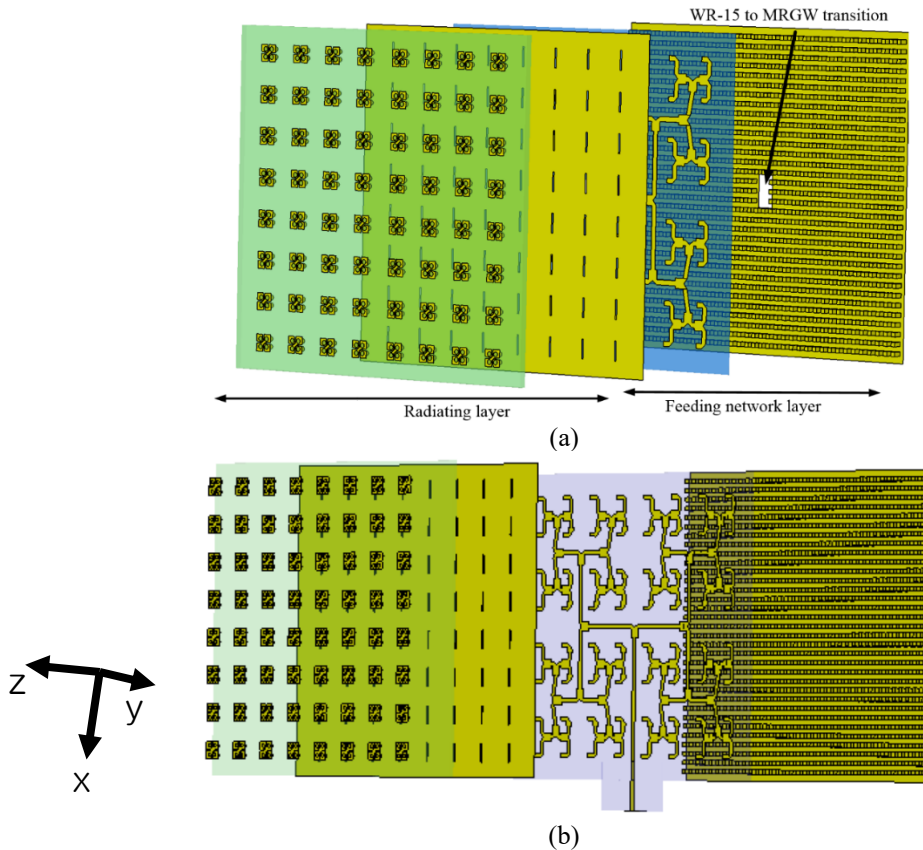


Figure 5.5 Geometry of the 8×8 antenna array with the feeding network of MRGW:(a) differential, (b)all in phase.

Using MRGW allows the whole corporate feeding network to be designed in a single layer. The electromagnetic signal is coupled between these two layers through slots that are etched on the top metal layer of the MRGW. The feeding network is designed using the concept of effective input impedance, as discussed in the previous Chapter. Using 4x4 antenna array elements, the effective input impedances for the 8x8 array are calculated to be used as terminated loads instead of the physical antenna element in order to reduce the full-wave analysis complexity for the feed network design, as shown in Fig 5.6 that shows the 8x8 array elements. Then the calculated effective input impedances for the frequencies 57, 60, and 64 GHz, respectively, are shown in Fig 5.7 and 5.8. Edge and outer side elements are behaving differently from the elements in the middle in terms of the input impedance. Furthermore, the interaction of the element affects the phases and amplitudes at the element ports affecting the AR behavior. It's worth stating that the AR of the elements in the small array needs to be optimized before constructing the large array such that the radiating elements are optimized to provide not only an adequate impedance bandwidth but also wide AR bandwidth.



Figure 5.6 Arrangement of the 8x8 array to calculate the effective input impedances.

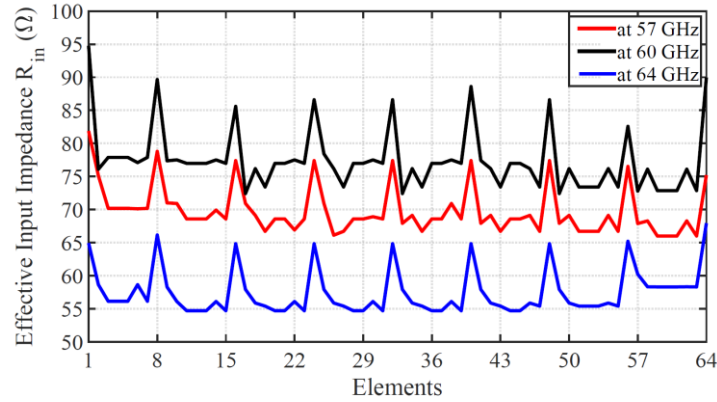


Figure 5.7 Effective impedance of 8×8-element array using 4×4-element array at 57 GHz.

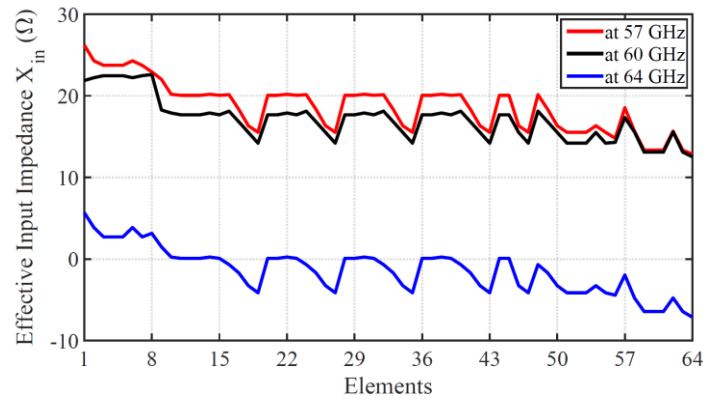


Figure 5.8 Effective impedance of 8×8-element array using 4×4-element array at 60 GHz.

The main reason for affecting the AR in the array environment is the mutual coupling effect between the elements. By optimizing the effective impedance for the elements that include the mutual coupling effect and designing the power divider to reduce the interaction between the slot that excites the ME elements and the MRGW line, as shown in Fig 5.5. Accordingly, three power dividers are used, as shown in Fig 5.9 with simulated reflection coefficient and transmission performance in Fig 5.10, since the feeding network is optimized based on different effective input impedances; therefore, these power dividers are different from those in Fig .4.31.

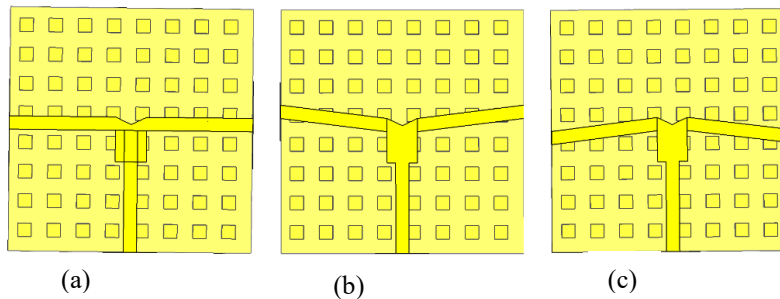


Figure 5.9 Power diver structures: (a) power Divider I, (b) power Divider II and (c) power Divider III.

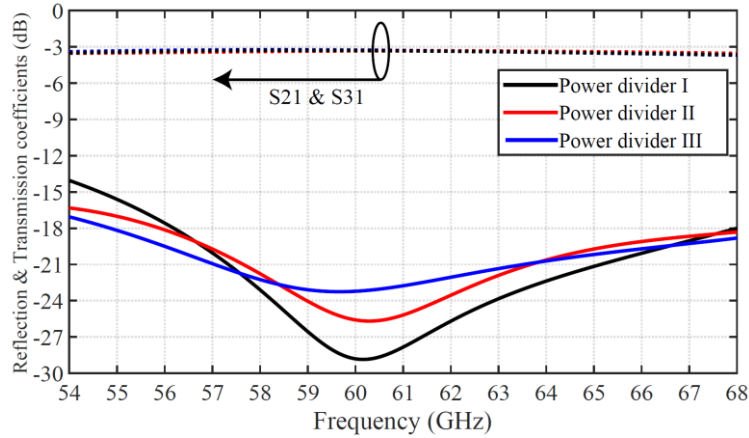


Figure 5.10 Simulated reflection and transmission coefficients of the power.

Eventually, using the CP-ME dipole, an 8×8 antenna array is designed. This 8×8 antenna array is designed such that the antenna elements are accommodated with a space distance less than λ (0.9λ). The dimensions of the radiating element after the tuning in the array environment are shown in Fig 5.11. The dimensions of the ME are changed for the tuning of the 4×4 small array that is used to estimate the effective input impedances only without changing them in the 8×8 array.

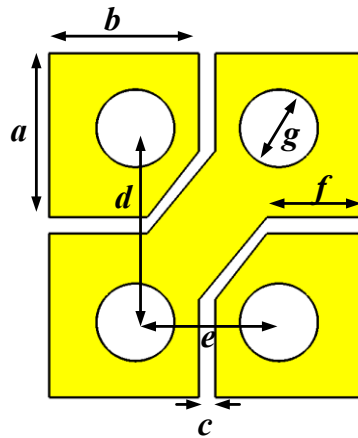


Figure 5.11 Schematic of the EM-dipole with the MRGW ($a = 1.02$ mm, $b = 0.807$ mm, $c = 0.117$ mm, $d = 1.288$ mm, $e = 0.699$ mm, $f = 0.58$ mm and $g = 0.44$ mm).

The simulated S_{11} of the 8×8 CP ME-dipole antenna array is presented for three cases where CST is used with differential feeding (Case I), HFSS with differential feeding (Case II), and all in phase feeding (Case III). In Fig. 5.12 for the differential feeding indicating that the -10 dB bandwidth is 18.2% (from 56.1 to 67 GHz) and 18.8% (from 55.7 to 67 GHz) using HFSS and CST, respectively. The simulated AR with less than 3dB is covering the -10 dB bandwidth. On the other hand, For the all-in phase feeding indicating

that -10 dB bandwidth is 15.8% (from 56.7 to 66.2 GHz), with the simulated AR about covering its -10 dB bandwidth.

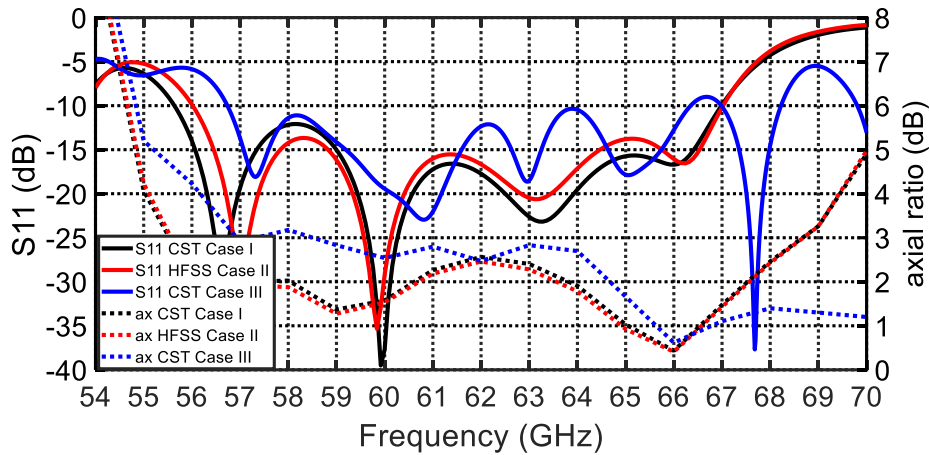


Figure 5.12 Reflection coefficient and AR of the 8x8 antenna array.

Besides, over the frequency band, the gain performance of the antenna array and the radiation efficiencies are shown in Fig. 5.13 with maximum gain up to 26.4 dBic is achieved for the differential feeding based and up to 26 dBic for the other feeding network where all the elements have the same phase excitation. Moreover, the radiation efficiency of the proposed antenna array is better than 82% over the operating frequency band for the differential feeding based. These results highlight the benefits of the differential feeding by improving the gain and efficiency as well as reduces the cross-polarization level.

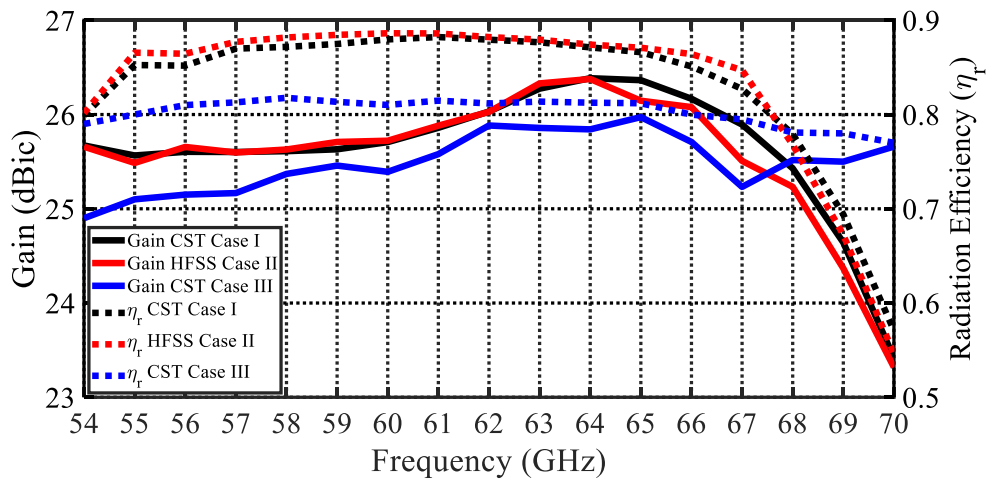


Figure 5.13 Simulated gain and radiation efficiency of the 8x8 antenna.

In Figs 5.15 and 5.15, the simulated radiation patterns of the antenna array at 57, 60, and 64 GHz, respectively, in xz- and yz-plane. Less than -10dB sidelobe level is achieved. Also, low cross-polarization levels can be observed in the differential feeding compared with other feeding methods, which can illustrate the advantage of using such kind of feeding network method.

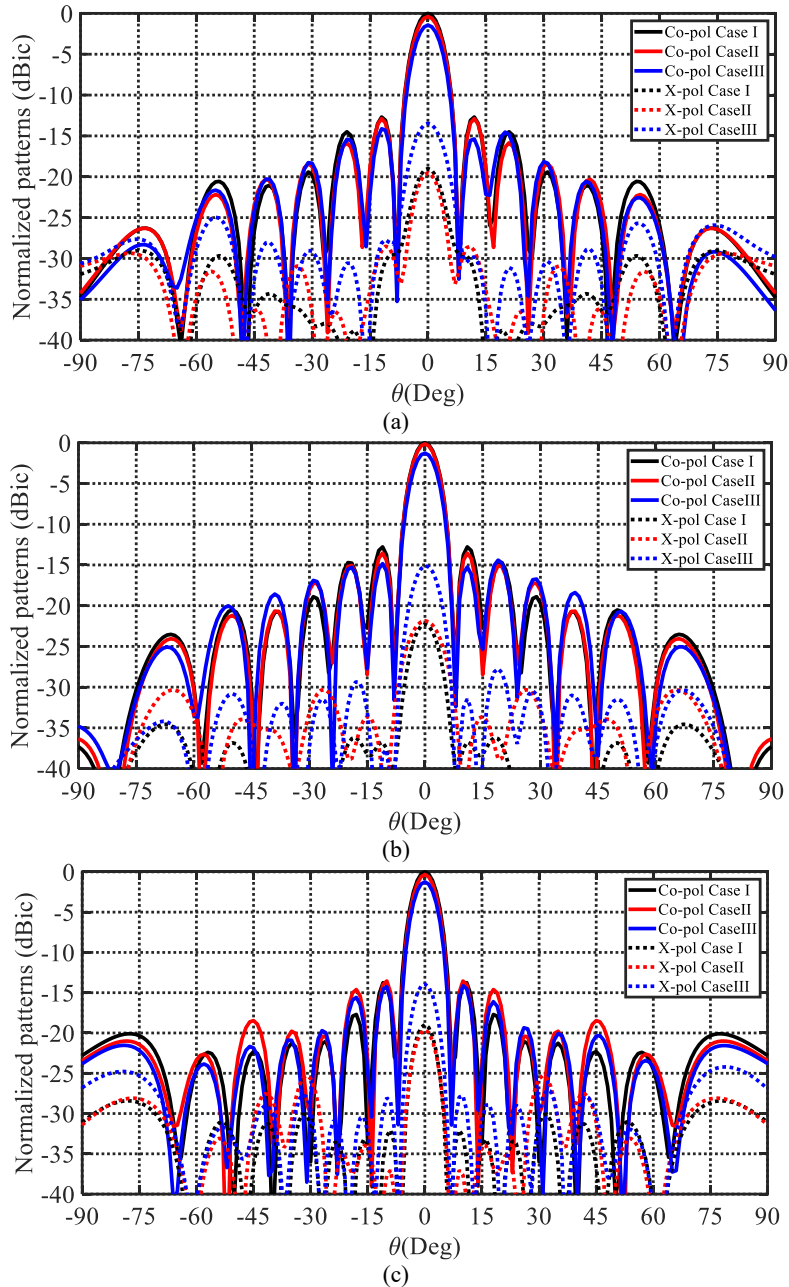


Figure 5.14 Radiation patterns of the 8x8 array in xz-plane at (a) 57GHz, (b) 60GHz, and (c) 64GHz.

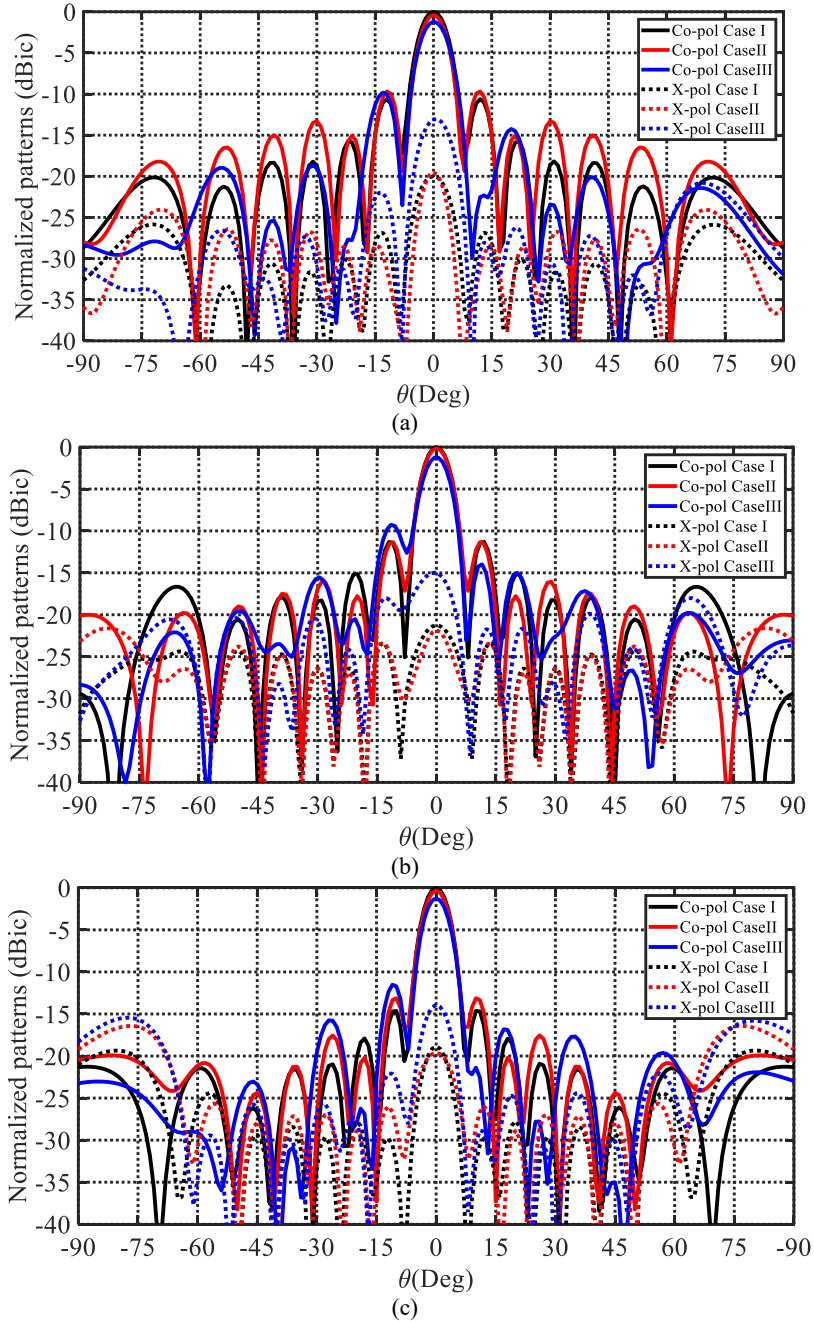


Figure 5.15 Radiation patterns of the 8x8 array in yz-plane at (a) 57GHz, (b) 60GHz, and (c) at 64GHz.

A comparison of the performance of CP antenna arrays operating at the 60-GHz band is reported in Table IV. This comparison includes mainly the structural characteristics (technology for designing the feeding network) and performances. The present work is compact with better gain and efficiency. In fact, due to

the absence of the cavity layer and using ridge gap technology, the proposed design experience less dielectric loss in the feed network compared to SIW.

Table IV. Comparison Between Proposed and Reported 60-GHz Cp Antenna Arrays

	present	[99]	[100]	[101]	[102]	[103]	[80]
Size, mm ²	37 ²	12.3 ²	14×15.2	67.2 ²	6.8 ×6.9	NA	30.6×34
Elements	8×8	4×4	4×4	16×16	2×2	2×2	8×8
# of layers	2	2	2	3	3	2	3
Bandwidth %	18.8	28.1	17.8	5.7	6.7	15.9	18.2
Peak Gain, dBic	26.4	16	16	33.3	12.2	11.43	26.1
$\eta_r >$	82	52.5	34.9	89.6	70	NA	70
AR %	19.8	19.2	15.6	6.4	6.8	15.9	16.5
Technology	MRGW	Stp	CPW	WG	SIW	Stp	SIW

Stp: stripline, CPW: coplanar waveguide, WG: waveguide.

Chapter 6: MILLIMETER-WAVE MIMO ANTENNA SYSTEM AND HIGH GAIN USING DOUBLE SUPERSTRATES

6.1 Millimeter-Wave MIMO Antenna

Recently, in the last decade, spectrum utilization has become more efficient through the long-term evaluation (LTE) network. Moreover, the transmission rates for wireless devices have been improved significantly. Therefore, wireless communication technologies must be developed to meet the increasing demand for high data-rate and high channel capacity. However, the growth of different wireless devices is continually increasing, such that the number of connected devices will be 50 billion by 2020, resulting in a fast-growing flood of data [110]. This significant growth in devices and wireless broadband traffic has a direct impact on future technologies and network architectures. Therefore, the communication industry and research must be prepared with technologies that can satisfy these requirements. The fifth-generation of the communication system (5G) is a promising technology that will add more flexibility in communication for many applications, including vehicle-to-vehicle (V2V), vehicle-to-infrastructure (V2I), peer-to-peer, as well as machine-to-machine. Moreover, 5G will satisfy high data rate demand for a variety of application services, including high definition (HD) videos and Internet of Things (IoT) [110], [111]. Conventional communication technologies use a finite frequency spectrum; this inspires the researchers to look at higher frequencies to achieve these new requirements [112]. Currently, research results show that 5G systems are expected to use multiple-input, multiple outputs (MIMO) to increase the communication channel capacity along with the mm-Wave to achieve high data rates and provide a small physical size for the antenna array. Hence, hundreds of antenna elements, along with other components, can utilize a relatively small area [112-119]. However, some hardware constraints can be added. In addition, mm-Waves have different propagation conditions and atmospheric absorption [120]. Furthermore, it has been estimated that over 80% of the total data traffic would come from indoor communication by 2020 [120]. Therefore, mm-Wave frequency bands can find broad applications for indoor communication. Several newcomer 60 GHz standards, including Wireless HD and IEEE 802.11ad (5G Unlicensed WiFi), are developed for short-range wireless personal area networking (WPAN) to support high data rates [121], [122]. Also, WiFi technology has started using MIMO concepts in the next wireless communication systems at mm-Wave in order to serve a significant number of users with high data rates [123]. Therefore, a new Unlicensed WiFi IEEE 802.11ay standard has been developed to support throughput of at least 20 Gbps in the 60 GHz band [124] to be used for indoor access points, as shown in Fig 6.1.

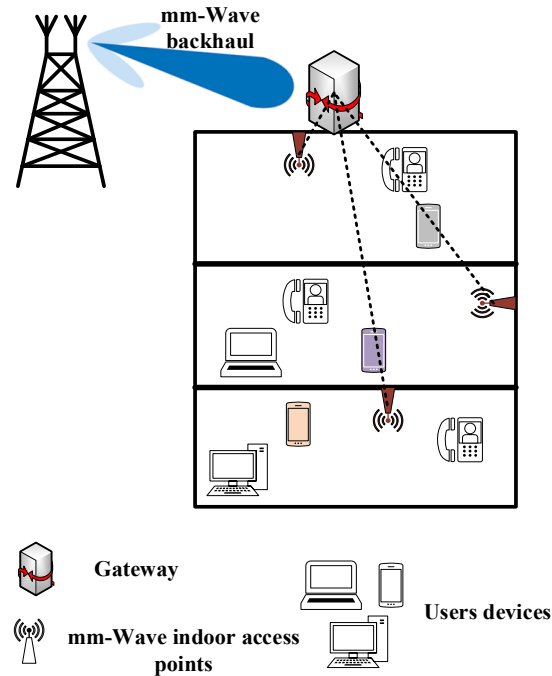


Figure 6.1 mm-Wave Indoor network architecture.

5G small cells can be deployed using micro/pico base stations on the sides of buildings connected to mm-Wave gateway transceivers that can provide backhaul and 5G access [125]. For a 5G communication system, each mm-Wave link should have at least two orthogonal polarizations to support multi-communication channels. Multiple channels can be realized at the front-end level of the radio frequency (RF) through the multibeam antenna array using beam-forming networks such as Butler-matrix and Rotman-lens [126-129] or using MIMO antenna systems. The main difference between the beam-forming networks and MIMO antenna systems is the way that the multibeam is generated. In the beam-forming networks, the beams radiating from the same antenna elements, which require a feeding network that can provide orthogonal beams. However, in the MIMO antenna system, each beam radiates from a separate subarray antenna that works independently. Beam-forming networks become more complicated to generate multiple beams in two-dimensional that should have orthogonality between these beams for good performance [130]. Moreover, mm-Wave will be used in a cell radius (<100 m) to minimize high path loss. Therefore, a high gain is indispensable, especially at 60 GHz, to compensate for the higher path loss [131]. The path loss is directly proportioned to the distance between the transmitter and the receiver; hence, mm-Wave must be used in line-of-sight (LOS) transmissions with highly directional antennas. The antenna array can be used to achieve high gain. However, using antenna arrays in beam-forming networks

leads to some design complexity, such as the spacing between the elements must be less than the half wavelength of the highest frequency of the operating band, also, as the antenna array size increases, the range of the beam tilt decreases. Furthermore, the antenna feed network can be lossy and limit the dimension of the antenna arrays. Feeding network losses mainly depend on the technology used to guide the electromagnetic signals. On the other hand, the MIMO antenna system performance mainly depends on the correlation between the antenna elements of an array.

Therefore, the sub-array antenna for MIMO needs to be designed in a way that the electromagnetic waves will be received de-correlated. This de-correlation can be achieved by separating the antenna arrays spatially or by changing their polarizations [110]. To overcome the feeding network losses, the gap waveguide technology is one of the promising technologies that can reduce those losses at mm-Wave, as mentioned in the previous chapters. Here, we provided an 8x8 high gain antenna array without a backed cavity in the 60 GHz band with good radiation pattern performances. The feed network is designed using MRGW, which adds flexibility and a compact profile. Then we introduced a high gain wideband 4x4 MIMO antenna system to cover 60 GHz. The MIMO antenna system consists of four subarrays of 8x8 elements, and each works independently. The 4x4 MIMO antenna system is designed for an indoor application that can be used and integrated easily with the other components at the physical layer for 5G WIFI devices.

6.1.1 Design procedures

The design of the antenna array is based on using microstrip ridge gap waveguide (MRGW) for the feeding network that can be summarized as follow:

1. Design the electromagnetic gap (EBG), which mainly consists of an artificial magnetic conductor (AMC) surface represented by metal pins topped by a substrate. Then an air gap is enclosed by an upper conducting plane. The EBG suppresses the surface waves, parallel plate mode wave, and the undesired wave propagation within our operation frequency band and allows only one mode to propagate. Using such technology will decrease the coupling between the MIMO antenna ports and improve system performance. The dimensions of the EBG unit cell and the stopband are the same as in Chapter 4.
2. Design the single element that will cover the 57–64 GHz band the same as in Chapter 4.
3. Design an 8x8 antenna array and the feeding network based on the microstrip ridge gap waveguide

(MRGW) as in [84]. This 8×8 antenna array will be used as a subarray in the MIMO antenna.

6.1.2 Sub-array antenna (8×8) design

In order to design a planar array structure with 8×8 antenna elements, a corporate feeding network is required with power dividers. The configuration of the structure is illustrated in Fig 6.2 with initial design parameters calculated from [84]. The antenna array is excited with WR-15, where the electromagnetic fields (mode TE_{10}) transform to the MRGW mode quasi-transverse electromagnetic mode quasi-TEM. The same transition that has been mentioned in Chapter 4 is used.

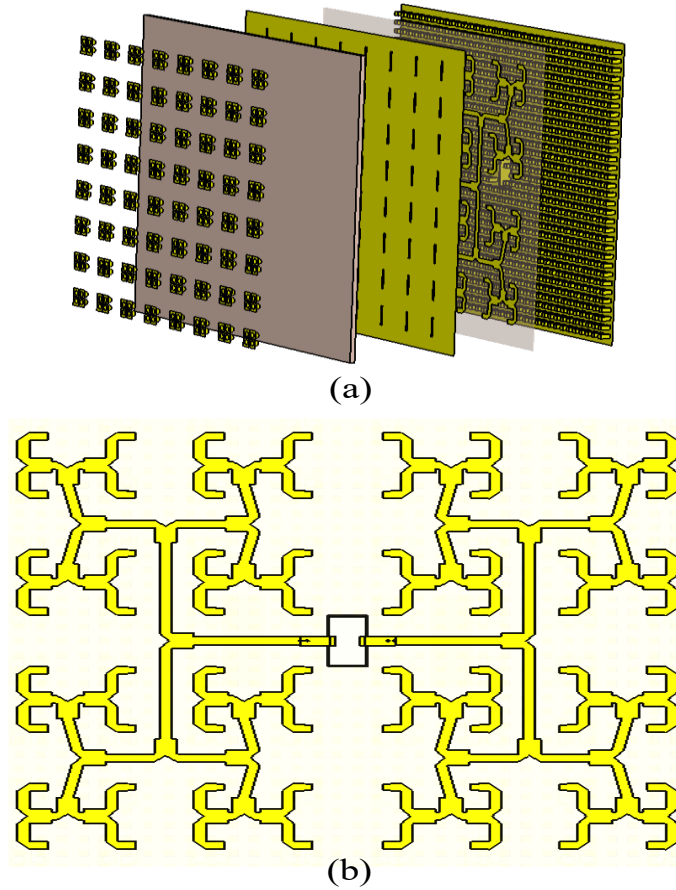


Figure 6.2 Configuration of the 8×8 -element array antenna.

The whole feeding network is optimized using the same effective input impedance in Chapter 3; however, different feeding networks are used. In Chapter 3, we used a feeding network where all the elements are in phase; on the other hand, here, we used differential feeding. The simulated reflection coefficient is shown in Fig. 6.3 using CST and HFSS with < -10 dB reflection coefficient bandwidth

covering 57–67.8 GHz with a good agreement between the two full-wave analysis computational tools.

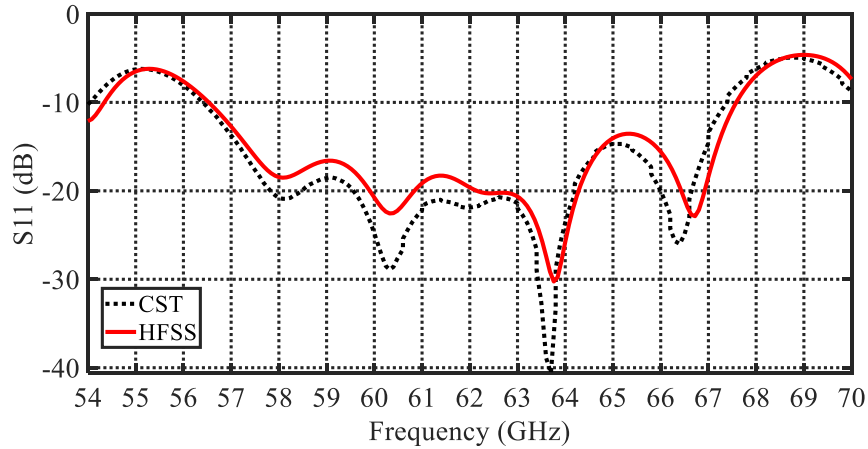


Figure 6.3 Simulated S-parameters of an 8×8 antenna array.

The far field characteristics of the 8×8 antenna array should be investigated because they represent a sub-array element in the MIMO system. The total gain is > 26 dB with radiation efficiency higher than 83% over the operating band, as shown in Fig 6.4.

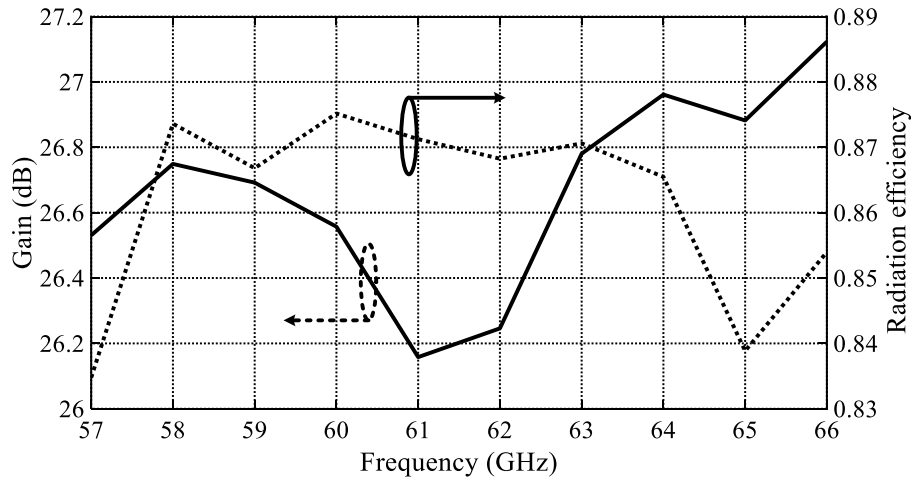


Figure 6.4 Simulated gain from the full-wave and total radiation efficiency of the 8×8 element array antenna.

The simulated radiation patterns of the 8×8 antenna array at 57, 60, 63, and 66 GHz in E-, H-plane, and 45°-plane are shown in Figs. 6.5–6.7. The radiation patterns are symmetrical with sidelobe levels in both E- and H-plane around -11.5 dB.

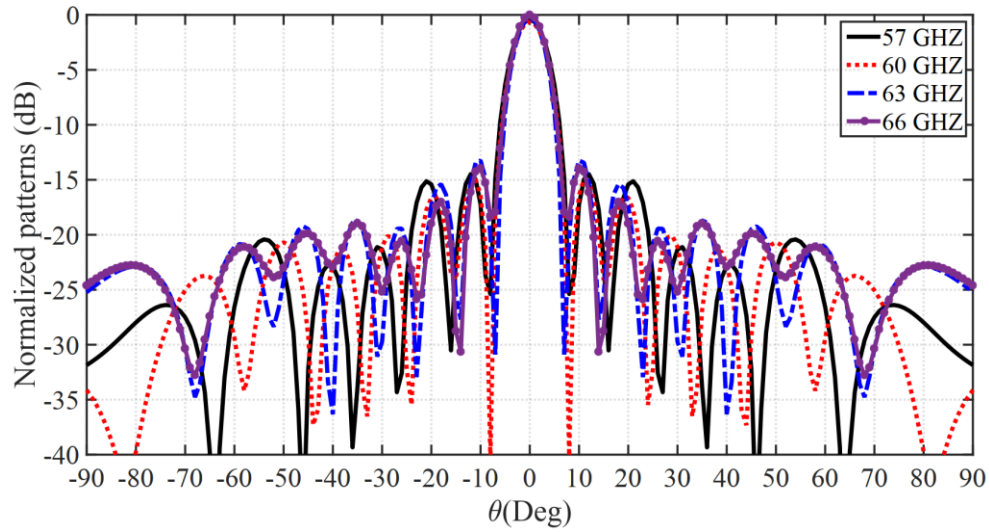


Figure 6.5 E-plane radiation patterns of the 8x8 array at frequencies 57, 60, 63, and 66 GHz.

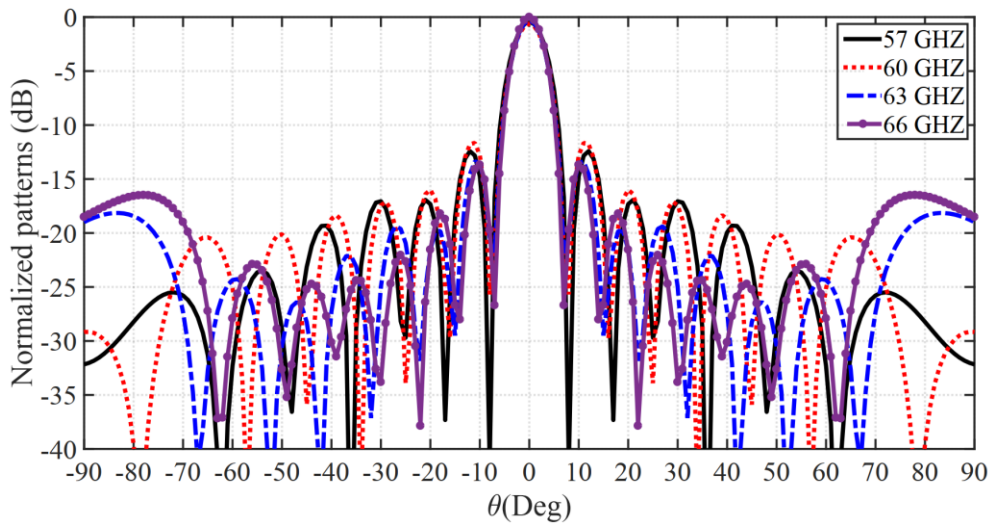


Figure 6.6 H-plane radiation patterns of the 8x8 array at frequencies 57, 60, 63, and 66 GHz.

However, in the 45° -plane, the sidelobe level is below -25 dB over the operating frequency band. It is essential to mention that the differential feeding from the middle provides low cross-polarization and symmetric radiation patterns.

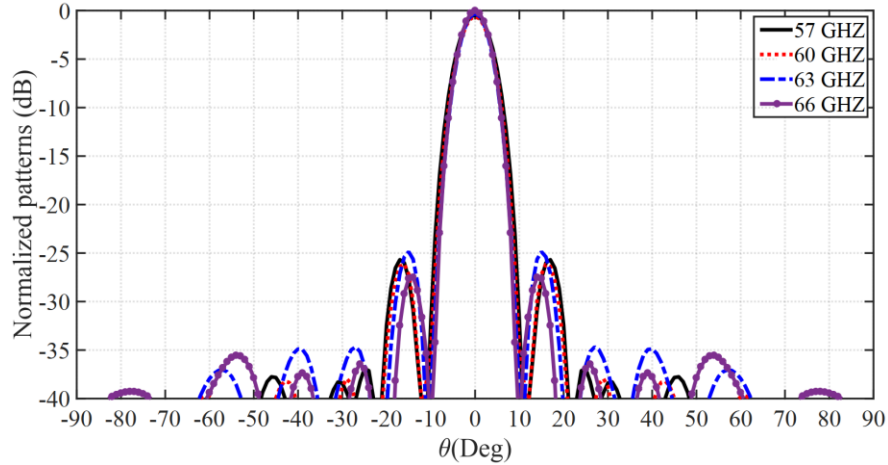


Figure 6.7 45°-plane radiation patterns of the 8x8 array at and frequencies 57, 60, 63, and 66 GHz.

6.1.3 Orthogonal 4×4 MIMO antenna design

Using an 8×8 antenna array as a sub-array, a 4×4 MIMO antenna system is designed. The geometry of the array is described as such; the polarization of each MIMO antenna element is orthogonal. This orthogonality is achieved by changing the polarization of the excitation source such that the direction of the electric field at each sub-array is orthogonal with respect to the neighbor sub-array, as shown in Fig 6.8. Then the 4×4 MIMO antenna system is analyzed. The simulated reflection coefficients for the 4 ports are below -10 dB for the frequency range 56.5-67.5GHz, as shown in Fig 6.9. The port reflection coefficients are almost the same, which is mainly due to the excellent isolation indicating small interaction between them. In Fig 6.10, the corresponding isolations between adjacent ports are shown. Isolation of more than 45dB is achieved, which indicates a possible excellent performance for the MIMO system. It can be pointed out that the nature of the MRGW plays a prominent role in enhancing port isolation. In Fig 6.11, the gain and the radiation efficiency of the four ports are shown where the performance of the isolated subarray is conserved due to the high isolation between the subarrays.

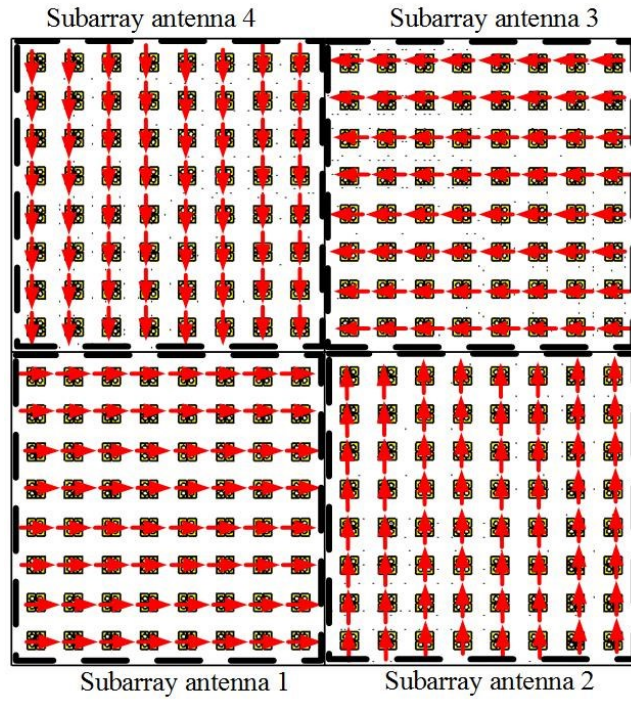


Figure 6.8 Orthogonal 4x4 MIMO antenna design with the electric field direction in the coupling slot at each subarray.

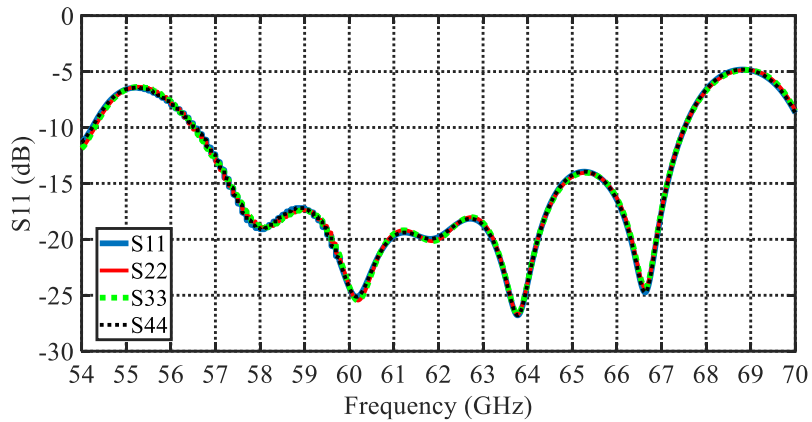


Figure 6.9 Simulated S-parameters of the four sub-array antenna.

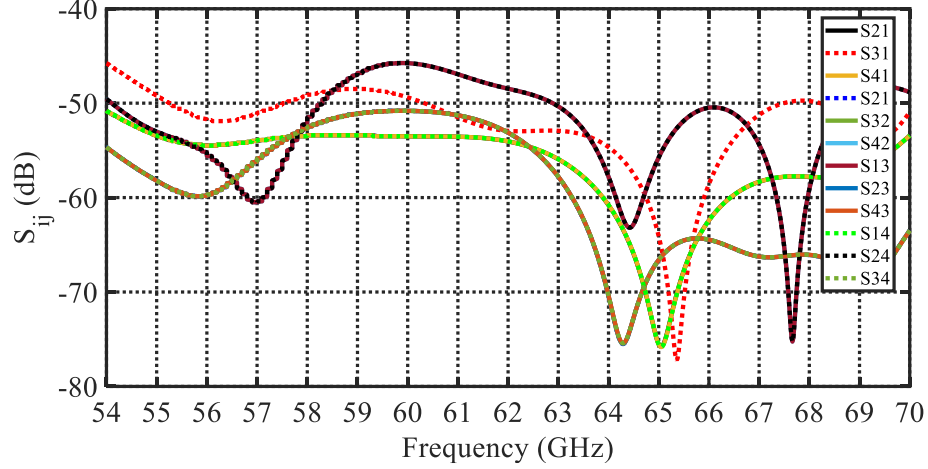


Figure 6.10 Simulated S-parameters (isolation) between the ports of the four subarray antennas.

The spherical far field components are used to calculate the envelope correlation coefficient (ECC ρ_e), and the diversity performance of the MIMO antenna array [132] is evaluated, as shown in Fig 6.12. The envelope correlation coefficient ρ_e is calculated from

$$\rho_e = \frac{|\iint_{4\pi} [\vec{F}_i(\theta, \phi) * \vec{F}_j(\theta, \phi)] d\Omega|^2}{\iint_{4\pi} |\vec{F}_i(\theta, \phi)|^2 d\Omega \iint_{4\pi} |\vec{F}_j(\theta, \phi)|^2 d\Omega} \quad (6.1)$$

where $F_i(\theta, \phi)$ and $F_j(\theta, \phi)$ are the three-dimensional antenna field radiation pattern when the i^{th} and j^{th} ports are excited, respectively, and Ω is the solid angle. The channel capacity, C_{MIMO} in (bit/s/Hz), can be calculated for $N \times N$ MIMO antenna system as [131]:

$$C_{MIMO} = \sum_{i=1}^N B \log_2(1 + SNR) \quad (6.2)$$

where N , B , and SNR are the number of antenna elements, bandwidth in (Hz), and the signal to noise ratio, respectively.

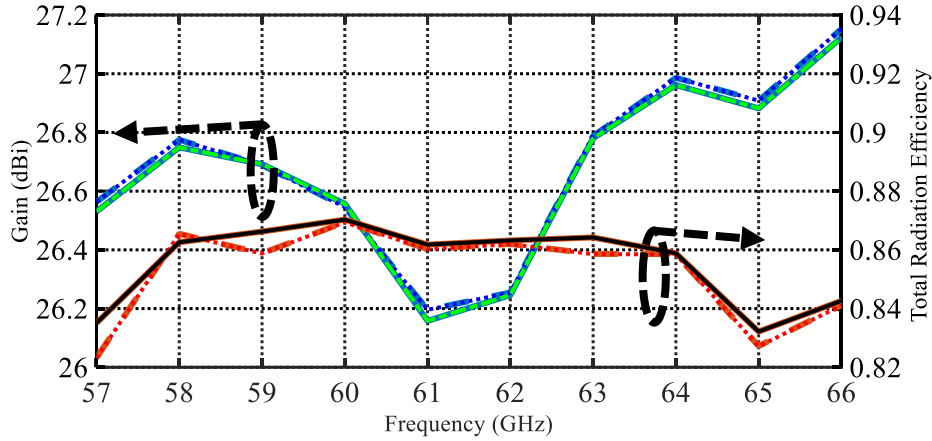


Figure 6.11 Simulated gain from the full-wave and total radiation efficiency of the four subarray antennas.

Calculation of the correlation coefficient is performed using the formula 6.1. ECC values are very low (way less than 0.5), which is the accepted maximum value [133], as shown in Fig. 6.12. It can be observed that ρ_{e13} increases as the frequency increases due to the grating lobes' contribution as the radiation from different sub-arrays interact with each other. The decorrelation between Port 1 and Port 3 is the spatial decorrelation because both Ports 1 and 3 have the same polarization; however, the distance between the antennas for these ports is more than one wavelength. On the other hand, ρ_{e12} and ρ_{e14} are not affected because of the orthogonality of the polarization decorrelation. Therefore, a lower ECC, better isolation between the communication channels, and high diversity is achieved.

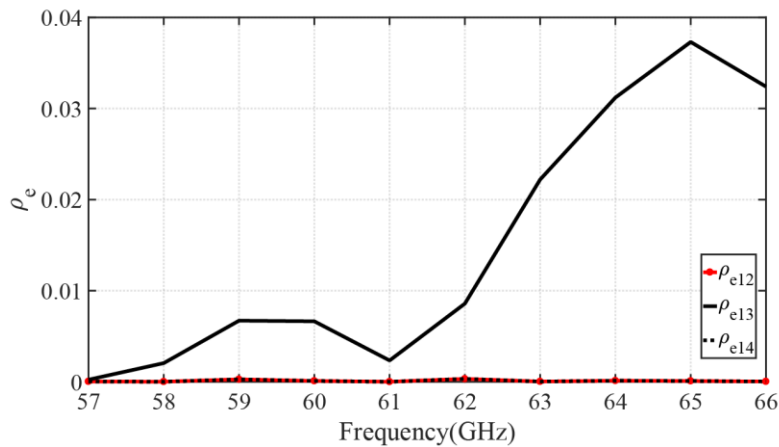


Figure 6.12 Envelope correlation coefficient between four sub-array antennas

6.2 Antenna Array based on Microstrip Ridge Gap Waveguide using Double Superstrates

6.2.1 Single ME-dipole antenna

It is known that the use of the superstrate dielectric layer enhances the antenna gain, which is equivalent to an increase of the virtual radiating aperture that exceeds that physical aperture size. Therefore, study the single element helps in approximately determine the virtual aperture and consequently helps in determining the proper distance between the elements in an array case. Therefore, the single radiating element needs to be designed first. Several research efforts have been conducted to increase the gain using superstrate at 60 GHz. In [134, 135], a 2×2 slot antenna array is designed. In [134], the maximum gain was 17.7dBi, with an impedance bandwidth of 33.8% between 56.5-79.5 GHz. A maximum gain is achieved in [135] was 16.6 dBi with an impedance bandwidth of 13.3% between 56-64 GHz. However, the gain bandwidth was limited, and radiation patterns had high sidelobe levels in both works. Also, in [136] and [137], a single element with a superstrate has achieved 16.5 and 14.9 dBi gain, respectively. However, the gain enhancement was achieved within a narrower bandwidth. Moreover, in [138], a double dielectric superstrate layer is used to increase the gain of a 1×8 microstrip antenna array with narrow bandwidth, and a maximum gain of 16.75dBi is achieved. Here, a ME-dipole antenna element [139] is excited by a narrow slot, which is coupled to MRGW, is selected. The antenna is built on a substrate RO4003C with a dielectric constant of 3.83 and a thickness of 0.508 mm. The MRGW guideline is realized using metal pins as AMC that allows only one mode to propagate within a specific frequency band with the same dimension, as described in the previous chapters. The ME-dipole provides a gain of 8.8 dBi; nevertheless, the gain is enhanced using a dielectric superstrate acting as a lens above the ME-dipole antenna [140]. As such, a high gain can be achieved through multiple reflections between the reflecting plane (the ground plane of the ME-dipole) and the superstrate with dielectric constant (ϵ_{r_sup}). The multiple reflections cause standing waves and stored energy with a high-quality factor that increases the antenna gain. However; for constructive performance, some conditions are required, such that the ground plane need to be separated by $n\lambda_{eff}/2$ (n is an integer) from the superstrate dielectric that has $\lambda/(4\sqrt{\epsilon_{r_sup}})$ thickness [140]. It is essential to point out that the ground plane here is the plane that has the slot, where the substrate RO4003C is deposited for the ME-dipole.

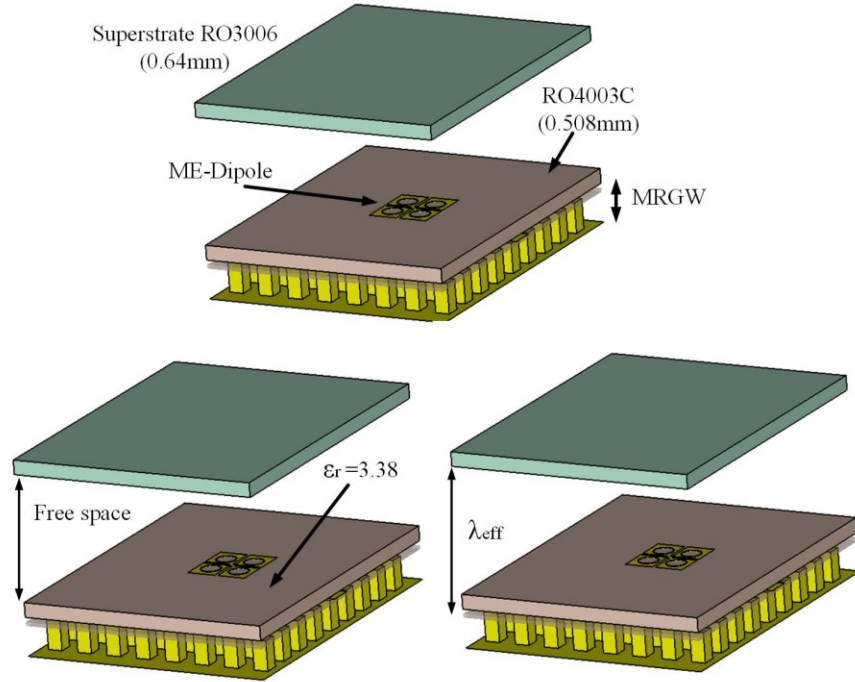


Figure 6.13 Schematic of the EM-dipole with the superstrate RO3006 and the MRGW.

Consequently, the gap between the substrate and the metal plate should be calculated based on the effective dielectric constant, not the free space. Fig 6.13 shows the single element with the superstrate dielectric RO3006 ($\epsilon_{r_sup} = 6.15$) that has the dimensions of $8.5 \times 7.8 \times 0.64 \text{ mm}^3$ and λ_{eff} ($0.95 \lambda_{air}$ at 60 GHz) above the ground plane. The structure is optimized to cover the 60 GHz band with excellent performance of reflection coefficient and gain, as shown in Fig 6.14. Another superstrate dielectric RO3010 ($\epsilon_{r_sup} = 10.2$) with dimensions of $8.5 \times 7.8 \times 0.5 \text{ mm}^3$ is used at distance $0.5 \lambda_{eff}$ ($0.4 \lambda_{air}$ at 60 GHz). The superstrate distance from the ground of the radiating element has a direct effect on the reflection coefficient and the performance of the superstrate to enhance the gain; for a compact prototype, the distance between the superstrate and the substrate ground of the antenna should be $0.5 \lambda_{eff}$. However, at this distance, the reflection coefficient is disturbed by the wave reflection between the superstrate and the radiating elements. Therefore, the structure needs to be optimized. Placing the superstrate at λ_{eff} has less effect on the reflection coefficient and maintain the compactness in case of using two superstrates (one at $0.5 \lambda_{eff}$ and the second at λ_{eff}).

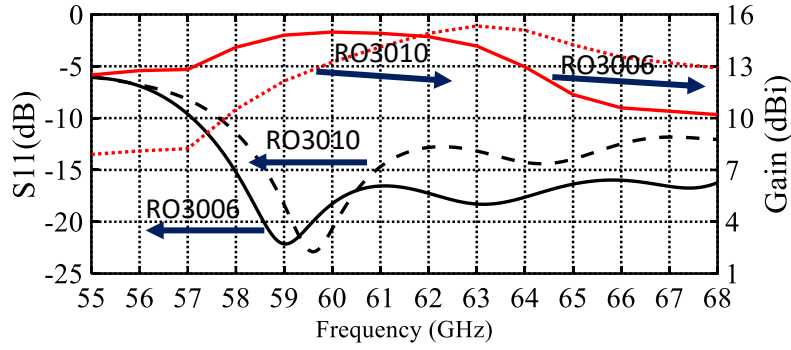
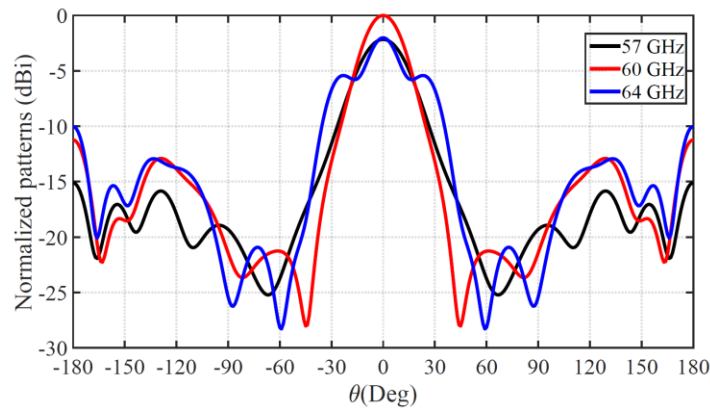
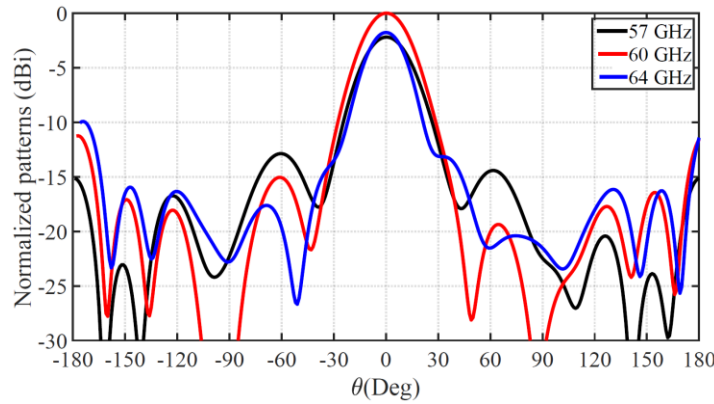


Figure 6.14 Simulated S11 and gain from the full-wave using a single ME-dipole antenna with different superstrates.



(a)



(b)

Figure 6.15 Radiation patterns of the single ME-dipole using dielectric superstrate RO3006. All are normalized to the gain at 60 GHz: (a) E-plane (b) H-plane.

The radiation patterns at 57, 60, and 64 GHz are shown in Figs. 6.15 and 6.16 for the two different superstrates. It can be pointed out that using the dielectric superstrate increased the gain in the broadside

direction within a narrower frequency band. The gain at 60 GHz increased from 8.8 dBi (without superstrate) to more than 14 dBi using RO3006 superstrate, which is equivalent to increasing the aperture size that is corresponding to using an array of 2×2 , ignoring any possible losses. Using superstrate dielectric has a direct effect on suppressing the grating lobes as well as SLL; the effect on SLL is investigated using antenna array structure.

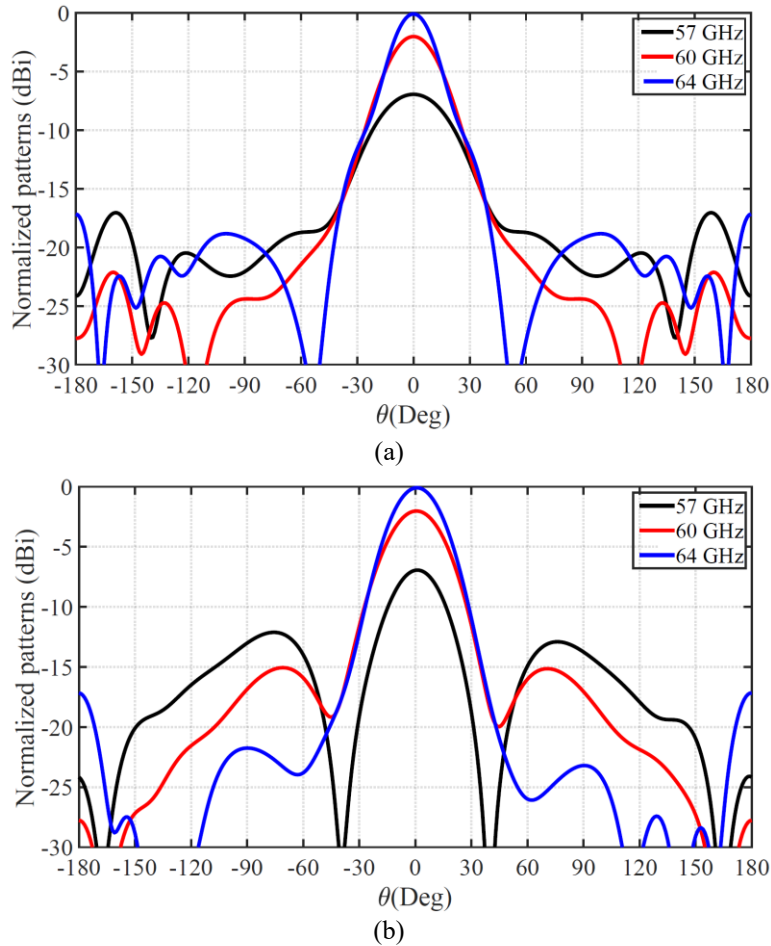


Figure 6.16 Radiation patterns of the single ME-dipole using dielectric superstrate RO3010. All are normalized to the gain at 64 GHz: (a) E-plane (b) H-plane.

6.2.2 2×2 ME-dipole array antenna

Here, we design a 2×2 ME-dipole array using a dielectric superstrate to enhance the gain. As the antenna gain is directly related to the aperture size of the antenna [141], the ground plane size of the single element is used as it is equivalent to its aperture size that should not overlap with the aperture of the neighboring

elements of the 2×2 array. However, using the same ground area size to design the array increases the spacing between the elements to exceed one, which certainly causes grating lobes. The new elements with the superstrate are forming the new array. Thus, their element radiation pattern beamwidth is reduced, and in turn, grating lobes are significantly reduced. Thus, the dielectric superstrate boosts the gain in the broadside (main beam direction) and making the relative level of the sidelobe and grating lobes reduced to an acceptable level. Thus, wide spacing between the elements can be resolved. The 2×2 elements are fed by a parallel feeding network that consists of quarter-wavelength transformers, as shown in Fig 6.17 using MRGW and the empirical expressions in [84].

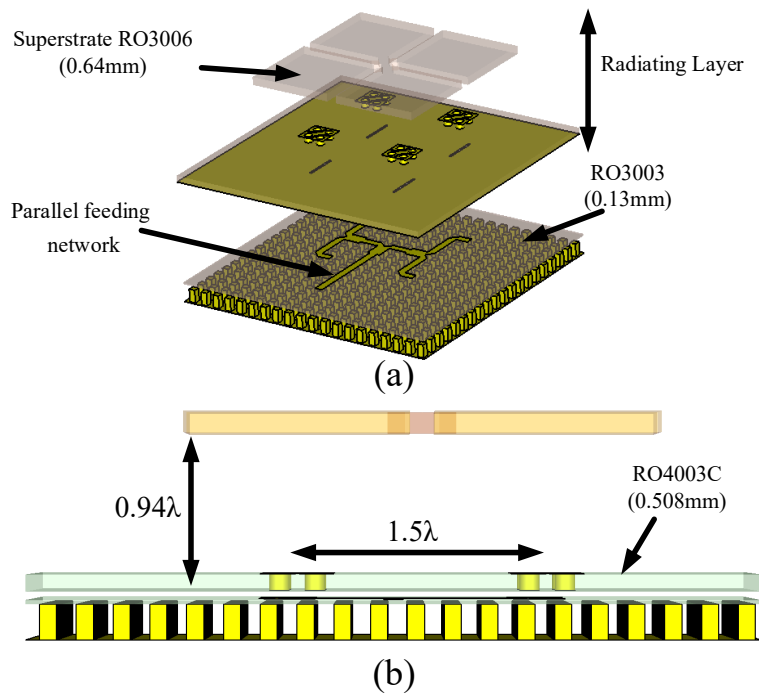


Figure 6.17 Schematic of the 2×2 ME-dipole with one dielectric superstrate and the MRGW.

The distance between the ME-dipole elements is equal to 1.5λ , with an aperture area $22 \times 22 \text{ mm}^2$. The structure has been optimized using CST, and 21.6% of impedance bandwidth is achieved with radiation efficiency better than 85%. Besides, a peak gain of 20.28 dBi at 61GHz is achieved and better than 19 dBi between 58.2-63.5 GHz, as shown in Fig 6.18.

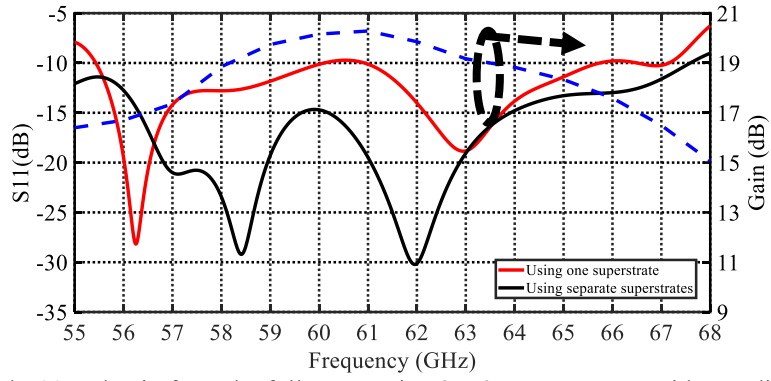
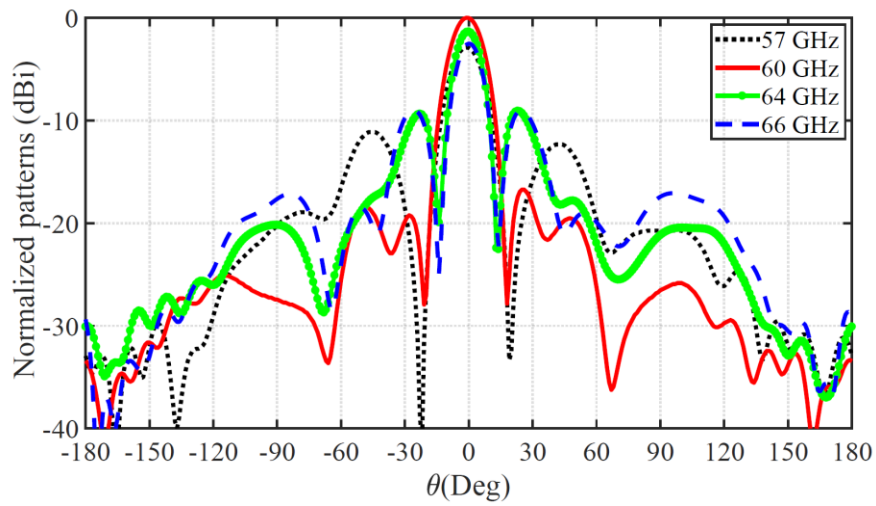
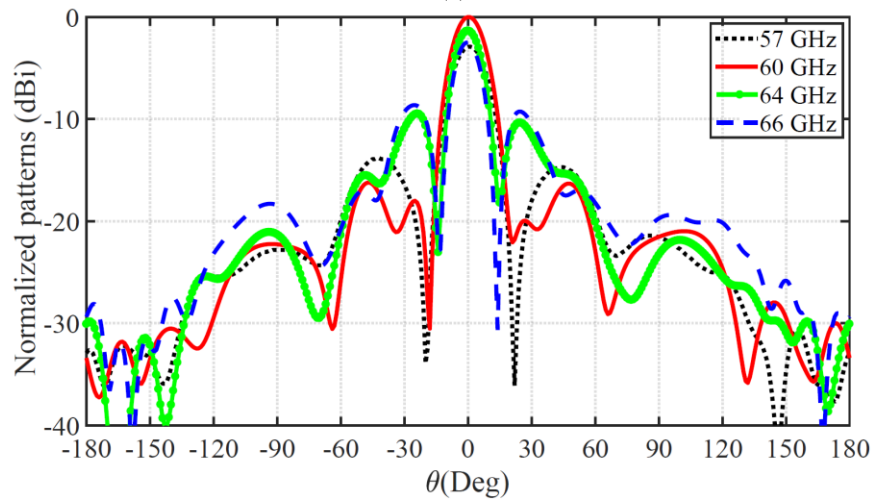


Figure 6.18 Simulated S11 and gain from the full-wave using 2×2 antenna array with one dielectric superstrate.



(a)



(b)

Figure 6.19 Radiation patterns of the 2×2 ME-dipole antennas using one dielectric superstrate. All are normalized to the gain at 60 GHz: (a) E-plane (b) H-plane.

The superstrate cuts are to suppress the surface wave interaction between the radiating elements such that each element in the array has the same environment as the single element by maintaining the same aperture size. The effect of these surface waves can be shown in Fig 6.18 in the case where one superstrate is used without cuts. The effects can be observed in the reflection coefficient level. However, the gain improvement does not cover the whole required frequency band due to the superstrate dielectric resonant behavior that limits the bandwidth. Accordingly, the gain at 57 GHz and 64 GHz is around 17 dBi, which leads to low SLL at these frequencies, as shown in Fig 6.19. To overcome the superstrate bandwidth limitation, two stacked superstrates are used. The second superstrate is inserted between the first superstrate and the ground plane at a distance of $0.5 \lambda_{eff}$ from the ground (metal plate of the MRGW), as shown in Fig 6.20 in order not to increase the original antenna height, then the whole structure is optimized to compensate for the effect of the reflected wave and maintain proper impedance matching of 20% and keep high radiation efficiency (more than 82%).

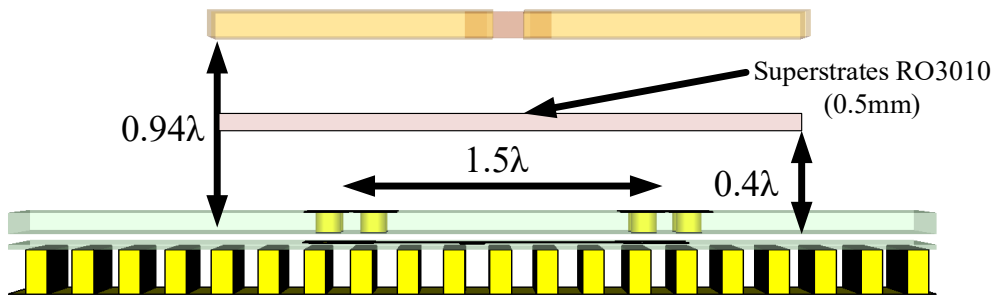


Figure 6.20 Schematic of the 2×2 EM-dipole with two dielectric superstrates and the MRGW.

Each superstrate has its impact at a different frequency to boost the gain, and by overlapping the frequency band of each superstrate, the gain is enhanced over the whole operating frequency band with a maximum gain of 20.5 dBi at 63GHz, as shown in Fig 6.21.

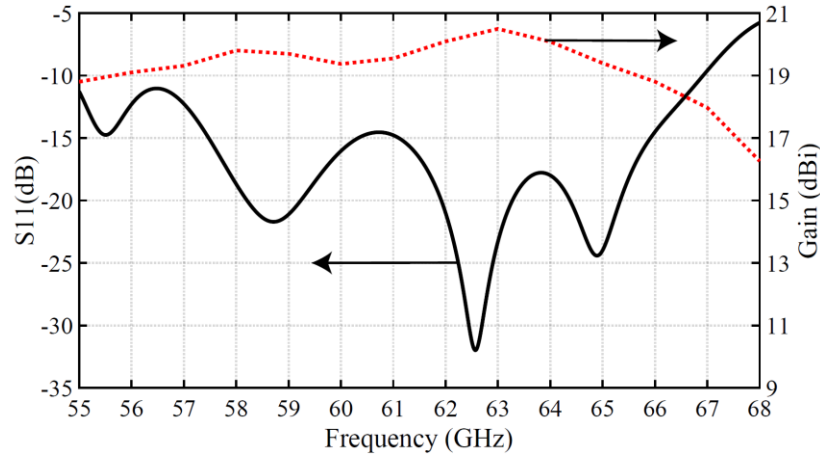
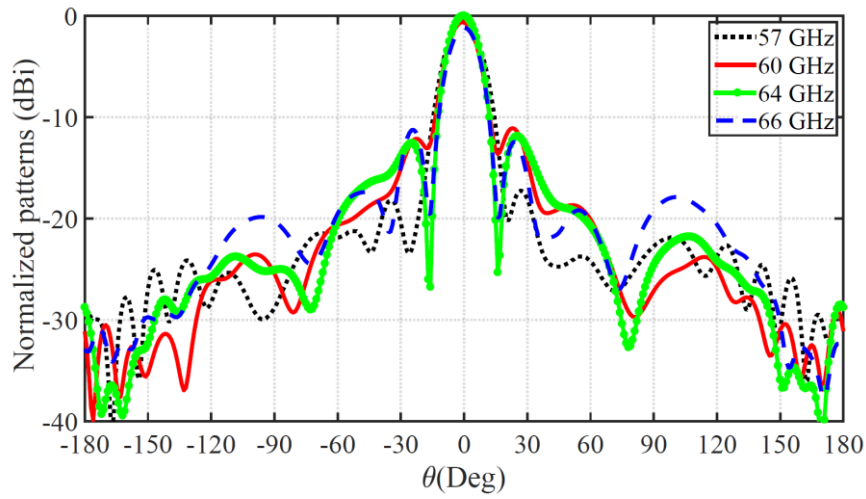
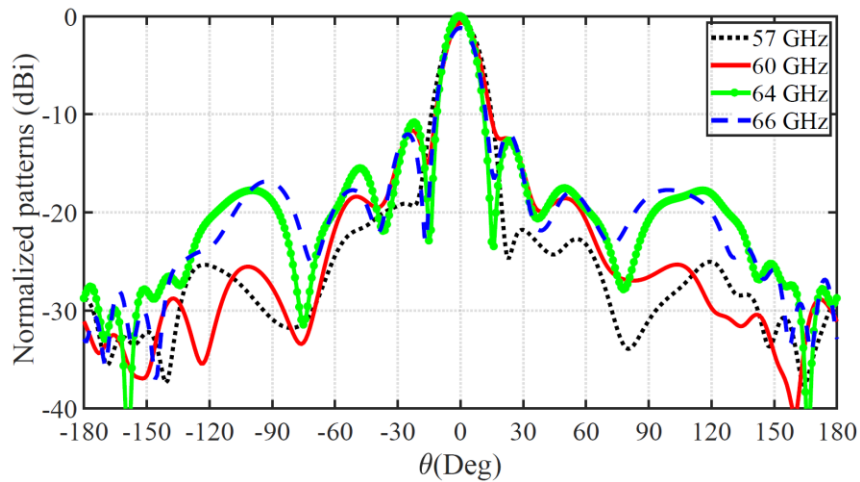


Figure 6.21 Simulated S11 and gain from the full-wave using 2×2 antenna array with two dielectric superstrates.



(a)



(b)

Figure 6.22 Radiation patterns of the 2×2 ME-dipole antennas using two dielectric superstrates. All are normalized to the gain at 64 GHz: (a) E-plane (b) H-plane.

The radiation patterns using two superstrates are shown in Fig 6.22. It is worth mentioning that the superstrate suppresses the grating lobe levels in E- and H-plane, and the gain achieved by 2×2 is equivalent to the gain from 4×4 array of an aperture area of $4.4 \times 4.4 \lambda^2$ (at 60 GHz) without superstrate.

6.2.3 4×4 ME-dipole array antenna

The 60 GHz band requires an antenna system with high gain to compensate for the Oxygen absorption. Using the same ME-dipole element, the 4×4 antenna array is designed with a parallel feeding network along with two superstrates to provide a gain of 8×8 elements. The array structure is shown in Fig 6.23. The aperture area of the 4×4 array is defined as $37.4 \times 37.4 \text{ mm}^2$ with 7.6 mm (1.5λ at 60 GHz) spacing between the elements. The whole structure is excited using WR-15 through a transition from the middle shown in Fig 6.23. The transition provides a differential feeding that can reduce the cross-polarization dramatically. The dimension of the radiating element is shown in Fig 6.24 after tuning. For the quarter-wavelength transformers, the length and width of the power dividers are 1.26 and 1.12 mm. However, the length of the V-shaped junction is 1.17 mm.

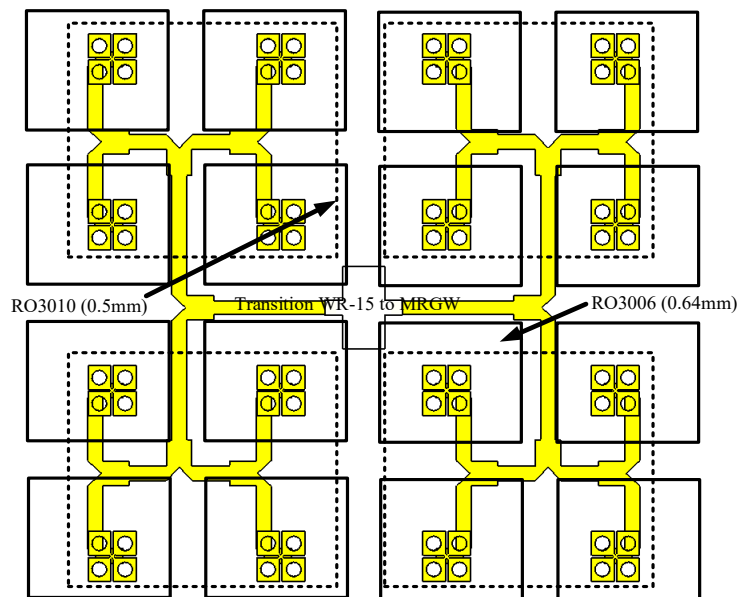


Figure 6.23 Schematic of the 4×4 EM-dipole with two dielectric superstrates and the MRGW.

Two different full-wave analyses are used to verify the simulated results (CST and HFSS). A good agreement between them is observed. An impedance matching of 16.2% (56.7-66.5GHz) with radiation efficiency better than 80% is achieved. A stable gain over the operating frequency band with a maximum of 26 dBi is obtained, as shown in Fig 6.26.

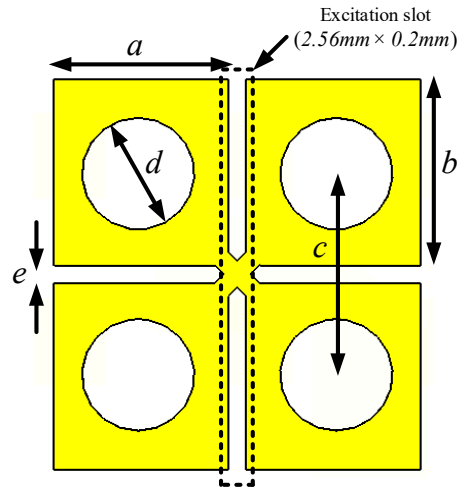


Figure 6.24 ME dipole antenna dimensions ($a = 1.02 \text{ mm}$, $b = 1.1 \text{ mm}$, $c = 1.19 \text{ mm}$, $e = 0.1 \text{ mm}$, and $d = 0.66 \text{ mm}$).

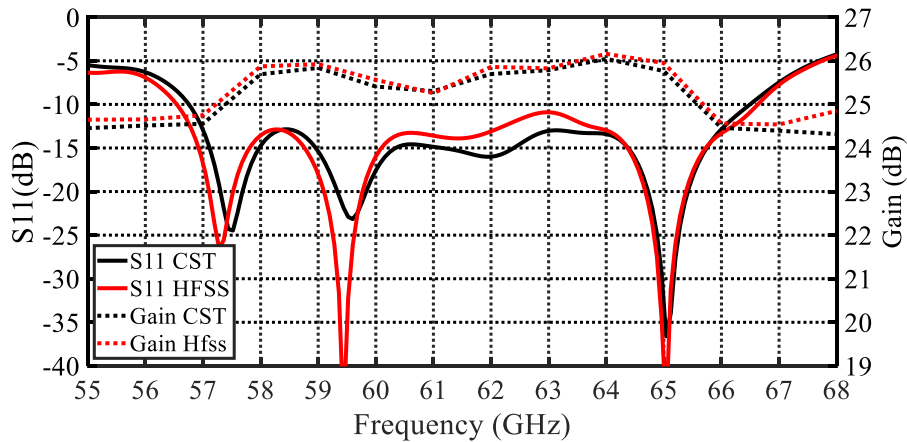


Figure 6.25 Simulated S11 and gain from the full-wave using 4×4 antenna arrays with two dielectric superstrates.

The same gain can be achieved using an 8×8 antenna array of the same aperture area without superstrate ignoring the mutual coupling effect, which, presumably, is significant when the distance between the

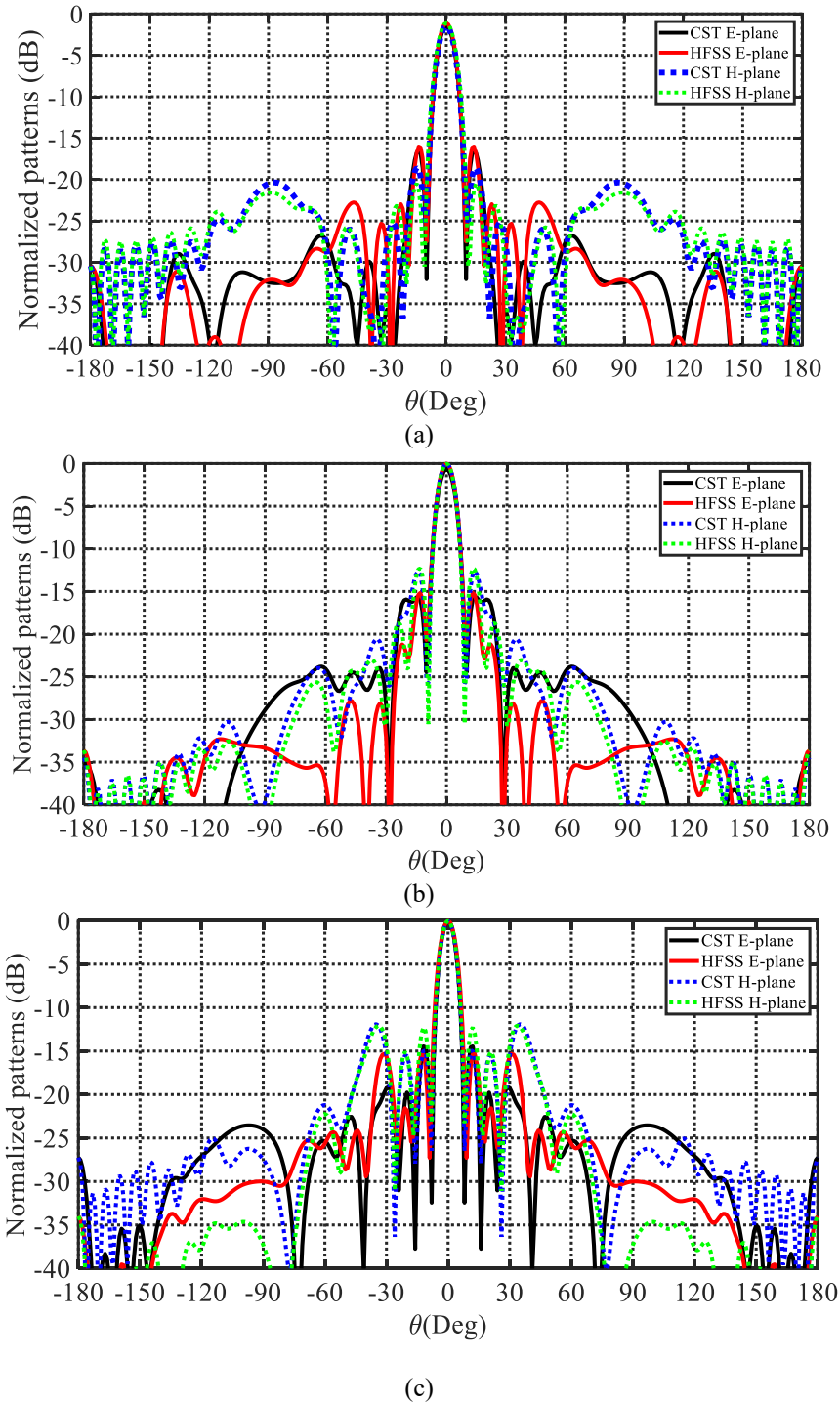


Figure 6.26 Radiation patterns of the 4×4 ME-dipole antennas using the two dielectric superstrates: (a) 57 GHz, (b) 60 GHz, and (c) 64 GHz.

elements are reduced. Therefore, the 8×8 array design is more challenging since the spacing between the elements is less than λ . The radiation patterns are shown in Fig 6.26 with first relative sidelobe levels

around -12 dB in both E- and H-planes with symmetrical radiation patterns with good agreement between the CST and HFSS results. Although the spacing between the radiating elements is more than one wavelength (at 60 GHz), the radiation patterns show low grating lobes, which are mainly suppressed by the superstrate.

6.3 Short-Range Wireless System based on Monopulse Microstrip Ridge Gap Waveguide

Monopulse technique can be used for the direction of arrival (DOA) of a signal in communication by simultaneously comparing the sum and difference of the signal collected from the two ports. It is also useful in the radar system for target tracking by allocating the target direction. Monopulse technique has many other potential applications [142]. A highly directional antenna for millimeter-wave technologies must be used in line-of-sight (LOS) transmissions because the signal in non-LOS consists of the reflected signals becomes weak. Also, LOS transmissions can be assumed since, for millimeter-wave, the cell coverage area shrunk in order to reduce the path loss effect. Therefore, finding the direction of the radiation beam for different millimeter-wave applications is necessary for finding the LOS direction in point-to-point wireless links. The design for a monopulse comparator is usually complicated and heavy, especially for low frequency. A lightweight monopulse comparator for K-band using a microstrip structure was introduced where the radiating elements were placed at the center of the comparator structure, which is designed using hybrid couplers [143]. However, using this technology, the structure was lossy and suffered from high surface wave losses and strong mutual coupling. Also, a monopulse comparator designed based on using hybrid couplers of Substrate Integrated Waveguide (SIW) technology for Ka-band with slot antenna array can be found [144]. However, the fractional bandwidth was 1.2%, and the center frequency 29.25 GHz with a radiation efficiency of -2.65 dB and a maximum gain of 8.1 dBi for the sum channel and a null depth better than -27.7 dB for the difference channel. Monopulse comparator can be implemented using rat-race hybrids and magic tee. Using rat-race hybrids for antenna array has the disadvantage of having one of the output ports is trapped inside the network. In [145]. A monopulse compactor was designed using magic tee and ridge gap waveguide technology for W-band with a fractional bandwidth of 21% at 94 GHz with a gain of 30 dB and maximum null depth of -38 dB. Although using the ridge gap has an excellent performance due to the low losses, using Magic tees brings

complexity to the design. Here, Microstrip Ridge Gap Waveguide (MRGW) is used, providing design flexibility, especially for array design, without disturbing the EBG structure. The proposed comparator network covers the frequency band of 57–66 GHz. It consists of three layers: EBG layer, comparator, and feeding network layer, and radiation layer. The comparator is a printed circuit that basically contains hybrid couplers and phase shifters. Then the signal couples from the comparator circuit to the ME-dipoles radiating elements through slots coupling. Those slots are etched on the metal layer that acts as a common ground for the MRGW and the ME-dipoles.

6.3.1 Monopulse components: Hybrid coupler

MIMO technology is used to improve the communication systems by providing orthogonal channels [131]. The orthogonality at the front end of the radio frequency (RF) can be implemented using a 3dB hybrid coupler. Different 3dB hybrid coupler structures have been investigated based on the guiding wave technologies that have been used in the design. For instance, in [146], a 3-10 dB coupler was implemented using microstrip technology. However, the coupler has an amplitude imbalance of ± 1 dB across the 3.1–10.6 GHz band. Besides, using microstrip technologies are providing high losses and low isolation between the components. In [147], SIW has also been used to design 3dB hybrid couplers at 10 GHz with 15% bandwidth. The coupling magnitude differences, 0.5 dB, and the losses have been reduced by using an air-filled slab. Also, in [148], a 3 dB hybrid coupler was reported using metallic ridge gap waveguide technology; the coupled ports were balanced within ± 0.5 dB over 7% bandwidth. Although the designed coupler has low loss, self-packing and wideband, the fabrication of the metallic ridge gap waveguide technology is costly and has a large profile. In [149], a 3dB hybrid coupler is designed using a branch line coupler that uses quarter-wavelength lines with two different impedances. The coupler is designed to work at 60 GHz based on MRGW using the metallic pins textured surface to act as an AMC. The coupling parameters were between -3 and -4 dB within 8.5% bandwidth.

Here, we present a 3dB hybrid coupler using the short-slot coupling concept. The short-slot hybrid coupler based on MRGW technology can be considered as placing two MRGW side by the side and removing a section of the center wall (coupling section). The length of the coupling section plays a crucial role in determining the coupling ratio of the coupler where this length should be greater than $\lambda_g/2$, where λ_g is the guided wavelength at the center frequency [150]. However, the propagating mode is not a pure transverse electromagnetic mode (TEM) but quasi-TEM. The 3 dB hybrid coupler is shown in Fig. 6.27. In the band of 57-64 GHz, the reflection and isolation between the ports is less than -14 dB. The simulated coupling

at Port 2 and Port 3 is around 3.9 dB at 61 GHz with an amplitude balance of ± 0.3 dB over 57-64 GHz with a nominal phase difference between the output ports of 90° with a maximum variation of 2.5° as in Fig. 6.28 and Fig. 6.29.

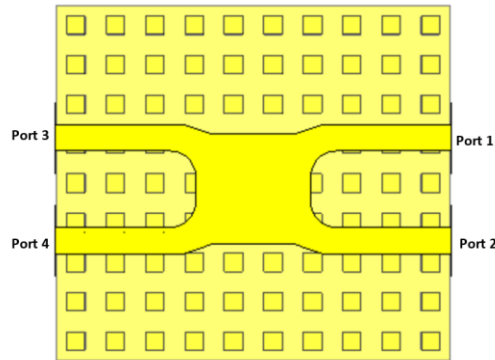


Figure 6.27. 3dB hybrid coupler structure.

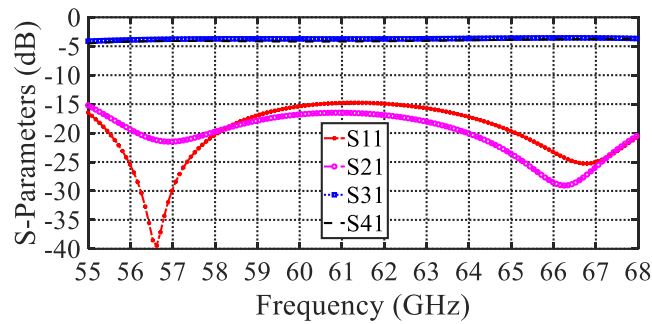


Figure 6.28. Simulated MRGW hybrid coupler scattering parameters.

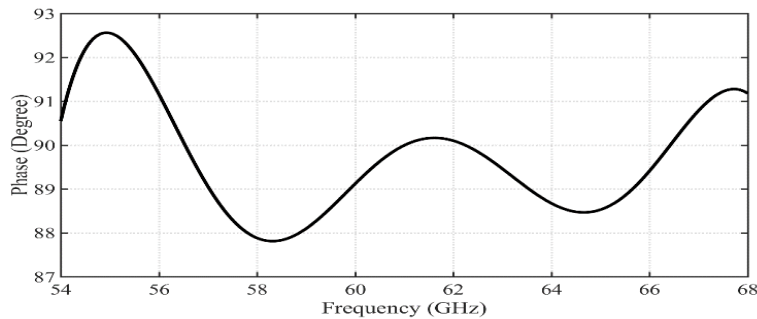


Figure 6.29. Simulated differential phase characteristics of the MRGW.

6.3.2 Monopulse components: Hybrid coupler plus delay lines

The monopulse comparator is designed by using the proposed hybrid coupler and the delay lines. Fig. 6.30 shows the configuration of the comparator network. The comparator has three main input ports: Sum (Σ) and E-plane differences (ΔE), and H-plane difference (ΔH). Port Sum (Σ) is when the whole signals at the output ports are in phase, ΔE is when the signals at the outputs (O/1 and O/2) are in phase, and 180° out of phase of (O/3 and O/4), and ΔH is when the signals at the outputs (O/2 and O/4) are in phase and 180° out of phase of (O/1 and O/3). For Port 4, the signals at the outputs (O/1 and O/4) are in phase and 180° out of phase of (O/2 and O/3).

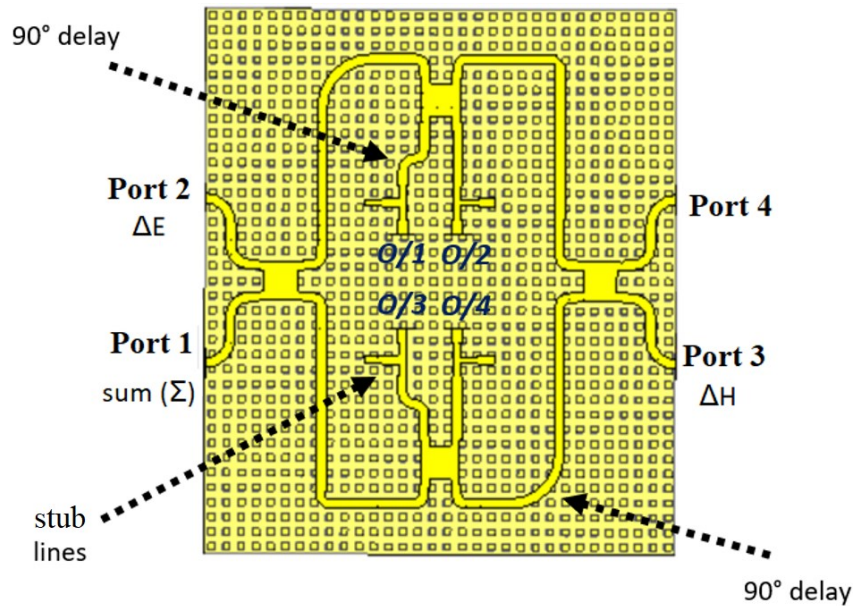


Figure 6.30. The monopulse comparator structure.

The simulated scattering parameters of the input ports are shown in Fig. 6.31, with a reflection coefficient better than -14dB over the frequency band $57\text{-}64\text{GHz}$, and isolation between the input port is better than -17dB . The transmission coefficients have an amplitude balance of $\pm 0.65\text{ dB}$ within the frequency band $57\text{-}64\text{GHz}$ and a maximum variation of 13° , as shown in Fig. 6.32

For the antenna array, a planar monopulse array antenna is designed such that each output port from the comparator feeds a subarray of a 4×4 antenna array. The radiating element is ME, which is similar to the

one used in chapter 3. The structure of the array antenna with the monopulse comparator network is shown in Fig. 6.33.

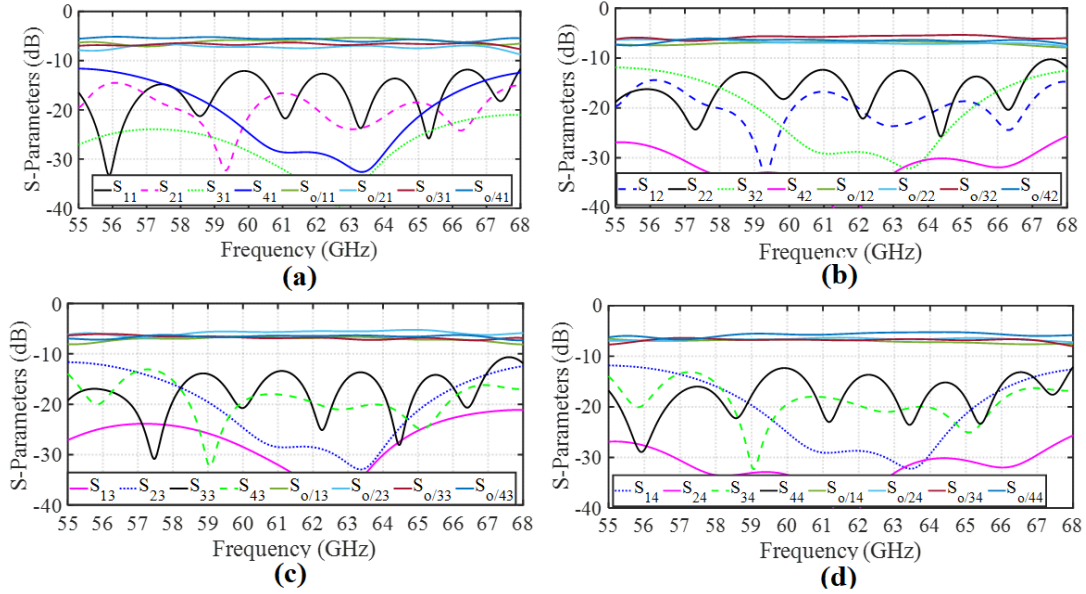


Figure 6.31. Simulated reflection coefficients of the comparator network: (a) mode 1, (b) mode 2, (c) mode 3 and (d) mode 4.

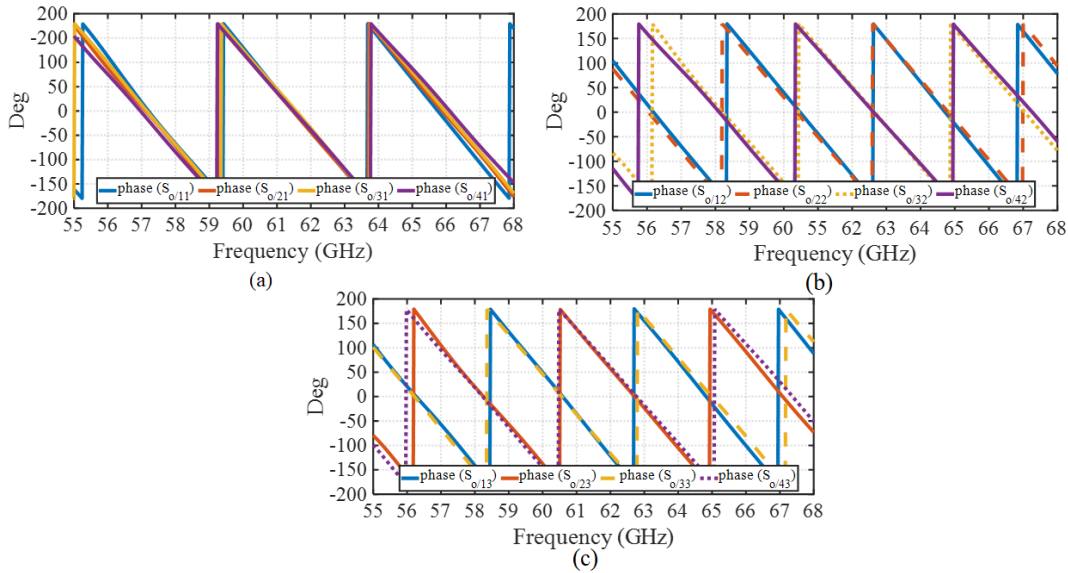


Figure 6.32. Simulated phase variation of the comparator network: (a) mode 1, (b) mode 2, and (c) mode 3.

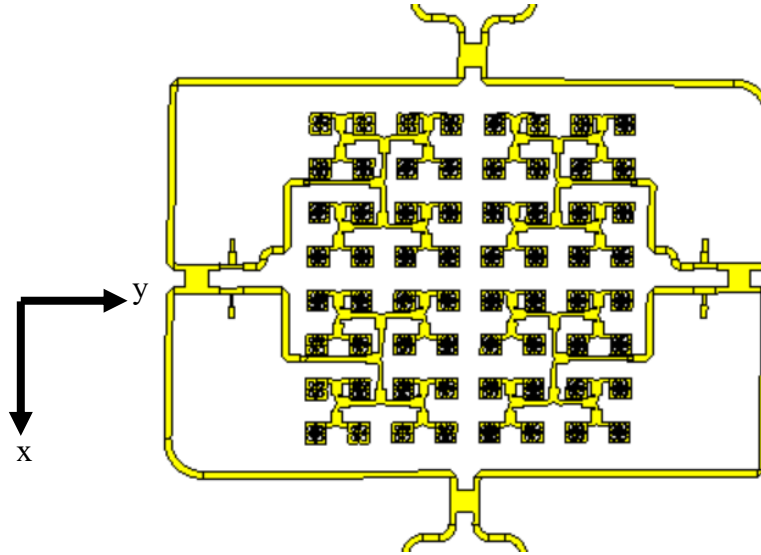


Figure 6.33. 8x8 antenna array of the monopulse comparator structure.

For the antenna array, the simulated reflection coefficients of the input ports are below -14 dB over the frequency band 57–64 GHz, as shown in Fig. 6.34. also, good isolation between the input port can be observed from the simulated reflection coefficient in Fig. 6.35.

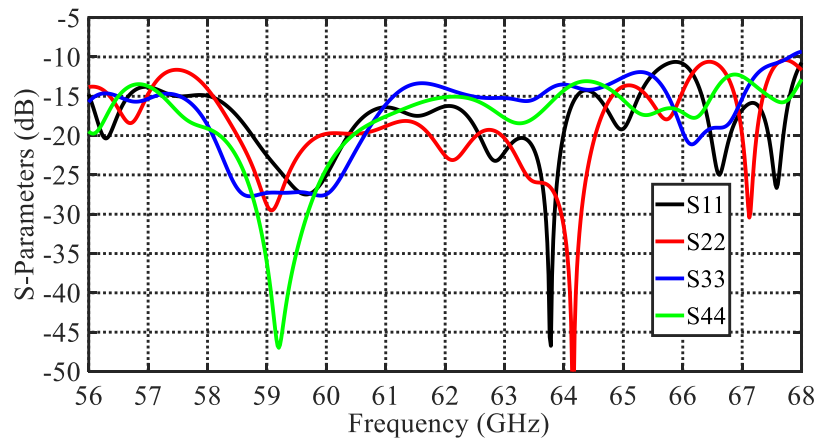


Figure 6.34. Simulated reflection coefficients of the 8x8 antenna array.

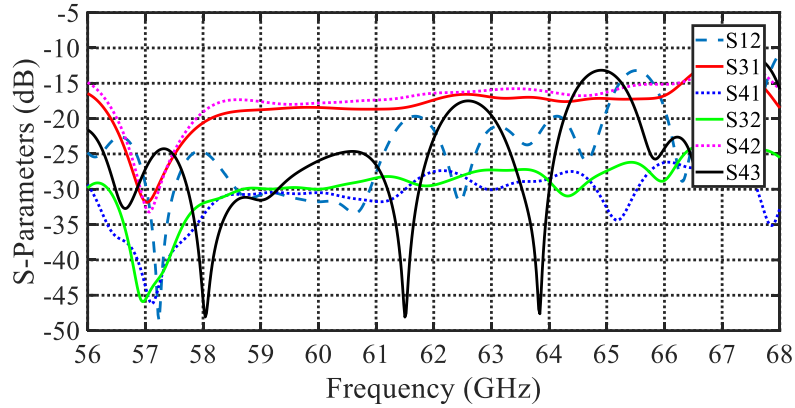


Figure 6.35. Simulated reflection coefficients of the port isolation of the 8x8 antenna array.

Fig. 6.35 illustrates the technique of the radiating pattern forming when the different input ports are excited. The (+) means all the elements within the same subarray are in phase, and (-) means all the elements within the same subarray are in phase and have a 180° phase shift from the adjacent subarray.

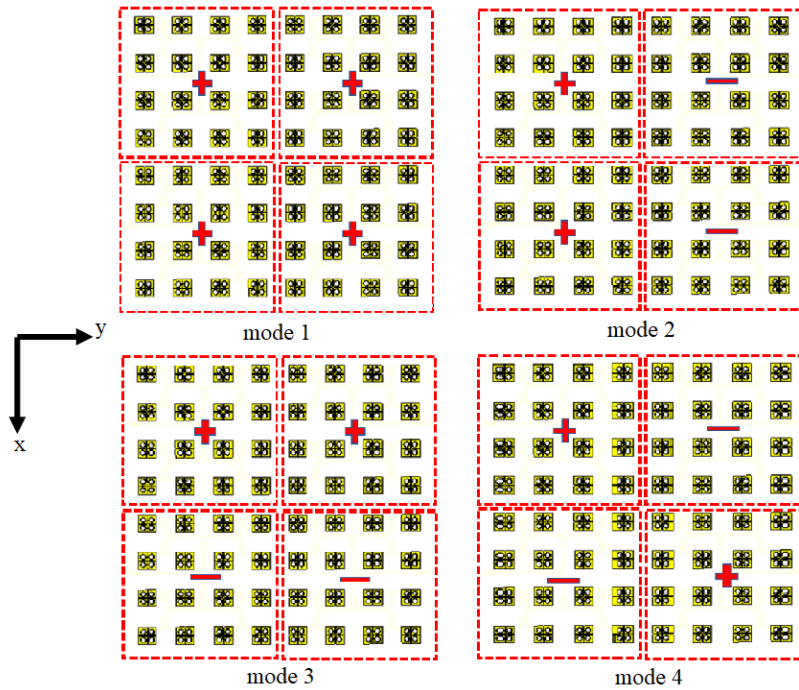


Figure 6.36. Operating mechanism of the 8x8 monopulse array antenna.

The simulated radiation patterns for the Sum (Σ), E-plane (ΔE), and H-plane (ΔH) are shown in Fig 6.36-6.38 at different frequencies 57, 60, and 64 GHz; the antenna array has good radiation pattern characteristics, includes low SLL and null in the difference pattern is around 20dB below the maximum value of the pattern of the sum input port and radiation efficiency more than 64% over the whole frequency band 57-64GHz and maximum gain for the sum port of 26.3 dB. An unbalanced pattern can be observed around the null at the higher frequency due to the phase error from the delay lines that have been used for the phase difference.

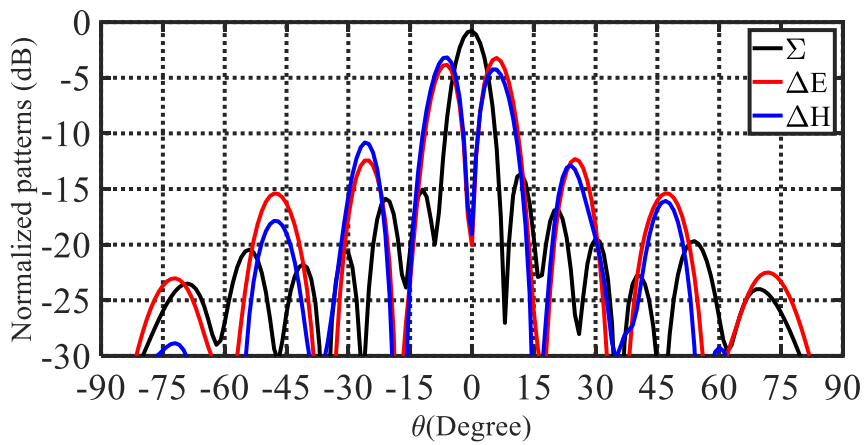


Figure 6.37. Radiation patterns of the 8×8 monopulse antenna array at 57GHz.

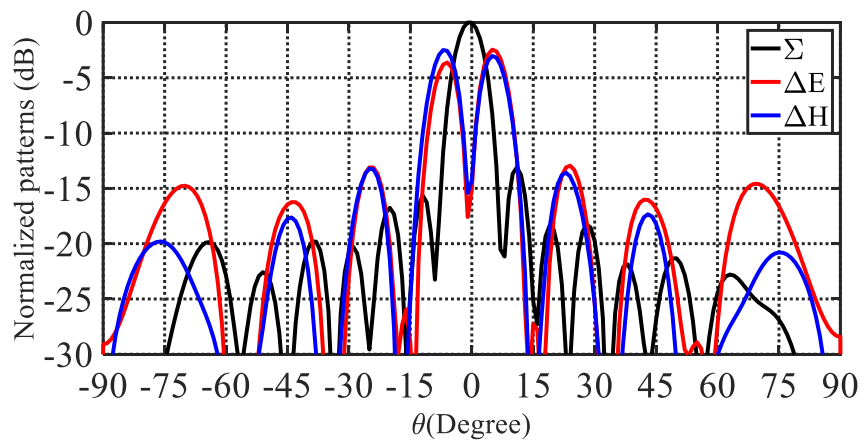


Figure 6.38. Radiation patterns of the 8×8 monopulse antenna array at 60GHz.

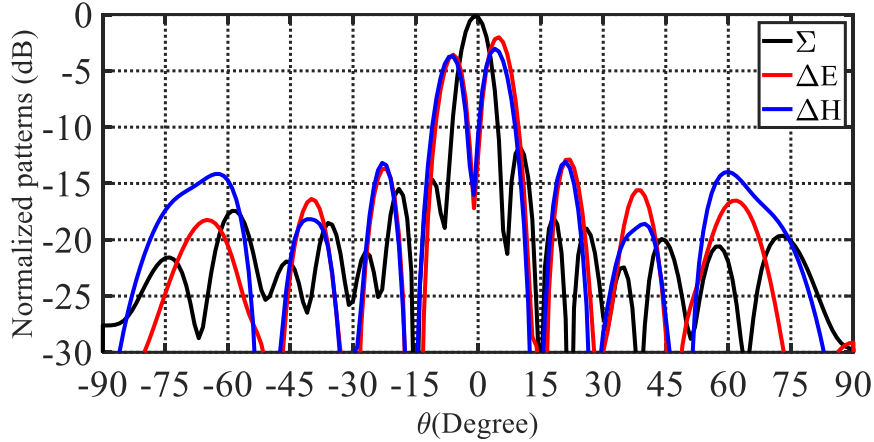


Figure 6.39. Radiation patterns of the 8×8 monopulse antenna array at 64GHz.

6.3.3 Short-range MIMO wireless system

Multiple-Input Multiple-Output (MIMO) is one of the promising solutions to satisfy the high demand for data rate through improving the channel capacity besides operating at a high-frequency band (mm-wave) [151]. Therefore, in this work, a short-range MIMO antenna system for a line of sight (LOS) is introduced at 60 GHz. The MIMO antenna system is based on the comparator, which has four modes, and each mode corresponds to a radiation pattern that provides four independent channels through pattern orthogonality [152]– [155]. These channels communicate at the same frequency in the same direction. The proposed MIMO short-range wireless system is based on two identical array antennas, as shown in Fig. 6.39. These antenna arrays are fed by a comparator that provides four modes. Each mode communicates directly with the same mode in the other antenna system.

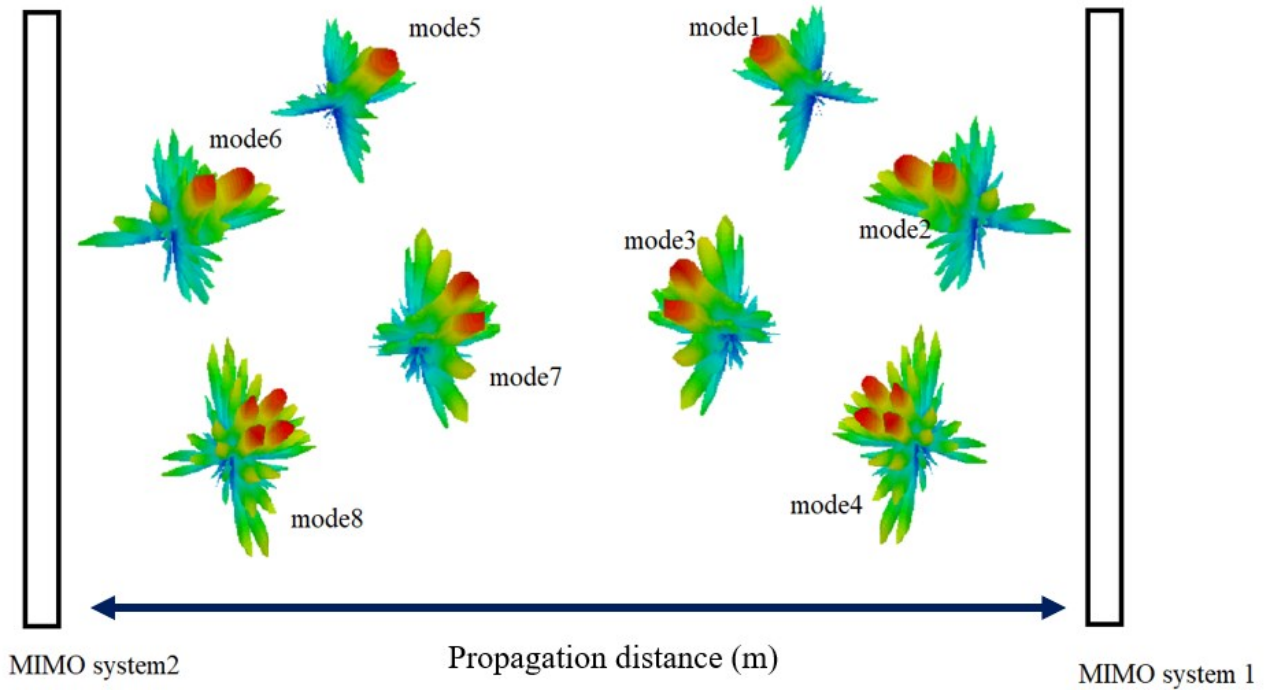


Figure 6.40. MIMO system based on 8×8 antenna and monopulse.

Although the radiating modes have the same polarization, the decorrelation between them is holding because of the hybrid coupler used in the comparator. The amount of the transmitted signal between the same mode (coupling) depends on the distance between the two antenna systems. The coupling at a short distance (up to 20 cm) is efficient; however, at a far distance (> 60 cm), The coupling between the modes deteriorates as illustrated in Fig 6.40. It is worth pointing out that we consider the direct coupling between the same modes, the coupling between the different modes (isolation) is below -20 dB for all modes, and the high isolation is mainly because of the orthogonality between these modes.

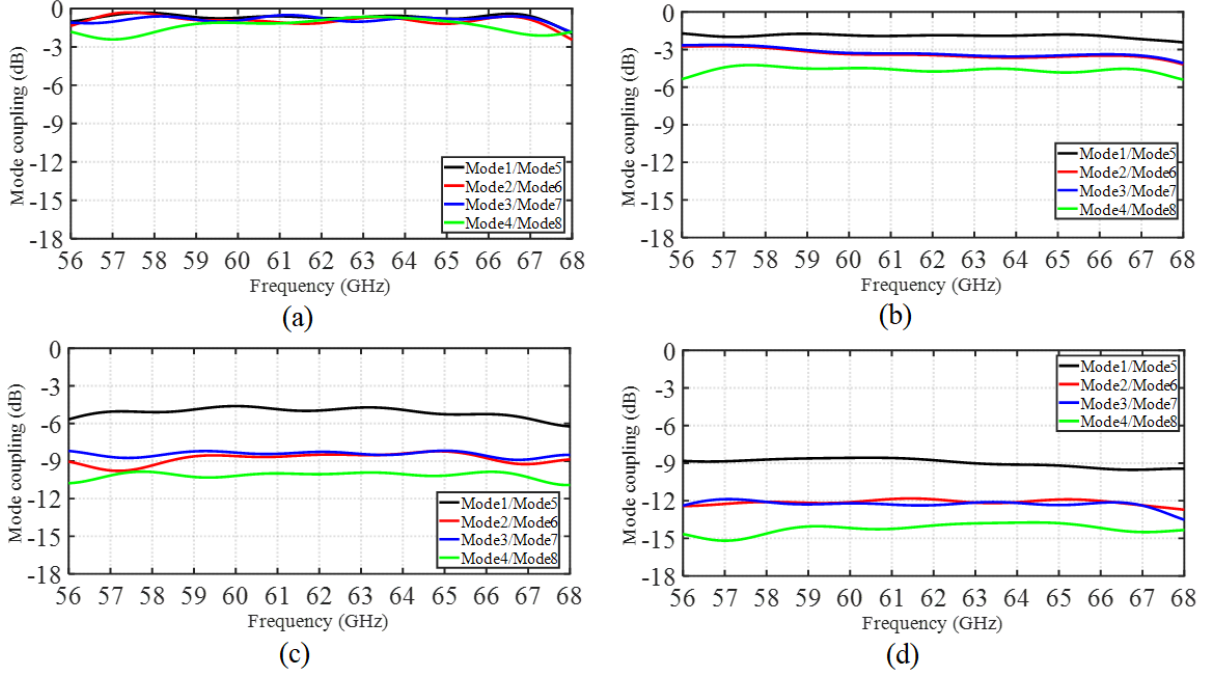


Figure 6.41. Mode coupling between two MIMO system at: (a) 8 cm, (b) 20 cm, (c) 38 cm, and (d) 60 cm.

6.3.4 Channel capacity of monopulse antenna array system

The four radiated modes can form four independent channels that can provide good diversity and increase the channel capacity for MIMO applications. The channel capacity of the system is the summation of the channel capacity of each independent mode that can be express as such

$$C_{MIMO} = \sum_{i=1}^4 \log_2(1 + SNR|S_{(4+i)i}|^2) \quad (6.1)$$

where SNR is the signal (transmitted power) to the noise at distance d from the transmitter and $S_{(4+i)i}$ is the coupling coefficient for mode i between Tx and Rx antennas. The channel capacity is normalized with respect to the capacity of mode (1) sine it has the highest coupling coefficient over the distance.

$$Normalized C_{MIMO} = \frac{\sum_{i=1}^4 \log_2(1 + SNR|S_{(4+i)i}|^2)}{\log_2(1 + SNR|S_{51}|^2)} \quad (6.2)$$

The normalized channel capacity over a distance d between the two antenna systems is shown in Fig. 6.41 with an SNR equals to 30 dB for mode (1). The normalized channel capacity of the MIMO system is up to four times the capacity of mode (1) for short distances, which indicate that all the modes participate in the whole channel capacity, but as the distance increase, the contribution of the mode becomes weak till

reaching the unity which shows the contribution of mode (1) only. Also, the system has a channel capacity of 3.5 times the channel capacity of mode (1) with propagation distance up to 35 cm.

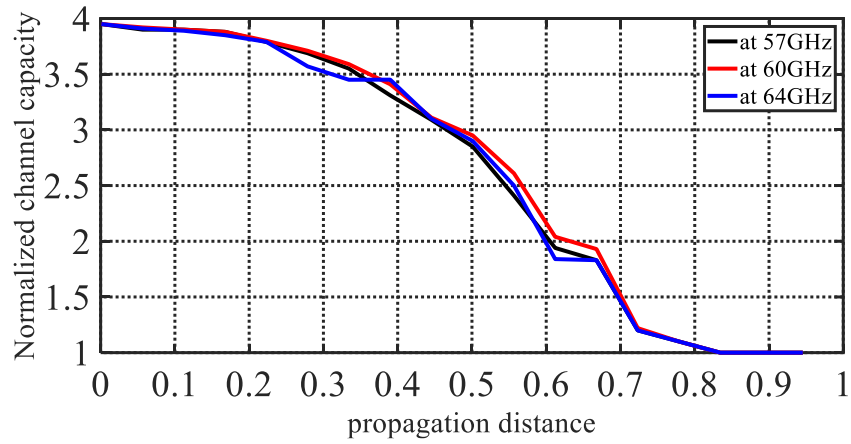


Figure 6.42. Channel capacity of a monopulse MIMO system.

Chapter 7: CONCLUSIONS AND FUTURE WORK

7.1 Conclusions:

MRGW has been used to overcome the drawback of the other guiding structures. MRGW provides good performance, but the fabrication is costly, especially at 60 GHz, because it requires more accurate dimensions for the bed of nails as well as for the mushrooms. In terms of cost, using the bed of nails is more costly compared to the cost of the mushroom bed. However, using the bed of nails provides better performance. Also, in the case of differential feeding of the antenna array, the waveguide transition is suited for the input port as it provides perfect differential feeding with the operating band.

Several contributions have been presented. In Chapter 3, an empirical expression has been developed to analyze and design the MRGW for the propagating quasi-TEM mode [84],[156]. The MRGW support of the quasi-TEM mode has been imposed by the AMC. These empirical expressions have been generalized to be used in the case of the air-filled or dielectric-filled gap. The estimation of the characteristic impedance and the effective dielectric constant has shown good agreement with the full-wave analysis. Unlike the microstrip line, it has been observed that the MRGW has less dispersive behavior within the stopband. Moreover, in Chapter 4: a simple and efficient method has been introduced to predict the performance of large finite arrays using a smaller array that has the same lattice and spacing between the elements of the large array [157], [158].

Moreover, several contributions are presented in Chapter 4. First, the large antenna array method has been presented to predict the performance of a large finite array from a small array over a wide bandwidth. The radiation characteristics of the large array, as well as the effective impedance (active impedance), have been predicted for the whole array elements without a need for the full-wave analysis within the whole frequency band and ability to analyze elements failure in the antenna array system [159]. Then, the frequency dependent effective impedances have been used as terminations to design a corporate feeding network without a need to use the actual radiating elements. To layout the feeding line in a way that keeps the feeding network lines at proper distances between each other to reduce their direct interaction, three different 3-port MRGW power dividers are designed differently from the traditional T-power divider. In addition, a rectangular waveguide transition to the two output MRGW lines has been designed to provide a differential output phase power division. Finally, an efficient design procedure of the large finite array feeding network has been introduced. The procedure is applicable to any feeding network technology. The procedure has been applied to a microstrip ridge gap waveguide (MRGW) to design an 8×8 and 16×16

antenna arrays of ME-dipole elements excited by narrow slots to cover the bandwidth of 57–64 GHz. The benefit of using this technique in designing a large finite array has tremendously reduced the design time using a moderate computing resource. In addition, optimization has only been performed on the feeding network design. In addition, to reducing the optimization parameters, the optimization has been made of several levels of the feeding network to reduce the optimization parameters to those needed for a 2×2 cooperate feeding network. Thus, the use of the commercial full-wave simulation tools, such as CST and HFSS, in designing large array becomes more efficient and faster.

Chapter 5 has presented a design of an 8×8 circularly-polarized antenna array [160]. Optimization has been used to achieve a wide bandwidth performance. The design is compact with a single-layered corporate feeding network, and all elements have been directly excited to eliminate the grating lobes and increase the view range if used in scanning application, unlike those designs that used subarray as elements of the array that supports grating lobes and limited possible scanning view range.

In Chapter 6, we have provided an 8×8 high gain antenna arrays without a backing cavity in the 60 GHz band with a good radiation pattern. The feed network has been designed using MRGW, which adds flexibility and compactness to the design structure. Then, we have introduced a high gain wideband 4×4 MIMO antenna system to operate in the 60 GHz band [161]. The MIMO antenna system consists of four subarrays of 8×8 elements, and each works independently. The 4×4 MIMO antenna system has been designed for indoor applications that can be used and integrated easily with the other components at the physical layer for 5G WIFI devices. Lastly, a low-cost, high-efficient, and less complicated antenna array has been designed using MRGW based on the superstrate layer to increase the gain. Although the spacing between the elements is larger than a free-space wavelength, the grating lobe level is substantially reduced, and excellent radiation characteristics have been achieved within the whole operating frequency band. Moreover, a monopulse antenna array is presented based on the hybrid coupler and delay lines [162], and the MIMO antenna system based on the monopulse is introduced with promising results to operate for high data rate short-range wireless systems [163].

7.2 Future Work:

The antenna array design, active/passive components, and integration between these components in a unique module with good isolation and packaging at the same time are challenging, especially at

millimeter-wave frequency ranges. MRGW is a low loss technology and provides a high-performance and flexible design that has massive potential to realize this integration and to overcome the limitations of the traditional technologies. In Chapter 3, we have introduced empirical design expressions for MRGW that will enable to design and analysis of components at millimeter-wave frequency bands and will open up the way to investigate, design, and explore more structures, filters, and other components effortlessly beside integration of active components into MRGW.

Moreover, in Chapter 4, we investigated and verified the concept of designing the antenna arrays using the effective input impedance as a load instead of using the physical radiating element that can facilitate the optimization process by considering the effect of the mutual coupling between the adjacent components. This concept could unlock the research path to study and design antenna array systems, including the tapering antenna array, to control the SLL since this technique allows controlling the power injected into each element. However, it is worth emphasizing that MRGW can be lossy for designing a large antenna array with mushroom AMC instead of a bed of nails. Besides, as a further step, the mechanical tolerances can be critical at millimeter-wave frequencies; for this reason, the empirical expressions can be used for more investigation.

References

- [1] https://www.ericsson.com/assets/local/mobility-report/documents/2018/ericsson_mobility-report-June-2018.pdf
- [2] P. Zhouyue and F. Khan, "An introduction to millimeter-wave mobile broadband systems," *IEEE Communications Magazine*, vol. 49, no. 6, pp. 101–107, 2011.
- [3] Zhouyue Pi, Junil Choi, and Robert Heath Jr., "Millimeter-Wave Gigabit Broadband Evolution toward 5G: Fixed Access and Backhaul," *IEEE Communications Magazine*, pp. 138–144, April 2016.
- [4] C. J. Hansen, "WiGig: Multi-gigabit wireless communications in the 60 GHz band," *IEEE Wireless Communications*, vol. 18, no. 6, pp. 6–7, 2011.
- [5] WiGig specification. <http://wirelessgigabitalliance.org>.
- [6] J. Wenger, "Short-range radar - being on the market," in *European Radar Conference*, EuRAD, pp. 255–258, 2007.
- [7] K.-C. Huang and Z. Wang, *Millimeter Wave Communication Systems*. Wiley, 2011.
- [8] P.-S. Kildal, A. U. Zaman, E. Rajo-Iglesias, E. Alfonso, and A. V. Nogueira, "Design and experimental verification of ridge gap waveguide in bed of nails for parallel plate mode suppression," *IET Microwaves Antennas Propag.*, vol. 5, no. 3, pp. 262–270, March 2011.
- [9] E. Rajo-Iglesias and P.-S. Kildal, "Numerical studies of bandwidth of parallel plate cut-off realized by bed of nails, corrugations and mushroom-type EBG for use in gap waveguides," *IET Microwaves Antennas Propag.*, vol. 5, no. 3, pp. 282–289, March 2011.
- [10] I. J. Bahl and D. K. Trivedi, "A designer's guide to microstrip line," *Microwaves*, vol. 16, pp. 174–182, May 1977.
- [11] P.-S. Kildal, "Three metamaterial-based gap waveguides between parallel metal plates for mm/submm waves," in *Proc. 3rd Eur. Conf. Antennas Propag. (EuCAP 2009)*, pp. 28–32, 2009.
- [12] E. Rajo-Iglesias, A. U. Zaman, and P.-S. Kildal, "Parallel plate cavity mode suppression in microstrip circuit packages using a lid of nails," *IEEE Microw. Wireless Compon. Lett.*, vol. 20, no. 1, pp. 31–33, Dec. 2009.
- [13] A. U. Zaman, T. Vukusic, M. Alexanderson, and P.-S. Kildal, "Gap waveguide PMC packaging for improved isolation of circuit components in high frequency microwave modules," *IEEE Trans. Compon. Packag. Manuf. Technol.*, vol. 4, no. 1, pp. 16–25, 2014.
- [14] E. Pucci, E. Rajo-Iglesias, J.-L. Vazquez-Roy, and P.-S. Kildal, "Planar dual-mode horn array with corporate-feed network in inverted microstrip gap waveguide," *IEEE Trans. Antennas Propag.*, vol. 62, no. 7, pp. 3534–3542, Jul. 2014.
- [15] E. Pucci, E. Rajo-Iglesias, and P.-S. Kildal, "New microstrip gap waveguide on mushroom-type EBG for packaging of microwave components," *IEEE Microw. Wireless Compon. Lett.*, vol. 22, no. 3, pp. 129–131, Mar. 2012.
- [16] H. Raza, J. Yang, P.-S. Kildal, and E. Alfonso, "Resemblance between gap waveguides and hollow waveguides," *IET Microw. Antennas Propag.*, vol. 7, no. 15, pp. 1221–1227, Dec. 2013.
- [17] P. S. Kildal, E. Alfonso, A. Valero-Nogueira, and E. Rajo-Iglesias, "Local metamaterial-based waveguides in gaps between parallel metal plates," *IEEE Antennas Wireless Propag. Lett.*, vol. 8, pp. 84–87, 2009.
- [18] P. S. Kildal, "Waveguides and transmission lines in gaps between parallel conducting surfaces," *Eur. Patent Appl. PCT/EP2009/057743*, 2009.

- [19] P. S. Kildal, "Artificially soft and hard surfaces in electromagnetics," *IEEE Transactions on Antennas and Propagation*, vol. 38, no. 10, pp. 1537–1544, 1990.
- [20] P. S. Kildal, "Definition of artificially soft and hard surfaces for electromagnetic waves," in *Electronics Letters*, vol. 24, no. 3, pp. 168–170, 4 Feb. 1988.
- [21] Y. Rahmat-Samii and H. Mosallaei, "Electromagnetic Band-Gap Structures: Classification, Characterization, and Applications," *11th International Conference on Antennas and Propagation (ICAP 2001)*, Manchester, UK, pp. 564, April 17–20, 2001.
- [22] F. Yang and Y. Rahmat-Samii, *Electromagnetic Band Gap Structures in Antenna Engineering*, Cambridge University Press, UK, 2008.
- [23] C.A. Balanis *Advanced Engineering Electromagnetics*, 2nd Edition, *John Wiley & Sons, Inc.*, New York 2012.
- [24] D. Sievenpiper, Z. Lijun, R. F. J. Broas, N. G. Alexopolous, and E. Yablonovitch, "High-impedance electromagnetic surfaces with a forbidden frequency band," *IEEE Transactions on Microwave Theory and Techniques*, vol. 47, no. 11, pp. 2059–2074, 1999.
- [25] E. Rajo-Iglesias and P. S. Kildal, "Numerical studies of bandwidth of parallel-plate cut-off realized by a bed of nails, corrugations and mushroom-type electromagnetic bandgap for use in gap waveguides," *IET Microwaves, Antennas & Propagation*, vol. 5, no. 3, pp. 282–289, 2011.
- [26] M. G. Silveirinha, C. A. Fernandes, and J. R. Costa, "Electromagnetic characterization of textured surfaces formed by metallic pins," *IEEE Trans. Antennas Propag.*, vol. 56, no. 2, pp. 405–415, Feb. 2008.
- [27] D. Sievenpiper, Z. Lijun, R. F. J. Broas, N. G. Alexopolous, and E. Yablonovitch, "High-impedance electromagnetic surfaces with a forbidden frequency band," *IEEE Trans. Microw. Theory Tech.*, vol. 47, no. 11, pp. 2059–2074, Nov. 1999.
- [28] S. A. Razavi, P. S. Kildal, L. Xiang, E. Alfonso Alos and H. Chen, "2x 2-Slot Element for 60-GHz Planar Array Antenna Realized on Two Doubled-Sided PCBs Using SIW Cavity and EBG-Type Soft Surface fed by Microstrip-Ridge Gap Waveguide," *IEEE Transactions on Antennas and Propag.*, vol. 62, no. 9, pp. 4564–4573, Sept. 2014.
- [29] A. Vosoogh, P.-S. Kildal, and V. Vassilev, "Wideband and high-gain corporate-fed gap waveguide slot array antenna with ETSI class II radiation pattern in V -band," *IEEE Trans. Antennas Propag.*, vol. 65, no. 4, pp. 1823–1831, Apr. 2017.
- [30] A. Vosoogh and P.-S. Kildal, "Corporate-fed planar 60-GHz slot array made of three unconnected metal layers using AMC pin surface for the gap waveguide," *IEEE Antennas Wireless Propag. Lett.* vol. 15, pp. 1935–1938, 2015.
- [31] A. Vosoogh and P.-S. Kildal, "High efficiency 2x2 cavity-backed slot sub-array for 60 GHz planar array antenna based on gap technology," in *Proc. IEEE Int. Symp. Antennas Propag. (ISAP)*, Nov. 2015, pp.1–3.
- [32] A. Vosoogh, P.-S. Kildal, and V. Vassilev, "A multi-layer gap waveguide array antenna suitable for manufactured by die-sink EDM," in *Proc. IEEE 10th Eur. Conf. Antennas Propag. (EuCAP)*, pp. 1–4, Apr. 2016.
- [33] A. Vosoogh and P.-S. Kildal, "V-band high efficiency corporate-fed 8x8 slot array antenna with ETSI class II radiation pattern based on gap technology," in *Proc. IEEE Int. Symp. Antennas Propag. (APSURSI)*, pp. 803–804, Jun./Jul. 2016.
- [34] H. Attia, M. S. Sorkherizi, and A. A. Kishk, "60 GHz slot antenna array based on ridge gap waveguide technology enhanced with dielectric superstrate," in *Proc. IEEE 9th Eur. Conf. Antennas Propag. (EuCAP)*, pp. 1–4, Apr. 2015.

- [35] S. A. Razavi, P.-S. Kildal, L. Xiang, E. A. Alòs, and H. Chen, "2×2-slot element for 60-GHz planar array antenna realized on two doubled-sided PCBs using SIW cavity and EBG-type soft surface fed by microstrip ridge gap waveguide," *IEEE Trans. Antennas Propag.*, vol. 62, no. 9, pp. 4564–4573, Sep. 2014.
- [36] A. Vosoogh, A. A. Brazález, and P.-S. Kildal, "A V-band inverted microstrip gap waveguide end-coupled bandpass filter," *IEEE Microw. Wireless Compon. Lett.* vol. 26, no. 4, pp. 261–263, Apr. 2016.
- [37] M. S. Sorkherizi, A. Khaleghi, and P.-S. Kildal, "Direct-coupled cavity filter in ridge gap waveguide," *IEEE Trans. Compon., Packag., Manuf. Technol.*, vol. 4, no. 3, pp. 490–495, Mar. 2014.
- [38] A. Berenguer, M. Baquero-Escudero, D. Sanchez-Escuderos, B. Bernardo-Clemente, and V. E. Boria-Esbert, "Low insertion loss 61 GHz narrow-band filter implemented with groove gap waveguides," in *Proc. IEEE 44th Eur. Microw. Conf. (EuMC)*, pp. 191–194, Oct. 2014.
- [39] E. A. Alòs, A. U. Zaman, and P.-S. Kildal, "Ka-band gap waveguide coupled-resonator filter for radio link diplexer application," *IEEE Trans. Compon., Packag., Manuf. Technol.*, vol. 3, no. 5, pp. 870–879, May 2013.
- [40] M. S. Sorkherizi and A. A. Kishk, "Fully printed gap waveguide with facilitated design properties," *IEEE Microw. Wireless Compon. Lett.* vol. 26, no. 9, pp. 657–659, Sep. 2016.
- [41] M. Rezaee, A. U. Zaman, and P.-S. Kildal, "A groove gap waveguide iris filter for V-band application," in *Proc. IEEE 23rd Iranian Conf. Electr. Eng.*, May 2015, pp. 462–465.
- [42] M. S. Sorkherizi and A. A. Kishk, "Completely tuned coupled cavity filters in defected bed of nails cavity," *IEEE Trans. Compon., Packag., Manuf. Technol.*, vol. 6, no. 12, pp. 1865–1872, Dec. 2016.
- [43] A. Vosoogh, M. S. Sorkherizi, A. U. Zaman, J. Yang, and A. A. Kishk, "An integrated Ka-band diplexer-antenna array module based on gap waveguide technology with simple mechanical assembly and no electrical contact requirements," *IEEE Trans. Microw. Theory Techn.*, vol. 66, no. 2, pp. 962–972, Feb. 2017.
- [44] M. Rezaee, A. U. Zaman, and P.-S. Kildal, "V-band groove gap waveguide diplexer," in *Proc. IEEE 9th Eur. Conf. Antennas Propag. (EuCAP)*, pp. 1–4, Apr. 2015.
- [45] A. Vosoogh, M. S. Sorkherizi, A. U. Zaman, J. Yang, and A. A. Kishk, "An E-band antenna-diplexer compact integrated solution based on gap waveguide technology," in *Proc. IEEE Int. Symp. Antennas Propag. (ISAP)*, pp. 1–2, Oct./Nov. 2017.
- [46] A. Vosoogh, M. S. Sorkherizi, A. U. Zaman, J. Yang, and A. A. Kishk, "Diplexer integration into a Ka-band high-gain gap waveguide corporate fed slot array antenna," in *Proc. IEEE Int. Symp. Antennas Propag. USNC/URSI Nat. Radio Sci. Meeting*, pp. 2667–2668, Jul. 2017.
- [47] H. Raza, J. Yang, P.-S. Kildal, and E. Alfonso Alos, "Microstrip-ridge gap waveguide; Study of losses, bends, and transition to WR-15," *IEEE Trans. Microw. Theory Techn.*, vol. 62, no. 9, pp. 1943–1952, Sep. 2014.
- [48] M. S. Sorkherizi and A. A. Kishk, "Low loss planar bandpass filters for millimeter-wave application," in *Proc. IEEE MTT-S Int. Dig.*, pp. 1–4, 2015.
- [49] E. Pucci, E. Rajo-Iglesias, and P.-S. Kildal, "New microstrip gap waveguide on mushroom-type EBG for packaging of microwave components," *IEEE Microw. Wireless Compon. Lett.* vol. 22, no. 3, pp. 129–131, Mar. 2012.
- [50] E. Rajo-Iglesias, A. U. Zaman, and P.-S. Kildal, "Parallel plate cavity mode suppression in microstrip circuit packages using a lid of nails," *Microwave and Wireless Components Lett.* vol. 20, no. 1, pp. 31–33, 2010.

- [51] Ahmed Kishk, Ashraf Uz Zaman, and Per-Simon Kildal, "Numerical Prepackaging with PMC lid – Efficient and Simple Design Procedure for Microstrip Circuits including the Packaging," *ACES Journal*, vol. 27, No. 5, pp. 389–398, May 2012.
- [52] Jing Zhang, Xiupu Zhang, Dongya Shen, Ahmed A. Kishk, "Packaged Microstrip Line: A New Quasi-TEM Line for Microwave and Millimeter Wave Applications," *IEEE Trans. Microw. Theory Tech.*, vol. 65, No. 3, pp. 707 – 719, March 2017.
- [53] Jing Zhang, Xiupu Zhang, Dongya Shen, Ahmed A Kishk, " A Novel SelfJ Packaged Microstrip Line," in *Proc. 32nd URSI General Assembly and Scientific Symposium*, Montreal, August 2017.
- [54] J. Zhang, X. Zhang, D. Shen, and A. A. Kishk, "Design of packaged microstrip line," in *Proc. IEEE Int. Conf. Microw. Millim. -Wave Techn. (ICMMT)*, Beijing, China, pp. 82–84, Jun. 2016.
- [55] Milad Sharifi Sorkherizi, and Ahmed A. Kishk, "Self-Packaged, LowM Loss, Planar Bandpass Filters for Millimeter-Wave Application Based on Printed Gap Waveguide Technology," *IEEE Transactions on Components, Packaging and Manufacturing Technology*, vol. 7, Issue: 9, pp. 1419–1431, Sept. 2017.
- [56] Hamburg, Germany, pp 268-72. 6. E. Hammerstad and O. Jensen, "Accurate Models for Microstrip Computer-Aided Design," *IEEE MTT-S International Symposium Digest*, Washington D.C. IEEE catalog #80CH1545-3MTT, pp 407–409, May 1980.
- [57] H. A. Wheeler, "Transmission-Line Properties of a Strip on a Dielectric Sheet on a Plane," *IEEE Transactions on Microwave Theory and Techniques*, vol. 25, no. 8, pp. 631–647, Aug 1977.
- [58] M. A. R. Gunston and J. R. Weale, "Variation of microstrip impedance with strip thickness," *Electron. Lett.*, vol. 5, pp. 697–698, Dec. 27, 1969.
- [59] M. A. R. Gunston and J. R. Weale, "The transmission characteristics of microstrip," *The Marconi Rev.*, vol. 32, pp. 226–243, Oct.–Dec. 1969.
- [60] I. J. Bahl and R. Garg, "Simple and accurate formulas for a microstrip with finite strip thickness," *Proceedings of the IEEE.*, vol. 65, no. 11, pp. 1611–1612, Nov. 1977
- [61] N. Bayat-Makou and A. A. Kishk, "Accurate Models for Microstrip Gap Waveguide Horn Antenna," *IEEE Transactions on Antennas and Propag.*, vol. 65, no. 12, pp. 6847–6855, Dec. 2017.
- [62] R. E. Collin, *Foundations for Microwave Engineering*, 2nd ED. New York, NY, USA: McGraw-Hill, 1992.
- [63] A. A. Brazãa, lez, E. Rajo-Iglesias, J. L. Vazquez-Roy, A. Vosoogh, and P. S. Kildal, "Design and Validation of Microstrip Gap Waveguides and Their Transitions to Rectangular Waveguide, for Millimeter-Wave Applications," *IEEE Transactions on Microwave Theory and Techniques*, vol. 63, no. 12, pp. 4035–4050, Dec. 2015.
- [64] M. Sharifi Sorkherizi, A. Dadgarpour, and A. A. Kishk, "Planar High efficiency Antenna Array Using New Printed Ridge Gap Waveguide Technology," *IEEE Transactions on Antennas and Propag.*, vol. 65, no. 7, pp. 3772–3776, July 2017.
- [65] S. Yong and C. Chong, "An overview of multi gigabit wireless through millimeter wave technology: potentials and technical challenges," *EURASIP J. Wireless Commun. Netw.*, vol. 2007, no. 1, pp. 50–50, 2007.
- [66] Ahmed A. Kishk, "Design of Large Finite Arrays Using Simulations or Measurements of Small Arrays," *Forum for Electromagnetic Research Methods and Application Technologies (FERMAT)*, vol.14, July-August 2014.
- [67] Ahmed A. Kishk, " Prediction of Large Array Characteristics from Small Array Parameters," *2nd European Conference on Antennas and Propagation (EuCAP 2007)* Edinburgh, UK, pp. 584-588, Nov. 2007.

- [68] C. Balanis, “*Antenna Theory: Analysis and Design*,” Wiley, 3rd Edition. 2005.
- [69] F. Capolino, M. Albani, S. Maci, and L. B. Felsen, “Frequency-domain green’s function for a planar periodic semi-infinite phased array - part I: Truncated Floquet wave formulation,” *IEEE Transactions on Antennas and Propagation*, vol.48, no. 1, pp. 67–74, January 2000.
- [70] A. Polemi, A. Toccafondi, and S. Maci, “High-frequency green’s function for a semi-infinite array of electric dipoles on a grounded slab - part I: Formulation,” *IEEE Transactions on Antennas and Propagation*, vol. 49, no. 12, pp.1667-1677, December 2001.
- [71] A. Cucini, M. Albani, and S. Maci, “Truncated Floquet wave full-wave analysis of large phased arrays of open ended waveguides with a nonuniform amplitude excitation,” *IEEE Transactions on Antennas and Propagation*, vol. 51, no. 6, pp.1386-1394, June 2003.
- [72] C. Craeye, A. B. Smolders, D. H. Schaubert, and A. G. Tijhuis, “An efficient computation scheme for the free space Green's function of a two-dimensional semi-infinite phased array,” *IEEE Transactions on Antennas and Propagation*, vol. 51, no. 4, pp. 766–771, April 2003.
- [73] A. K. Skrivervik and J. R. Mosig, “Finite phased array of microstrip patch antennas: The infinite array approach,” *IEEE Transactions on Antennas and Propagation*, vol. 40, no. 5, pp. 579–582, (1992).
- [74] C. Craeye, A. G. Tijhuis, and D. H. Schaubert, “An efficient mom formulation for finite by-infinite arrays of two-dimensional antennas arranged in a three-dimensional structure,” *IEEE Transactions on Antennas and Propagation*, volume 52, no. 1, pp. 271–281, 2004.
- [75] R. W. Kindt, K. Sertel, E. Topsakal, and J. L. Volakis, “Array decomposition method for the accurate analysis of finite arrays,” *IEEE Transactions on Antennas and Propagation*, volume 51, no. 6, pp. 1364–1372, 2003.
- [76] B. Lesur et al., “A Large Antenna Array for Ka-Band Satcom-on-the-Move Applications—Accurate Modeling and Experimental Characterization,” *IEEE Transactions on Antennas and Propagation*, vol. 66, no. 9, pp. 4586-4595, Sept. 2018.
- [77] D. Zarifi, A. Farahbakhsh, A. U. Zaman and P. S. Kildal, “Design and Fabrication of a High-Gain 60-GHz Corrugated Slot Antenna Array with Ridge Gap Waveguide Distribution Layer,” *IEEE Transactions on Antennas and Propagation*, vol. 64, no. 7, pp. 2905-2913, July 2016.
- [78] A. Farahbakhsh, D. Zarifi, and A. U. Zaman, “A mmWave Wideband Slot Array Antenna Based on Ridge Gap Waveguide With 30% Bandwidth,” *IEEE Transactions on Antennas and Propagation*, vol. 66, no. 2, pp. 1008-1013, Feb. 2018.
- [79] Y. Li and K. M. Luk, “60-GHz Substrate Integrated Waveguide Fed Cavity-Backed Aperture-Coupled Microstrip Patch Antenna Arrays,” *IEEE Transactions on Antennas and Propagation*, vol. 63, no. 3, pp. 1075-1085, March 2015.
- [80] Y. Li and K. Luk, “A 60-GHz Wideband Circularly Polarized Aperture-Coupled Magneto-Electric Dipole Antenna Array,” *IEEE Transactions on Antennas and Propagation*, vol. 64, no. 4, pp. 1325-1333, April 2016.
- [81] S. A. Razavi, P. S. Kildal, L. Xiang, E. Alfonso Alós, and H. Chen, “2x2-Slot Element for 60-GHz Planar Array Antenna Realized on Two Doubled-Sided PCBs Using SIW Cavity and EBG-Type Soft Surface fed by Microstrip-Ridge Gap Waveguide,” *IEEE Transactions on Antennas and Propagation*, vol. 62, no. 9, pp. 4564-4573, Sept. 2014.
- [82] Y. Li and K. M. Luk, “60-GHz Dual-Polarized Two-Dimensional Switch-Beam Wideband Antenna Array of Aperture-Coupled Magneto-Electric Dipoles,” *IEEE Transactions on Antennas and Propagation*, vol. 64, no. 2, pp. 554-563, Feb. 2016.

- [83] K. M. Luk and H. Wong, "A new wideband unidirectional antenna element," *Int. J. Microw. Opt. Technol.*, vol. 1, no. 1, pp. 35–44, Jun. 2006.
- [84] A. T. Hassan, M. A. Moharram Hassan, and A. A. Kishk, "Modeling and Design Empirical Formulas of Microstrip Ridge Gap Waveguide," *IEEE Access*, vol. 6, pp. 51002-51010, Sept. 2018.
- [85] A. A. Brazález, E. Rajo-Iglesias, J. L. Vázquez-Roy, A. Vosoogh, and P. Kildal, "Design and Validation of Microstrip Gap Waveguides and Their Transitions to Rectangular Waveguide, for Millimeter-Wave Applications," *IEEE Transactions on Microwave Theory and Techniques*, vol. 63, no. 12, pp. 4035-4050, Dec. 2015.
- [86] J. Wu, Y. J. Cheng, and Y. Fan, "A wideband high-gain high efficiency hybrid integrated plate array antenna for V-band inter-satellite links," *IEEE Trans. Antennas Propag.*, vol. 63, no. 4, pp. 1225–1233, Apr. 2015
- [87] Y. Miura, J. Hirokawa, M. Ando, Y. Shibuya, and G. Yoshida, "Double-layer full-corporate-feed hollow-waveguide slot array antenna in the 60-GHz band," *IEEE Trans. Antennas Propag.*, vol. 59, no. 8, pp. 2844–2851, Aug. 2011.
- [88] Y. Li and K.-M. Luk, "Low-cost high-gain and broadband substrate integrated-waveguide-fed patch antenna array for 60-GHz band," *IEEE Trans. Antennas Propag.*, vol. 62, no. 11, pp. 5531–5538, Nov. 2014.
- [89] J. Liu, A. Vosoogh, A. U. Zaman and J. Yang, "A Slot Array Antenna with Single-Layered Corporate-Feed Based on Ridge Gap Waveguide in the 60 GHz Band," *IEEE Transactions on Antennas and Propagation*, vol. 67, no. 3, pp. 1650-1658, March 2019.
- [90] D. Zarifi, A. Farahbakhsh, A. U. Zaman and P. S. Kildal, "Design and Fabrication of a High-Gain 60-GHz Corrugated Slot Antenna Array with Ridge Gap Waveguide Distribution Layer," *IEEE Transactions on Antennas and Propagation*, vol. 64, no. 7, pp. 2905-2913, July 2016.
- [91] M. Levitas, D. A. Horton, and T. C. Cheston, "Practical failure compensation in active phased arrays," *IEEE Transactions on Antennas and Propagation*, vol. 47, no. 3, pp. 524-535, March 1999.
- [92] T. J. Peters, "A conjugate gradient-based algorithm to minimize the sidelobe level of planar arrays with element failures," *IEEE Trans. Antennas Propag.*, vol. 39, pp. 1497-1504, Oct. 1991.
- [93] J. Simmers, H. L. Southall, and T. O'Donnell, "Advances in neural beamforming," in *Proc. '93 Antennas Appl. Symp.*, Univ. Illinois, Urbana-Champaign, pp. 206-219, Sept. 1993.
- [94] M. C. Dogan and J. Mendel, "Applications of cumulants to array processing-Part I: Aperture extension and array calibration," *IEEE Trans. Signal Processing* vol. 43, pp. 1200-1216, May 1995.
- [95] T. S. Rappaport, Y. Xing, G. R. MacCartney, A. F. Molisch, E. Mellios, and J. Zhang, "Overview of Millimeter Wave Communications for Fifth-Generation (5G) Wireless Networks—With a Focus on Propagation Models," *IEEE Transactions on Antennas and Propagation*, vol. 65, no. 12, pp. 6213-6230, Dec. 2017.
- [96] K. Zheng et al., "10 Gb/s HetsNets with Millimeter-Wave Communications: Access and Networking — Challenges and Protocols," *IEEE Commun. Mag.*, vol. 53, no. 1, Jan. 2015, pp. 222–31.
- [97] S. Rangan, T. Rappaport, and E. Erkip, "Millimeter Wave Cellular Wireless Networks: Potentials and Challenges," *Proc. IEEE*, vol. 102, no. 3, pp. 366–85, Mar. 2014.
- [98] T. Mannabe et al., "Polarization dependence of multipath propagation and high-speed transmission channel characteristics of indoor millimeter wave channel at 60 GHz," *IEEE Trans. Veh. Technol.*, vol. 44, no. 2, pp. 268–274, May 1995.
- [99] H. C. Sun, Y. X. Guo, and Z. L. Wang, "60-GHz circularly polarized U-slot patch antenna array on LTCC," *IEEE Trans. Antennas Propag.*, vol. 61, no. 1, pp. 430–435, Jan. 2013.

- [100] M. J. Li and K. M. Luk, "Low-cost wideband microstrip antenna array for 60-GHz applications," *IEEE Trans. Antennas Propag.*, vol. 62, no. 6, pp. 3012–3018, Jun. 2014.
- [101] Y. Miura, J. Hirokawa, M. Ando, K. Igarashi, and G. Yoshida, "A circularly-polarized aperture array antenna with a corporate-feed hollow waveguide circuit in the 60 GHz-band," in *Proc. IEEE Int. Symp. Antennas Propag. (AP-S)*, Session: 429.2, Jul. 2011, pp. 3029–3032.
- [102] A. B. Guntupalli and K. Wu, "60-GHz circularly polarized antenna array made in low-cost fabrication process," *IEEE Antennas Wireless Propag. Lett.*, vol. 13, pp. 864–867, May 2014.
- [103] Y. Sun and K. W. Leung, "Circularly Polarized Substrate-Integrated Cylindrical Dielectric Resonator Antenna Array for 60 GHz Applications," *IEEE Antennas and Wireless Propagation Letters*, vol. 17, no. 8, pp. 1401–1405, Aug. 2018.
- [104] Y. Miura, J. Hirokawa, M. Ando, Y. Shibuya, and G. Yoshida, "Double-layer full-corporate-feed hollow-waveguide slot array antenna in the 60-GHz band," *IEEE Trans. Antennas Propag.*, vol. 59, no. 8, pp. 2844–2851, Aug. 2011.
- [105] Y. Li and K.-M. Luk, "Low-cost high-gain and broadband substrate integrated-waveguide-fed patch antenna array for 60-GHz band," *IEEE Trans. Antennas Propag.*, vol. 62, no. 11, pp. 5531–5538, Nov. 2014.
- [106] J. Liu, A. Vosoogh, A. U. Zaman and P.-S. Kildal, "Design of a cavity backed slot array unit cell on inverted microstrip gap waveguide," in *Proc. Int. Symp. Antennas Propag. (ISAP)*, Nov. 2015, pp. 1–4.
- [107] J. Liu, A. Vosoogh, A. U. Zaman and P.-S. Kildal, "Design of 8×8 slot array antenna based on inverted microstrip gap waveguide," in *Proc. Int. Symp. Antennas Propag. (ISAP)*, Oct. 2016, pp. 760–761.
- [108] J. Liu, A. Vosoogh, A. U. Zaman, and J. Yang, "Design and fabrication of a high-gain 60-GHz cavity-backed slot antenna array fed by inverted microstrip gap waveguide," *IEEE Trans. Antennas Propag.*, vol. 65, no. 4, pp. 2117–2122, Apr. 2017.
- [109] A. Farahbakhsh, D. Zarifi, and A. U. Zaman, "60-GHz groove gap waveguide based wideband H-plane power dividers and transitions: For use in high-gain slot array antenna," *IEEE Trans. Microw. Theory Techn.*, vol. 65, no. 11, pp. 4111–4121, Nov. 2017.
- [110] J. Rodriguez, *Fundamentals of 5G Mobile Networks*. Hoboken, NJ, USA: Wiley, 2015.
- [111] T. S. Rappaport, Y. Xing, G. R. MacCartney, A. F. Molisch, E. Mellios, and J. Zhang, "Overview of Millimeter Wave Communications for Fifth-Generation (5G) Wireless Networks—With a Focus on Propagation Models," *IEEE Transactions on Antennas and Propagation*, vol. 65, no. 12, pp. 6213–6230, Dec. 2017.
- [112] B. Ai et al., "Challenges toward wireless communications for high-speed railway," *IEEE Trans. Intell. Transp. Syst.*, vol. 15, no. 5, pp. 2143–2158, Oct. 2014.
- [113] A. Lee Swindlehurst, Ender Ayanoglu, Payam Heydari, and Filippo Capolino "Millimeter-Wave Massive MIMO: The Next Wireless Revolution?" *IEEE Communications Magazine*, pp. 52–62, September 2014.
- [114] F. Boccardi, R. W. Heath, A. Lozano, T. L. Marzetta, and P. Popovski, "Five disruptive technology directions for 5G," *IEEE Commun. Mag.*, vol. 52, no. 2, pp. 74–80, Feb. 2014.
- [115] C.-X. Wang et al., "Cellular architecture and key technologies for 5G wireless communication networks," *IEEE Commun. Mag.*, vol. 52, no. 2, pp. 122–130, Feb. 2014.
- [116] E. G. Larsson, O. Edfors, F. Tufvesson, and T. L. Marzetta, "Massive MIMO for Next Generation Wireless Systems," *IEEE Commun. Mag.*, vol. 52, no. 2, pp. 186–195, Feb. 2014.

- [117] J. G. Andrews et al., "What will 5G be?" *IEEE J. Sel. Areas Commun.*, vol. 32, no. 6, pp. 1065–1082, Jun. 2014.
- [118] T. S. Rappaport et al., "Millimeter Wave Mobile Communications for 5G Cellular: It will work!" *IEEE Access*, vol. 1, pp. 335–349, May 2013.
- [119] W. Roh et al., "Millimeter-wave beamforming as an enabling technology for 5G cellular communications: Theoretical feasibility and prototype results," *IEEE Commun. Mag.*, vol. 52, no. 2, pp. 106–113, Feb. 2014.
- [120] M. R. Akdeniz et al., "Millimeter-wave channel modeling and cellular capacity evaluation," *IEEE J. Sel. Areas Commun.*, vol. 32, no. 6, pp. 1164–1179, Jun. 2014.
- [121] N. Al-Falahy and O. Y. Alani, "Technologies for 5G Networks: Challenges and Opportunities," *IT Professional*, vol. 19, no. 1, pp. 12-20, Jan. -Feb. 2017.
- [122] T. Yamada, T. Nishio, M. Morikura, and K. Yamamoto, "Experimental evaluation of IEEE 802.11ad millimeter-wave WLAN devices," *Proc. 21st Asia-Pacific Conf. Commun. (APCC)*, pp. 278–282 Oct. 2015.
- [123] A. Siligaris et al., "A 65-nm CMOS fully integrated transceiver module for 60-GHz wireless HD applications," *IEEE J. Solid-State Circuits*, vol. 46, no. 12, pp. 3005–3017, Dec. 2011.
- [124] K. Chandra, A. Doff, Z. Cao, R. V. Prasad, and I. Niemegeers, "60 GHz MAC standardization: Progress and way forward," *2015 12th Annual IEEE Consumer Communications and Networking Conference (CCNC)*, Las Vegas, NV, pp. 182-187, 2015.
- [125] A. Maltsev, A. Pudeyev, A. Lomayev, and I. Bolotin, "Channel modeling in the next generation mmWave Wi-Fi: IEEE 802.11ay standard," *Proc. 22nd Eur. Wireless Conf. Eur. Wireless*, pp. 1–8, May 2016.
- [126] M. Cudak, T. Kovarik, T. A. Thomas, A. Ghosh, Y. Kishiyama and T. Nakamura, "Experimental mm wave 5G cellular system," *2014 IEEE Globecom Workshops (GC Wkshps)*, Austin, TX, pp. 377-381, 2014.
- [127] T. Djerafi and K. Wu, "A low-cost wideband 77-GHz planar butler matrix in SIW technology," *IEEE Trans. Antennas Propag.*, vol. 60, no. 10, pp. 4949–4954, Oct. 2012.
- [128] C. Tseng, C. Chen, and T. Chu, "A low-cost 60-GHz switched-beam patch antenna array with butler matrix network," *IEEE Antennas Wireless Propag. Lett.*, vol. 7, pp. 432–435, Dec. 2008.
- [129] H. Chu, Y.-X. Guo, and Z. Wang, "60-GHz LTCC wideband vertical off-center dipole antenna and arrays," *IEEE Trans. Antennas Propag.*, vol. 61, no. 1, pp. 153–161, Jan. 2013.
- [130] W. Lee, J. Kim, C. Cho, and Y. Yoon, "Beamforming lens antenna on a high resistivity silicon wafer for 60 GHz WPAN," *IEEE Trans. Antennas Propag.*, vol. 58, no. 3, pp. 706–713, Mar. 2010.
- [131] T. Brown, P. Kyritsi, and E. D. Carvalho, *Practical Guide to MIMO Radio Channel: With MATLAB Examples*. John Wiley & Sons, 2012.
- [132] S. Blanch, J. Romeu, and I. Corbella, "Exact representation of antenna system diversity performance from input parameter description," *Electronics Letters*, vol. 39, no. 9, pp. 705–707, 2003.
- [133] M. S. Sharawi, *Printed MIMO Antenna Engineering*. Norwood, MA, USA: Artech House, 2014.
- [134] H. Attia, M. S. Sorkherizi, and A. A. Kishk, "60 GHz slot antenna array based on ridge gap waveguide technology enhanced with dielectric superstrate," *2015 9th European Conference on Antennas and Propagation (EuCAP)*, Lisbon, 2015, pp. 1-4.
- [135] H. Vettikalladi, O. Lafond and M. Himdi, "High-Efficient and High-Gain Superstrate Antenna for 60-GHz Indoor Communication," *IEEE Antennas and Wireless Propagation Letters*, vol. 8, pp. 1422-1425, 2009.

- [136] Y. Al-Alem and A. A. Kishk, "Antenna Gain and Bandwidth Enhancement Using a Dielectric Superstrate at 60 GHz," *2018 18th International Symposium on Antenna Technology and Applied Electromagnetics (ANTEM)*, Waterloo, ON, 2018, pp. 1-3.
- [137] H. Vettikalladi, L. Le Coq, O. Lafond, and M. Himdi, "Broadband superstrate aperture antenna for 60GHz applications," *The 40th European Microwave Conference*, Paris, 2010, pp. 687-690.
- [138] D. Abbou, R. Touhami, S. Gaoua, and T. P. Vuong, "High gain microstrip antenna based on double superstrate layer for 60GHz communication systems," *2014 International Conference on Multimedia Computing and Systems (ICMCS)*, Marrakech, 2014, pp. 1384-1387.
- [139] K. M. Luk and H. Wong, "A new wideband unidirectional antenna element," *Int. J. Microw. Opt. Technol.*, vol. 1, no. 1, pp. 35-44, Jun. 2006.
- [140] D. Jackson and N. Alexopoulos, "Gain enhancement methods for printed circuit antennas," *IEEE Trans. Antennas Propag.*, vol. 33, no. 9, pp. 976-987, Sep. 1985.
- [141] D. M. Pozar, *Microwave Engineering*, 3rd ed., Wiley 2005.
- [142] S. M. Sherman and D. K. Barton, *Monopulse Principles and Techniques*. Norwood, MA, USA: Artech House, 2011.
- [143] Hao Wang, Da-Gang Fang, and X. G. Chen, "A compact single layer monopulse microstrip antenna array," in *IEEE Transactions on Antennas and Propagation*, vol. 54, no. 2, pp. 503-509, Feb. 2006.
- [144] H. Chu, J.-X. Chen, S. Luo, and Y.-X. Guo, "A millimeter-wave filtering monopulse antenna array based on substrate integrated waveguide technology," *IEEE Trans. Antennas Propag.*, vol. 64, no. 1, pp. 316-321, Jan. 2016.
- [145] A. Vosoogh, A. Haddadi, A. U. Zaman, J. Yang, H. Zirath, and A. A. Kishk, "W -Band Low-Profile Monopulse Slot Array Antenna Based on Gap Waveguide Corporate-Feed Network," *IEEE Transactions on Antennas and Propagation*, vol. 66, no. 12, pp. 6997-7009, Dec. 2018.
- [146] A. M. Abbosh and M. E. Bialkowski, "Design of Compact Directional Couplers for UWB Applications," *IEEE Transactions on Microwave Theory and Techniques*, vol. 55, no. 2, pp. 189-194, Feb. 2007.
- [147] T. Djerafi, K. Wu and S. O. Tatu, "3 dB 90o Hybrid Quasi-Optical Coupler With Air Field Slab in SIW Technology," *IEEE Microwave and Wireless Components Letters*, vol. 24, no. 4, pp. 221-223, April 2014.
- [148] S. I. Shams and A. A. Kishk, "Design of 3-dB Hybrid Coupler Based on RGW Technology," *IEEE Transactions on Microwave Theory and Techniques*, vol. 65, no. 10, pp. 3849-3855, Oct. 2017.
- [149] A. Algaba-Brazalez and E. Rajo-Iglesias, "Design of a Butler matrix at 60GHz in inverted microstrip gap waveguide technology," *2015 IEEE International Symposium on Antennas and Propagation & USNC/URSI National Radio Science Meeting*, pp. 2125-2126, Vancouver, BC, 2015.
- [150] H.J. Riblet," A mathematical theory of Directional Coupler," *I.R.E Proc*, Vol.33, pp.1307-1313, 1947.
- [151] K. Tekkouk et al., "Corporate-feed slotted waveguide array antenna in the 350-GHz band by silicon process," *IEEE Trans. Antennas Propag.*, vol. 65, no. 1, pp. 217-225, Jan. 2017.
- [152] T. Svantesson, "Correlation and channel capacity of MIMO systems employing multimode antennas," *IEEE Trans. Veh. Technol.*, vol. 51, no. 6, pp. 1304-1312, Nov. 2002.
- [153] C. Waldschmidt and W. Wiesbeck, "Compact wide-band multimode antennas for MIMO and diversity," *IEEE Trans. Antennas Propag.*, vol. 52, no. 8, pp. 1963-1969, Aug. 2004.
- [154] A. Mukherjee and H. M. Kwon, "Compact multi-user wideband MIMO system using multiple-mode microstrip antennas," in *Proc. IEEE 65th Veh. Technol. Conf.*, Apr. 2007, pp. 584-588.

- [155] R. G. Vaughan, "Two-port higher mode circular microstrip antennas," *IEEE Trans. Antennas Propag.*, vol. AP-36, no. 3, pp. 309–321, Mar. 1988.
- [156] A. T. Hassan, M. A. Moharram, and A. A. Kishk, "Empirical Analysis Formulae of Microstrip Ridge Gap Waveguide," *2018 IEEE International Symposium on Antennas and Propagation & USNC/URSI National Radio Science Meeting*, Boston, MA, 2018, pp. 423-424.
- [157] A. T. Hassan and A. A. Kishk, "Efficient Procedure to Design Large Finite Array and Its Feeding Network with Examples of ME-Dipole Array and Microstrip Ridge Gap Waveguide Feed," in *IEEE Transactions on Antennas and Propagation*, vol. 68, no. 6, pp. 4560-4570, June 2020.
- [158] A. A. Kishk and A. T. Hassan, "Design of Large Finite Array Antennas and its Feeding Network," *2019 IEEE International Conference on Computational Electromagnetics (ICCEM)*, Shanghai, China, 2019, pp. 1-3.
- [159] A. T. Hassan and A. A. Kishk, "Mutual Coupling and Failure analysis in Phased Antenna Arrays," *2019 IEEE International Symposium on Antennas and Propagation and USNC-URSI Radio Science Meeting*, Atlanta, GA, USA, 2019, pp. 1757-1758.
- [160] A. T. Hassan and A. A. Kishk, "Circularly Polarized Antenna Array Based on Microstrip Ridge Gap Waveguide at 60 GHz," *2020 14th European Conference on Antennas and Propagation (EuCAP)*.
- [161] A. T. Hassan and A. A. Kishk, "4×4 MIMO Antenna Elements Fed by Microstrip Ridge Gap Waveguide," *2019 IEEE International Symposium on Antennas and Propagation and USNC-URSI Radio Science Meeting*, Atlanta, GA, USA, 2019, pp. 419-420.
- [162] A. T. Hassan and A. A. Kishk, "Microstrip Ridge Gap Waveguide Hybrid Coupler at 60 GHz," *2018 IEEE International Symposium on Antennas and Propagation & USNC/URSI National Radio Science Meeting*, Boston, MA, 2018, pp. 427-428.
- [163] A. T. Hassan and A. A. Kishk, "Enhanced Gain and Bandwidth of Single Magneto-Electric Dipole Antenna at 60 GHz Using Double Superstrates" *2020 IEEE International Symposium on Antennas and Propagation & USNC/URSI National Radio Science Meeting*, Montréal.
- [164] A. T. Hassan and A. A. Kishk, "Monopulse Microstrip Ridge Gap Waveguide Antenna Array" *2020 IEEE International Symposium on Antennas and Propagation & USNC/URSI National Radio Science Meeting*, Montréal.